THE UNIVERSITY of ADELAIDE

Explicit Numerical Simulation of Microfluidic Liquid Flows in Micro-Packed Bed

Moein Navvab Kashani

A thesis submitted for the degree of Doctor of Philosophy

School of Chemical Engineering
The University of Adelaide
Australia

June 2015

Declaration

I certify that this work contains no material which has been accepted for the award of any other degree or diploma in my name, in any university or other tertiary institution and, to the best of my knowledge and belief, contains no material previously published or written by another person, except where due reference has been made in the text. In addition, I certify that no part of this work will, in the future, be used in a submission in my name, for any other degree or diploma in any university or other tertiary institution without the prior approval of the University of Adelaide and where applicable, any partner institution responsible for the joint-award of this degree.

I give consent to this copy of my thesis when deposited in the University Library, being made available for loan and photocopying, subject to the provisions of the Copyright Act 1968. The author acknowledges that copyright of published works contained within this thesis resides with the copyright holder(s) of those works.

I also give permission for the digital version of my thesis to be made available on the web, via the University's digital research repository, the Library Search and also through web search engines, unless permission has been granted by the University to restrict access for a period of time.

Moein Navvab Kashani

6 June 2015

Abstract

Microfluidic systems are of tremendous technological interest as demonstrated by their use in chemical analysis (so called 'lab-on-a-chip') and biochemical analysis (e.g. to detect biomarkers for disease), and in process intensification. Packed beds of micro-sized particles possibly utilized for enhancing heat and mass transfer in microfluidic devices, where the flow regime is normally laminar, as well as provide significant increases in surface area per unit volume for analytical chemistry and biochemistry, and for separation and purification. Whilst macro-scale packed beds have long been well understood, the same is not true of their microfluidic counterparts, which we term micro-packed beds or µPBs. Of particular concern is the effect that the small bed-to-particle diameter ratio has on the nature of the bed packing and the hydrodynamics of the flow within them. This lack of understanding stems in part from the challenges that are faced in experimentally assessing µPBs and the flow through to them. The study reported in this thesis addresses these concerns through a two developments. In the first body of work, a new method is proposed for the accurate reconstruction of the structure of a µPB from X-ray micro-computed tomography data for such beds. The porosity obtained from µPB was, within statistical uncertainty, the same as that determined *via* a direct method whilst use of a commonly used technique yielded a result that was nearly 10% adrift, well beyond the experimental uncertainty. This work particularly addresses the significant issues that arise from the limited spatial resolution of the tomography technique in this context. In the second part of the work reported here, a meshless computational fluid dynamics technique is used to study Newtonian fluid flow through µPBs, including determination of their permeability and the by-pass fraction due to wall effects, which are important in these beds. This use of a CFD allows determination of parameters that are difficult to determine experimentally because of the challenges faced in measuring the small pressure drops involved and the absence of the limited spatial and temporal resolutions of various imaging techniques. The meshless method used here also overcomes the challenges normally faced when seeking to discretise the complex three-dimensional pore space of the packed bed. The developments here open the way to studying more complex µPB configurations, and other processes within them such as non-Newtonian flows and mass and heat transfer.

Achievements

Three following papers were achieved from this work:

1) Navvab Kashani, M., Zivkovic, V., Elekaei, H., Biggs, M. J., *A new method for reconstruction of the structure of micro-packed beds of spherical particles from desktop X-ray microtomography images. Part A. Initial structure generation and porosity determination*, submitted to Chemical Engineering Science, Elsevier, 2015.
2) Navvab Kashani, M., Zivkovic, V., Elekaei, H., Herrera, L. F., Affleck, K., Biggs, M. J., *A new method for reconstruction of the structure of micro-packed beds of spherical particles from desktop X-ray microtomography images. Part B. Structure refinement and analysis*, submitted to Chemical Engineering Science, Elsevier, 2015.
3) Navvab Kashani, M., Elekaei, H., Zhang, H., Zivkovic, V., Biggs, M. J., *Explicit numerical simulation-based study of the hydrodynamics of micro-packed beds*, submitted to Chemical Engineering Science, Elsevier, 2015.

A part of this work was also presented in conference with the following titles:

1) Navvab Kashani, M., Zivkovic, V., Alwahabi, Z., Biggs, M. J., *Particle packing structure in a rectangular micro-capillary*, Chemeca 2012, 23-26 September 2012, Wellington, New Zealand.

Acknowledgements

Over the past four years, I was inspired and supported by many people without whom I would never have been able to finalize this dissertation. This section is therefore dedicated to all those people who have shared their time, enthusiasm and expertise with me, admitting that I will never be able to thank enough those whom I am indebted the most. I would like to express my deepest gratitude and appreciation to all of them.

I would like to start by thanking my principal supervisor, Prof Mark J. Biggs for his ongoing advice, encouragement and support during the entire course of my PhD study. Many of the achievements would have not been possible without his support and guidance. Mark, your expertise and detailed critical comments on every part of my research, pushed me to think deeper about my research and shape my ideas. I am also very grateful to the other members of the supervision team, A/Prof Zeyad Alwahabi and Dr Hu Zhang for their valuable feedback and supports.

My heartfelt gratitude goes to Dr Vladimir Zivkovic for all the inspiration and motivation I received from him. Vlad, thank you for all the valuable discussions we had together and for your constructive comments on my research. You have been my great mentor and always cheered me up, when I felt down.

During the four years of my PhD, I have been lucky to discuss my research and collaborate with many bright people. In particular, I wish to extend my appreciation to Dr Milan Mijajlovic and Dr Luis Herrera Diaz. Milan, thanks for your occasional support in computer coding and programming. Luis, I truly enjoyed our collaboration on a joint paper as well as long discussion we had about the Monte-Carlo algorithm.

I am more thankful than I can say to Mr Ron Seidel and Mrs Marilyn Seidel. Ron, I would not be able to describe your big heart in a few words, I can just wholeheartedly thank you for all the endless support I have received from you. You have been a cheerful caring friend and a bullet of energy for me. Your honesty, experience and kindness make you a person with whom talking is nothing else but a pleasure. I have learnt a lot from you, which will leave in my memory forever. Marilyn, you are always nice and kind to me,

which makes me feel at home. You two made my PhD journey much more enjoyable. Thanks for everything.

The Government of Australia and the University of Adelaide are gratefully acknowledged for providing me International Postgraduate Research Scholarship (IPRS) and Australian Postgraduate Award (APA) for my study in Australia. Also, The X-ray micro-computed tomography was undertaken at Adelaide Microscopy, a node of the Australian Microscopy & Microanalysis Research Facility (AMMRF). The cluster super-computational facilities and high-performance computing (HPC) system for this work were provided by *eResearch SA organization,* which is warmly appreciated.

I am deeply indebted to my loving parents, who have been always encouraging their children to continue their education and broaden their mind. Dad, thank you for your infinite support. Mum, you showed me why I should study. You created a home environment that encouraged your children to study and learn. Words cannot describe how grateful I am for your never ending love and care and all you have done for me. Without your support, I would never achieve what I have today. I am also thankful to my lovely brothers, Amin and Mohsen, for their encouragements during my study time overseas.

The last word of acknowledgment I have saved for my best friend, greatest partner, and lovely wife, Hamideh. Hamideh, you went through every step of this long PhD journey with me. While you were also going through a similar demanding PhD study, your kind, calm and loving character even during my mood changes carried me through these four years. Whiteout you, I would have struggled to find the inspiration and motivation desired to complete this dissertation. Thank you for your warm presence in my life.

Moein Navvab Kashani

June 2015

List of Figures

List of Tables

Abbreviations

BGAF	Basic Gradient Approximation Formula
CFD	Computational Fluid Dynamics
CT	Computed Tomography
DEM	Discrete Element Method
DGAF	Difference Gradient Approximation Formula
DNS	Direct Numerical Simulation
ENS	Explicit Numerical Simulation
FDM	Finite Difference Method
FEM	Finite Element Method
FVM	Finite Volume Method
HPC	High-Performance Computing
HT	Hough Transform
LBM	Lattice Boltzmann Method
LGA	Lattice Gas Automata
LOC	Lab-On-a-Chip
LoG	Laplacian of Gaussian
MC	Monte Carlo
MD	Molecular Dynamics
MRI	Magnetic Resonance Imaging
NMR	Nuclear Magnetic Resonance
NNP	Nearest Neighbouring Particles
NNPS	Nearest Neighbouring Particle Searching
PPE	Pressure Poisson Equation
PSD	Particle Size Distribution
Re	Reynolds Number
RMC	Reverse Monte Carlo
RTD	Residence Time Distribution
SA	Simulated Annealing
SD	Standard deviation
SGAF	Symmetric Gradient Approximation Formula
SPH	Smoothed Particle Hydrodynamics
3D	Three-dimensional
2D	Two-dimensional
µPB	Micro-Packed Bed
µTAS	Micro Total-Analysis-System

Nomenclature

a	[m/s^2]	Acceleration
A	[-]	Scalar quantity
A	[m^2]	Area
A_w	[-]	Wall correction parameter
B_w	[-]	Wall correction parameter
C	[m/s]	Sound speed
C_D	[-]	Drag coefficient
D	[m]	Bed diameter
D_{ij}	[m]	Particle-particle overlap
D_{iw}	[m]	Particle-wall overlap
d_{ij}	[m]	Minimum distance between particles in packed-bed
d_p	[m]	Sphere diameter
f	[-]	General function
F	[-]	Objective function
g	[m/s^2]	Gravitational acceleration
h	[m]	Cut-off distance (smoothing length)
I	[-]	Unit tensor
K	[-]	Number of sequential circular planes partitioning of a spherical particle
k	[m^2]	Permeability
K_1	[-]	Experimental coefficient in Reichelt model
L	[m]	Bed length
L_0	[m]	Initial distance between particles
M	[-]	Particle-to-bed size ratio
m	[kg]	Mass of particle
N	[-]	Number of computational cells
N_p	[-]	Number of SPH particles
P	[-]	Probability
P	[Pa]	Pressure
ΔP	[Pa]	Pressure drop
r	[m]	Position
r_{ij}	[m]	Distance between particles *i* and *j*
$\acute{r}$	[m]	Location of individual particle
R	[-]	Inter-plane resolution of x-ray microtomography
R_h	[m]	Hydraulic radius
R_O	[-]	Roundness
t	[s]	Time
t	[-]	Time step
Δt	[s]	Time step size
T	[K]	Temperature

u	[m/s]	Volume averaged fluid velocity
U_0	[m/s]	Superficial velocity
U_B	[m/s]	Bulk velocity
U_{max}	[m/s]	Maximum characteristic velocity
V	[m^3]	Particle volume
V	[m/s]	Velocity vector
W	[m^{-3}]	Smoothing kernel
x	[m]	Distance vector
$\mathbf{x}_{i0}$	[m]	Position of the particle in the initial 3d structure
$\overline{Z}$	[-]	Mean coordination number
γ	[-]	Coefficient for fluid properties
δ	[-]	Dirac delta function
ε	[-]	Porosity
ε	[-]	User-defined parameter in SPH particle-particle interaction model
η	[-]	Arbitrarily small quantity
μ	[Pa.s]	Dynamic viscosity
ρ	[kg/m^3]	Density
σ	N/m^2	Stress
τ	N/m^2	Shear stress
ϕ	[%]	Porosity
ξ	[-]	Random parameter
δx	[m]	Displacement
σ_i		Standard deviation
κ		Skewness
∇		Gradient operator

Subscript

i	Value for particle of interest
j	Value for neighbouring particles
b	Related to bed or bulk
D	Value for direct measurement
MC	From Monte Carlo
p	Value for particle
w	Related to wall
α	α-coordinate direction
β	β-coordinate direction

Superscript

α	Number of dimensions
β	Number of dimensions
*	Intermediate state

Table of contents

Chapter 1: **Introduction**

Microfluidic systems are devices in which processing and manipulation of fluids is performed in conduits having dimensions of the order of tens to hundreds of micrometres [1-4]. The micro-packed bed (µPB), examples of which are shown in Figure 1-1 [5, 6], has wide applicability in many applications of microfluidics. It is particularly useful in the process intensification context [7-10] as its large surface-to-volume ratio and short transport paths allow control of highly exothermic reactions [11-13] and mass transfer-limited reactions [14, 15]. The small volumes and short residence times of µPBs also mean they are ideal for rapid catalyst screening, allowing faster transfer of laboratory results into practise [16]. Beyond the process engineering context, they are widely used in clinical chemistry (also known as lab-on-a-chip) [17-20] and 'Micro Total-Analysis-System' (μTAS) [21], which has been since employed in a range of applications in chemical and biological analysis [22-26].

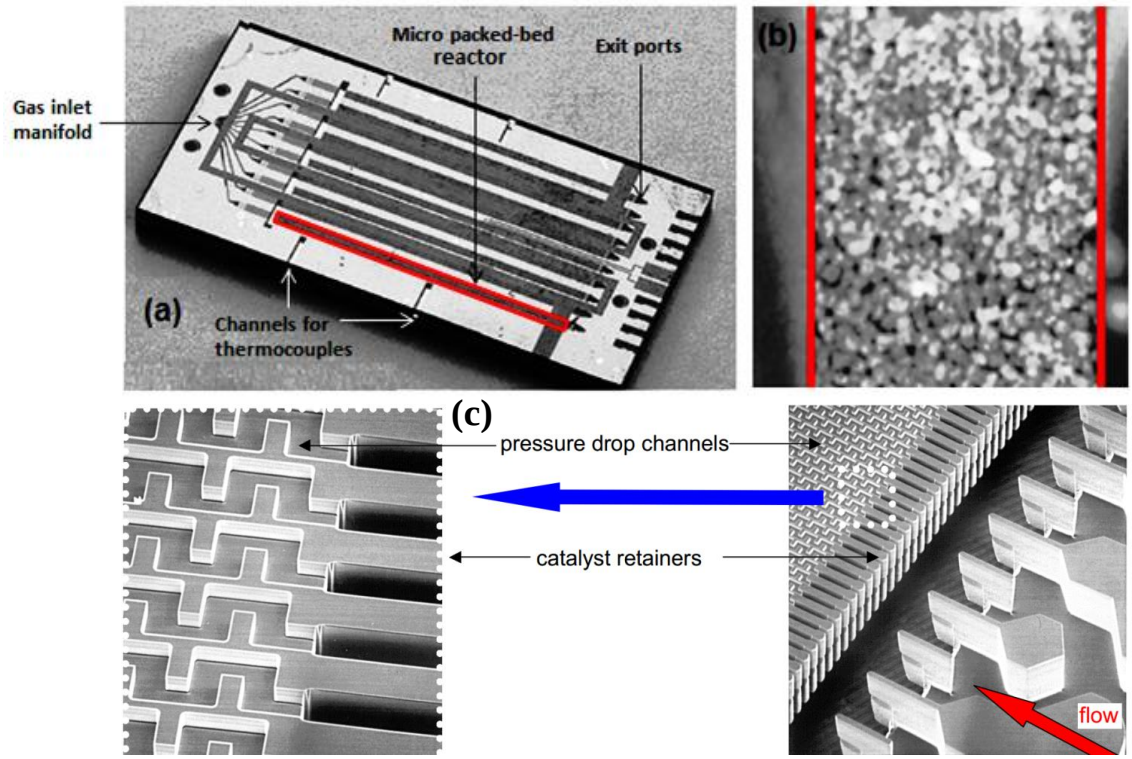

Figure 1-1 Multiphase-multichannel micro-reactor composed of 10 parallel micro-packed beds (µPB) (a); with micro-structured particles as packing catalyst (50µm particle size) (b); and complex µPB configuration (dimension of pressure drop channels is 40 µm wide, 1200 µm long, and 20 µm deep) (c), (adapted from [6, 27, 28]).

Whilst hydrodynamic studies on macroscale packed beds have been long-standing [29-32], the same cannot be said for their microfluidic counterparts. Such studies are necessary for a number of reasons. The first is the importance of the wall-region, which typically accounts for far more of the packed bed volume than in the macroscale counterparts due to the small bed-to-particle size ratio. A second primary reason is the pumping required to overcome pressure drop in μPBs is a major source of power consumption in microfluidic devices. Another incentive to study pressure drop is that it strongly influences two-phase heat transfer because pressure losses along the channel lead to a drop of the saturation temperature, which in turn impacts on the rate of heat transfer due to the higher driving temperature difference [33].

In principle, experimental study of μPB hydrodynamic character is straightforward in that it can mirror what is done at the macroscale. Such studies have been done. For example, hydrodynamic stability during start-up of three-phase μPB reactors has been investigated [34], as has residence time distribution (RTD) tests to determine global liquid holdup [35, 36] and gas–liquid flow in μPBs [37], and pressure drop and liquid holdup hysteresis [38]. Pressure drop studies have been performed for microchannels in the absence of micro-PBs for single-phase [39, 40] and two-phase [33, 39] flows. No studies have, however, concerned themselves with single phase pressure drop in μPBs, including the investigation of the effect of the channel-to-particle ratio. The absence of such studies is primarily due to the small pressure drops involved along with the difficulty of constructing devices that enable their measurement [40, 41]. Models for predicting pressure drop in μPB are, therefore, desirable.

Many models do exist for macroscale packed beds [42-44]. They may be wholly empirical, based on a theoretical considerations only, or a combination of both (*e.g.* based on a theoretical understanding but with an empirical coefficient to adjust the data) [42]. Ergun's equation [45] is an example of such a semi-empirical model. However, it applies only for packed beds with large channel-to-particle diameter ratios. If the bed diameter is not large in comparison to the particle diameter as in the case of micro-packed beds, the pressure drop suggested by the Ergun equation is likely to differ considerably from measurements due to the wall effects [46]. Models aimed at addressing wall effects have been developed for macroscale packed beds [47-53]. Whilst these may be applicable for μPBs, no work has

been done to establish this one way or the other. Moreover, extension of such models to more complex configurations such as that illustrated in Figure 1-1(c) [28] has not been undertaken.

Explicit numerical simulation (ENS) can in principle be used to replace experiment. In this approach, one attempts to model all the significant phenomena explicitly rather than in a mean field or average way as is done in many engineering models; in this sense, direct numerical simulation of turbulence is a class of ENS [54]. In the case of single-phase fluid flow in a real porous solid, ENS basically includes numerically solving the mass and momentum conservation equations of the interstitial fluid within the domain defined by the pore walls and any bounding surfaces such as, for a µPB, the bed walls. Explicit numerical simulation of flow in porous media requires two key elements: a model of the porous medium in question, particularly the pore space in which the fluid flows; and a method for solving for the flow within the porosity under a pressure gradient.

In the case of the modelling of the porous solid, there are four broad approaches for describing the geometry relevant to packed beds. The first is the unit cell method in which flow is modelled in a simple cell under periodic or similarly simple boundary conditions such as illustrated in Figure 1-2 [55] is used. This approach is, however, limited to structured packings [56-58], and are not particularly suitable for disordered packings such as those that occur in µPBs. The second approach are particle packing algorithms [59-67], which seek to imitate to a greater or lesser extent the way the bed is made; for example, modelling the deposition of particles into a container [68, 69]. This approach is, however, notorious for the challenges in obtaining appropriate packings within reasonable computational resource [70]. The third approach to building models of granular-based porous solids is reconstruction [71-76], where a model of the solid is formed by forcing it to match some experimental inputs (*e.g.* porosity, particle-particle pair distribution function or data derived from images) or some statistics that capture the essence of the solid or pore structure (*e.g.* particle size distribution). This approach is, however, limited to cases where the material is homogeneous (*i.e.* lack of variation of porosity at the course-grained scale, or at least slow spatial variation), something that does not hold in general for µPBs as we will see in the following chapters. The last method relies on direct, non-invasive imaging of the beds [77-79] using techniques such as X-ray microtomography

[80]. The main challenge here, however, is the resolution of these methods compared to the geometric features in µPBs.

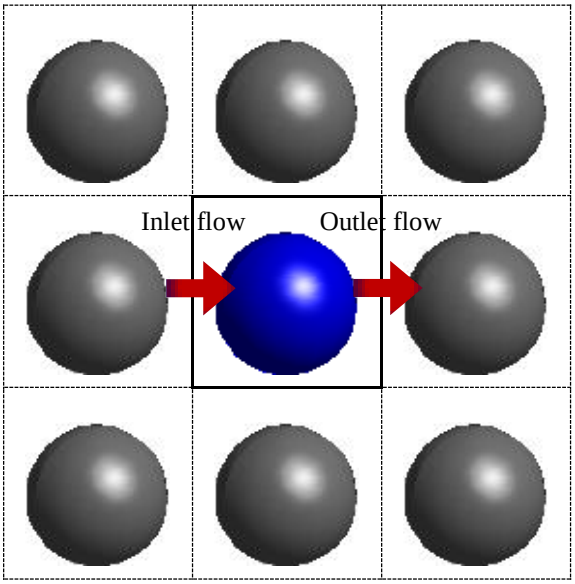

Figure 1-2 Principle of a 2D unit cell model (coloured), by applying periodic boundary condition to all directions of this unit cell (grey colours), the fluid flow could be modelled to all arrays of this structure

With regards to methods for solving for the flow within the porosity, computational fluid dynamics (CFD) is necessary when the flow domain is complex as in porous media. The standard CFD approaches such as those based on finite differences, elements and volumes, typically require the domain of interest to be 'meshed' as illustrated in Figure 1-3 [81, 82]. However, the generation of the meshes essential to such methods is not straightforward when the flow domain is complex in shape and, even more so, characterised by a range of length scales that necessitate a graduated change of mesh size. Such circumstances occur in µPBs. A potential solution to such challenges is to use so-called mesh-free methods. The most well-established of these is smoothed particle hydrodynamics (SPH) [83]. In SPH, a set of particles that interact with each other via a smoothing function carry fluid properties that evolve according to Navier-Stokes equations of fluid flow in their Lagrangian form [83]. In addition to removing the need to build a mesh, SPH also naturally clusters particles into regions where there are high spatial gradients; in effect, creating automatically the grading in the discretisation that is necessary when there are scale variations in the system of interest.

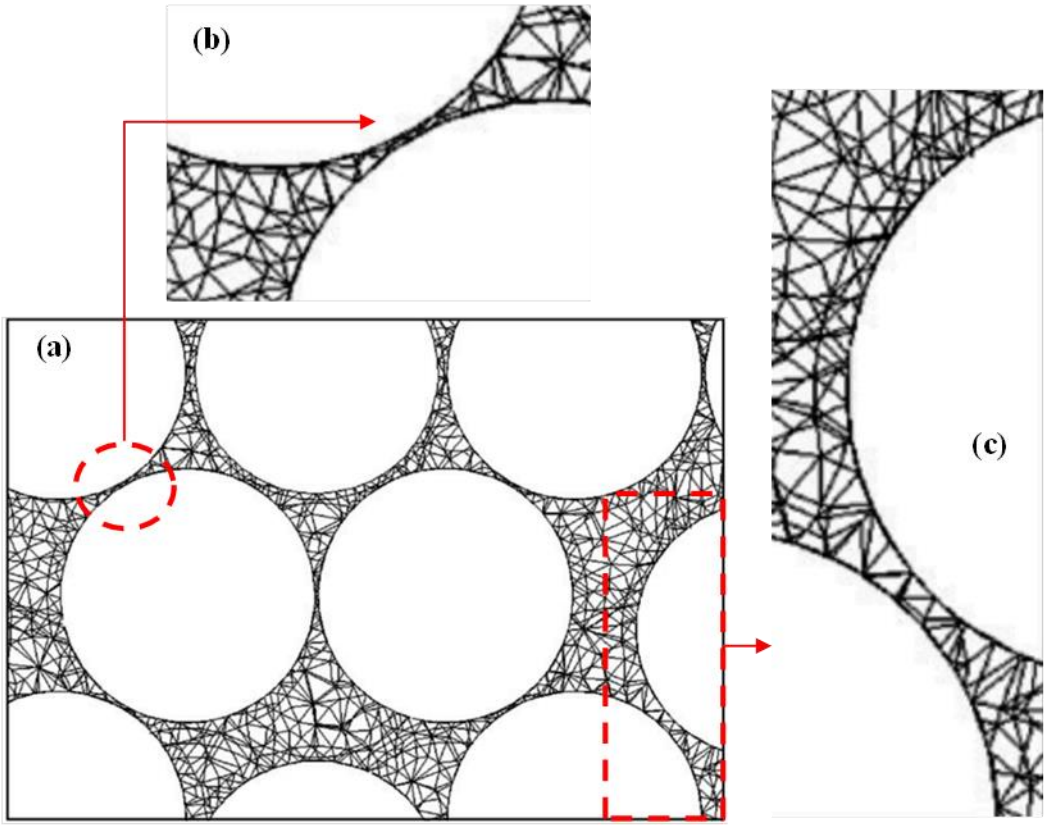

Figure 1-3 An example meshing of the pore space of a packed bed for solving the fluid flow in the pore space [81]: (a) overview of mesh; (b) zoom on the mesh to illustrate the refinement in the characteristic dimensions of the mesh as it transitions between the bulk porosity and the fine pore spaces located near the particle contact points; (c) zoom on the mesh to illustrate the refinement in the characteristic dimensions of the mesh in the boundary layer region of the particles where the gradients are large. Note the complexity of the mesh to accommodate the complex geometry of the porosity and the need to refine the mesh near surfaces and otherwise.

The aim of the work reported in this thesis was directed towards developing the application of mesh-free method to the explicit numerical simulation of liquid flows in the µPBs so as to determine their hydrodynamic character in general, and the effect of the wall region. The study reported here addresses these concerns through two related developments. The accurate reconstruction of the structure of a µPB from X-ray microtomography data of limited resolution relative to the characteristic dimensions of the bed represents the first development. This goal has been divided into two parts: the first involved generation of approximate structures (**Objective I**), and the second involved its refinement (**Objective**

II). The second development (**Objective III**) of the work reported here was concerned with a meshless computational fluid dynamics technique to study Newtonian fluid flow through μPBs, including determination of their permeability and the by-pass fraction due to wall effects. The developments described herein provide a basis for determining the hydrodynamic character of μPBs that are difficult to determine experimentally because of the challenges faced in measuring the small pressure drops involved and the absence of the limited spatial and temporal resolutions of various imaging techniques.

The thesis is laid out as follows. Chapter 2 provides a literature review that identifies research gaps that support the aim of the work reported here, as well as the technical background of the methods used. Chapters 3, 4 and 5 report the work undertaken to achieve **Objectives I**, **II** and **III, respectively**; these chapters are papers, all of which were submitted to the *Chemical Engineering Science*. The final chapter draws together the work reported here to make overall conclusions and suggest future work.

Chapter 2: **Literature Review**

2.1 Microfluidics

2.1.1 **Microfluidics technology**

Microfluidics, the science and technology utilized in the processing and manipulation of small amounts of fluids in channels having dimensions of the order of tens to hundreds of micrometers [1-4], is a fast developing research field with a broad variety of potential applications. Its genesis in the early 1990s [84] was in the form of what is now widely termed 'Micro Total-Analysis-System' (μTAS) [22-26], which has since been employed in a range of applications in chemical and biological analysis, including in clinical chemistry (also known as lab-on-a-chip or LOC) [17-20], medical diagnostics [85, 86], DNA analysis [22], cell biology (*e.g.* chemotaxis studies) and immunology [87]. This rising use is reflected in the growth of the biochip market from $400 million in 2001, to more than $2 billion in 2004 and $5 billion in 2009 [88]. Microfluidics is also of relevance beyond μTAS, including in colloid science [89], plant biology [90], and process intensification [7-10]. In the latter, specific applications include micro-chemical engineering technology [11, 91-94], which leads to higher product yields and new reaction pathways not possible in larger scale systems [3, 16, 95, 96], and control of extreme reactions [11-13, 15, 97].

2.1.2 **Micro-packed beds (µPB)**

Although microfluidic devices take on various shapes and structures (*e.g.* micro-coolers, micro-biochips and micro-reactors), rectangular micro-channels are the most frequently used due to ease of fabrication [98, 99]. Such a simple channel configuration does, however, bring limitations. One major limitation in many applications is the laminar flow within the channels due to their small dimensions and simple geometry, which leads to poor mixing and, thus mass and heat transfer [10, 100]; for example: the mixing length, which is the distance that a liquid must travel to become fully intermixed, can be of the order of centimeters or even meters, much greater than is available in typical microfluidic configurations where miniaturization is clearly the desired end-point.

One way of addressing the mixing challenge is to use a packed bed, also termed micro-packed beds (µPB) or micro-fixed beds [101-103], such as those shown in Figure 2-1 and Figure 2-2. The first of these is a µPB of $d_p = 115$ µm diameter catalyst particles within a channel of $D = 400$ µm square cross-section for gas-liquid-solid reactions [104]. The other figure shows a much shallower (400 µm length) µPB reactor of $D = 500$ µm depth containing $d_p = 60$µm glass beads [105]. The convoluted paths the particle beds enforce on the otherwise laminar flow in microfluidic devices promotes heat and mass transfer [14, 28, 106], making them suitable for highly exothermic [107, 108] and mass transfer-limited reactions [14, 109]. They also bring an increased surface area-to-volume ratio, which is useful if the particles within the bed act as an adsorbent or catalyst [109, 110]. The small test volumes and short residence times also make them ideal for rapid, high-throughput catalyst screening [16, 111].

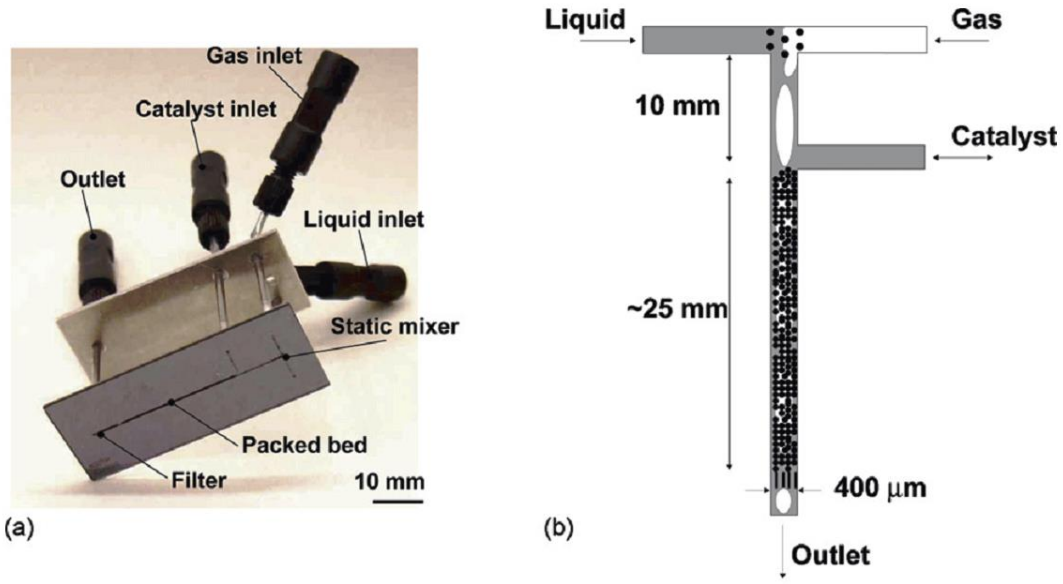

Figure 2-1 An example micro-packed bed (µPB) gas-liquid-solid reactor constructed in glass and silicon [105]: (a) overview of chip; and (b) schematic of the µPB reactor.

All else being equal, the pressure loss in a channel flow increases as the cross section decreases in size. As pumps are generally required to overcome pressure loss, this is a real challenge for microfluidic devices. The problem is, however, greatly exacerbated when µPBs are also present [112]. This means enhancements in mixing and all this brings must be traded off against energy consumption [113]. Whilst the pressure drop in packed beds

has long been known to depend on the mean porosity, particle geometry, particle size distribution, and Reynolds number [44, 114], hydrodynamic studies in µPBs indicate that the channel-to-particle size ratio, *D/dp*, is also important. This dependency has a couple of origins.

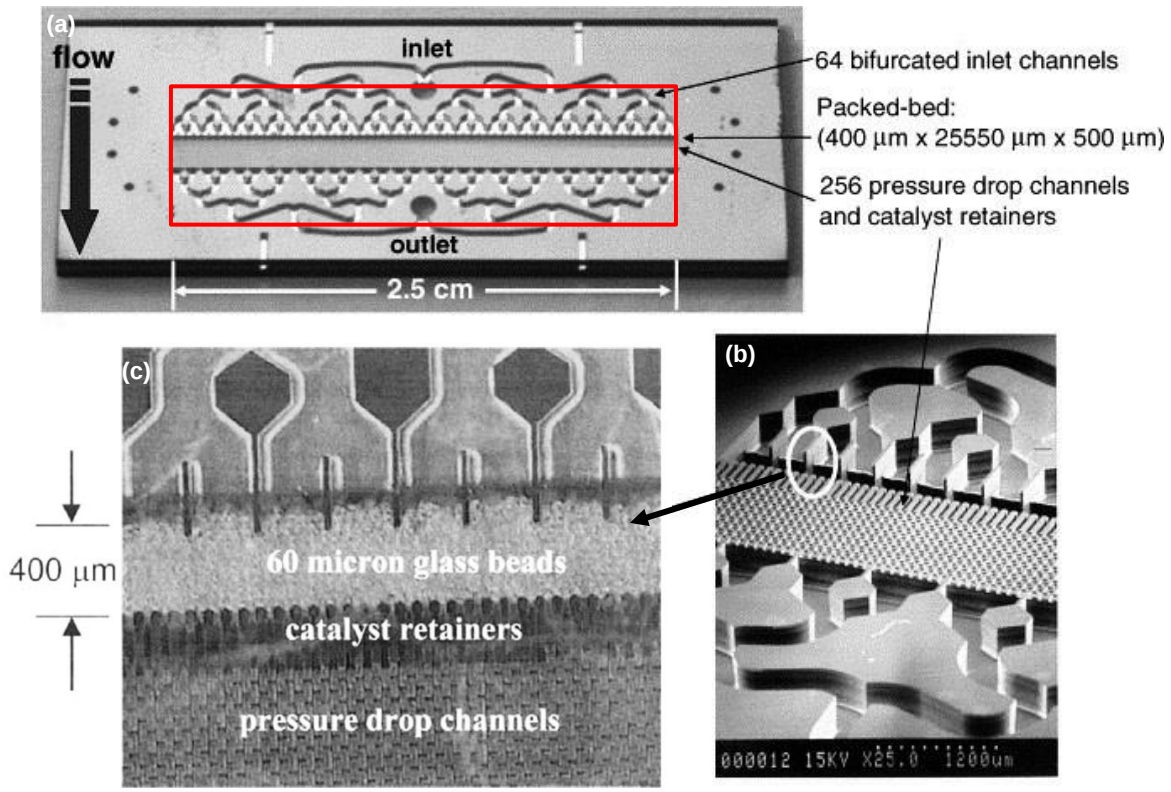

Figure 2-2 An example shallow (400 µm) cross-flow micro-packed bed (µPB) reactor in silicon [103]: (a) overview of chip showing how the reactant stream is bifurcated into 64 inlets into the bed; (b) a scanning electron micrograph close-up of the µPB; and (c) an even more higher resolution image of the µPB reactor showing the 60µm glass beads

Particles are typically randomly placed in packed beds (see Figure 2-1 and Figure 2-2, for example). The particles directly adjacent to the confining wall do not pack in the same way as those in the core of the bed due to the wall being impenetrable and, generally, smooth. As a result, there is an increased porosity next to the wall in comparison to the bed core, as seen at either end of the *x*-axis in Figure 2-3. In typical packed beds where the bed-to-particle size ratio is large, the bed core accounts for much of the volume and, thus, the wall region does not play a major role in the performance of the bed [115]. The opposite is true, however, when the bed-to-particle size ratio is small as in µPBs because the wall region accounts for a significant fraction of the bed volume. Figure 2-4 illustrates one major effect

of the higher porosity near the wall – the fluid velocity range and the dominant velocity are both greater in this region compared to the bulk of the bed. Figure 2-3 also shows that inhomogeneities in the porosity may also be present throughout the bed if it is of sufficiently small size relative to the particle diameter [116]. This too can lead to differences in performance relative to more homogeneous beds of the same average porosity [117].

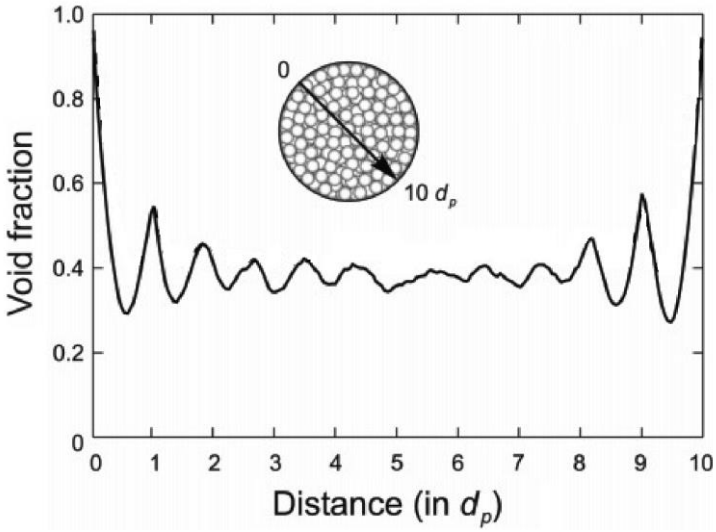

Figure 2-3 Porosity distribution for a random sphere packing in a cylindrical cross-sectioned channel of channel-to-particle diameter ratio of *D/dp* = 10 and porosity of 0.42 (after [117])

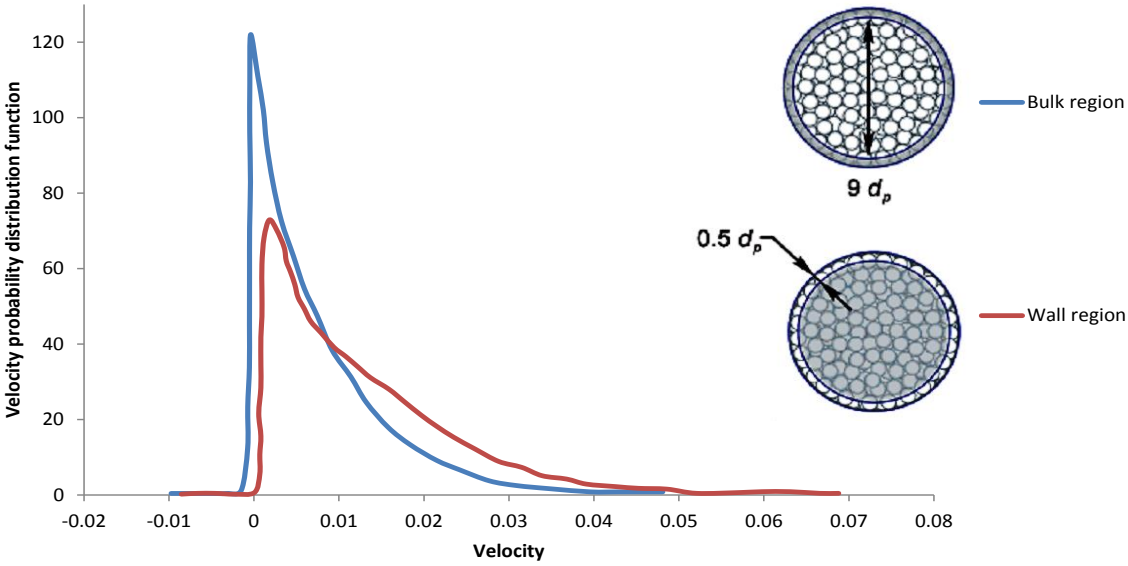

Figure 2-4 Velocity probability distribution functions in the bulk (blue) and wall (red) regions of a circular cross-sectioned packed bed of channel-to-particle diameter ratio of D/d_p = 10 (figure modified from [117])

2.1.3 **Pressure drop and flow models for packed beds**

Pressure drop in µPBs is of major concern because it is a significant source of power consumption in microfluidic devices [118]. Pressure drop also affects two-phase heat transfer in microfluidic devices because the pressure-dependence of the saturation temperature [33]. Being able to determine pressure drop in µPBs is, therefore, important.

A generalized flow model for pressure drop, ΔP, *per* unit length, L, of a packed bed is [42]

$$\frac{\Delta P}{L} = \alpha u + \beta u^2 + \gamma \frac{\partial u}{\partial t} \tag{1}$$

where α, β and γ are coefficients dependent on the fluid properties and the bed characteristics, and u is the volume averaged fluid velocity. The first term of Equation (1) is viscous in origin, the second relates to inertial effects, and the final term is connected to the acceleration of the flow. Under steady state or slowly varying conditions, which often hold, the third term can be ignored. The viscous term is dominant at low Reynolds numbers whilst inertial effects become increasingly important as Reynolds number increases. Since flow in µPBs is almost always characterised by low Reynolds numbers, the second term in Equation (1) can also be neglected, leaving just the linear term. This limit is termed Darcy's Law, which is often written as [42, 43]

$$\frac{\Delta P}{L} = -\frac{\mu}{k} u \tag{2}$$

where µ is the dynamic viscosity of the fluid, and k is the bed permeability. The negative sign simply reflects the fact that the direction of the velocity flow is opposite that of the pressure drop.

The permeability of a packed bed is the property that describes the ease with which a fluid can percolate through it and can be described as the bed's hydraulic conductivity. Many expressions have been proposed for this quantity over the past 100+ years [42, 43]. Some are based on idealised models of the porous media. For example, modelling a packed bed of porosity ε as a bundle of parallel tubes of diameter, d_p, much less than their length, Kozeny [119] proposed the following based on the assumption of Hagen-Poiseuille flow.

$$k = \frac{72(1-\varepsilon)^2}{d_p^2 \varepsilon^2} \tag{3}$$

The model is clearly an idealisation of a real packed bed; in reality, the pore space of randomly dumped particles is complex and tortuous, with interconnecting flow channels having no uniform geometry [119]. As a result, the fluid takes a longer path than simply the length of the theoretical tube. In one effort to account for this, Carman [120] used the work of Kozeny & Sitzber [119] to experimentally determine pressure drop through packed beds and concluded that the bed length should be multiplied by a constant (25/12) to account for the extra length [121]. This leads to what is commonly termed the Carman-Kozeny or Blake-Kozeny equation [119, 120]

$$\frac{\Delta P}{L} = \frac{150\mu(1-\varepsilon)^2}{\varepsilon^3 {d_p}^2} u \tag{4}$$

A range of other 'model-based' expressions, as well as 'model free' experimentally-derived correlations for the permeability are also available for packed beds as summarized in Bear [42], Dullien et al. [43], Happel et al. [122] and Azzam et al. [123] amongst others.

When the channel-to-particle diameter ratio is sufficiently small and, as a consequence, the flow mal-distributions and wall friction are non-negligible, there are some correlations for correcting the permeability for the 'wall effect'. However, opinion to date about the effect of confining walls on pressure drop in packed bed systems is contradictory. For instance, some researchers state that the inhomogeneity presented by the container walls reduces the pressure drop [53, 124], whereas others report an overall increase of the pressure drop due to the added wall friction [47, 125] or even find no measurable influence [44]. This research is, however, restricted to very low Reynolds numbers (Re < 1), where it could be argued that the wall friction is dominant and the coefficient of drag is less dependent on particle geometry.

In the case of low bed-to-particle ratio beds, the many and varied permeability models used for macroscale beds such as those mentioned above need to be modified to account for the significant influence of the wall region [49]. Gibilaro [51] proposes a simple model based on the division of the bed into two zones: the bulk or core that is unaffected by the wall,

and the wall region that is within a distance of *dp*/2 from the wall [126]. This two zone model leads to the following bulk velocity expression that is used in place of the superficial velocity in the Ergun equation above

$$U_B = \frac{U}{2.06 - 1.06(\frac{D/d_p - 1}{D/d_p})^2} \tag{5}$$

where U is total fluid flux, and a porosity, ε, value equal to that of the bulk region only. This equation models pressure drop relatively well at particle Reynolds number less than 10, but deviates from the experimental results quickly as the Reynolds number increases beyond this.

Based on the hydraulic radius theory and the Ergun equation, the following correlation for the pressure drop [118] proposed by Reichelt [127]

$$\frac{\Delta P}{L} = \frac{\rho {U_0}^2}{d_p}\left[\frac{K_1 A_W^2 (1-\varepsilon)^2}{Re\varepsilon^3} + \frac{A_W(1-\varepsilon)}{B_W\varepsilon^3}\right] \tag{6}$$

where U_0 is superficial velocity, ρ is density, K_1 is an experimental coefficient, and A_W and B_W are wall correction terms given by

$$A_W = 1 + \frac{2}{3(D/d_p)(1-\varepsilon)} \tag{7}$$

$$B_W = \left[k_1({}^{D}/_{d_p})^2 + k_2\right]^2 \tag{8}$$

In an attempt to improve the robustness of Reichelt's model, Eisfeld & Schnitzlein [118] fitted it to 2300 data points from 23 different research articles. Tsotsas [128] argued, however, that wall friction and flow mal-distributions at the container wall cannot be accounted for by the correlations proposed by Eisfeld & Schnitzlein [118]. There is little weight to this argument as the equation of Eisfeld & Schnitzlein is derived from a range of the empirical data which correctly encompasses all of the various effects of flow channelling and increased wall friction in the range of experimental methods. It is perhaps more appropriate to say that the effects of flow channelling and increased wall friction

cannot be separated from the data. What is more, their model is intended to give an empirical approximation for dimensionless pressure drop, which is a bulk value, rather than wall friction and flow mal-distribution effects directly. However, the increased wall friction and flow inhomogeneities may account for the large spread of data at high Reynolds numbers. Eisfeld & Schnitzlein [118] conducted a survey comparing the data with other empirical correlations. The root mean square deviations of the surveyed data compared to other correlations varied from less than 0.3 [45, 129] to more than 0.7 in some cases [53, 130].

Choi et al. [49] propose a correlation which recognises the increased wall friction and porosity as a result of the confining wall to predict pressure drop per unit length over a wide range of Reynolds numbers. They modified the original equation proposed by Ergun to take into account the effect of the confining wall.

$$\frac{\Delta P}{L} = \frac{150(1-\varepsilon)^2 \mu M^2}{\varepsilon^3 d_p^2} U \tag{9}$$

where M is defined as

$$M = 1 + \frac{2d_p}{3D(1-\varepsilon)} \tag{10}$$

This correlation fits some data with a reasonable degree of accuracy, e.g. with root mean square less than 10 for data reported in [131, 132], although not all, e.g. with root mean square more than 25 for data reported in [53]. On the assumption the experimental data has been collected competently, this reinforces the idea that there is no single correlation that can model every specific case accurately.

In summary, it can be concluded that models such as Darcy's Law and Ergun's equation can be effectively used to model pressure drop in packed beds where the bed-to-particle diameter ratio is not small. However, their application to packed beds where this ratio is small, such as in the case of μPBs, are less good [46] due to wall effects and porosity inhomogeneities. Additionally, they are not always well suited to beds whose porosity deviates substantially from around 0.4, something that will be shown in Chapter 3 is an issue also for micro-packed beds. Whilst various models have been suggested to address

these concerns, they are far from perfect in that it appears as if they are not entirely generalised. Thus, a method that allows the determination of pressure drop in micro-packed beds in a general way is needed. As the amount of data available for such systems is scarce [133], in part due to the challenges of measuring the pressure drop in microfluidic channels [41], modelling has a part to play here.

2.2 Explicit Numerical Simulation (ENS) of flow in porous media

Explicit numerical simulation (ENS) is a general concept where one attempts to model all the significant phenomena explicitly rather than in a mean field or average way as is done in many engineering models; in this sense, direct numerical simulation (DNS) of turbulence is a class of ENS [54]. In the case of single-phase fluid flow in a real porous solid, ENS principally includes numerically solving the mass and momentum conservation equations of the interstitial fluid within the defined domain defined by the pore walls. A more complicated illustration of ENS may be reported in [69], where the suspensions flow of solid-fluid with deposition in porous media is studied. Such ENS approaches have been used in place of experiment to determine directly (*i.e.* from first principles) the permeability of porous media. As an example, Piller et al. [134] used pore scale CFD-based ENS to compute the pressure fields and hydraulic permeability of real isotropic porous samples, using a model of the material derived from high-resolution X-ray tomography. Others (e.g. Vidal et al. [135] and references therein) have used Lattice Boltzmann Methods (LBM) in place of traditional CFD. None of the prior work has, however, concerned itself with μPBs, particularly with regards elucidating the wall effect.

Explicit numerical simulation of flow in porous media needs two key elements: a model of the porous medium in question, particularly the pore space in which the fluid flows; and a method for solving for the flow within the porosity under a pressure gradient. The second of these is dealt with in the last main section of this chapter. In the case of the modelling of the porous solid, there are four broad approaches relevant to packed beds, each of which will be outlined below.

2.2.1 **Unit cell method**

The first method for describing the geometry of a packed bed is to assume it is structured in a regular way. This allows the bed to be characterised by a unit cell in much the same

way as is done for a solid crystal. An example of such an approach is illustrated in Figure 2-5 [136]. Figure 2-5(a) to Figure 2-5(f) displays a cross-sectional view of the geometry of six representative packing unit cells. Each individual cell contains of eight sphere quarters, as seen in Figure 2-5(a), and an obstacle in the form of either a tube, Figure 2-5(b), or a band of rectangular cross-section in vertical or horizontal form, Figure 2-5(c) and Figure 2-5(d), or a triangular prism in different orientation to mean air flow, Figure 2-5(e) and Figure 2-5(f), respectively. As revealed in Figure 2-5(g), the uniform packing core was instead formed from cells "*a*" to "*e*", while for example the near-wall region was filled with tubes to reduce the near-wall channelling effects [136].

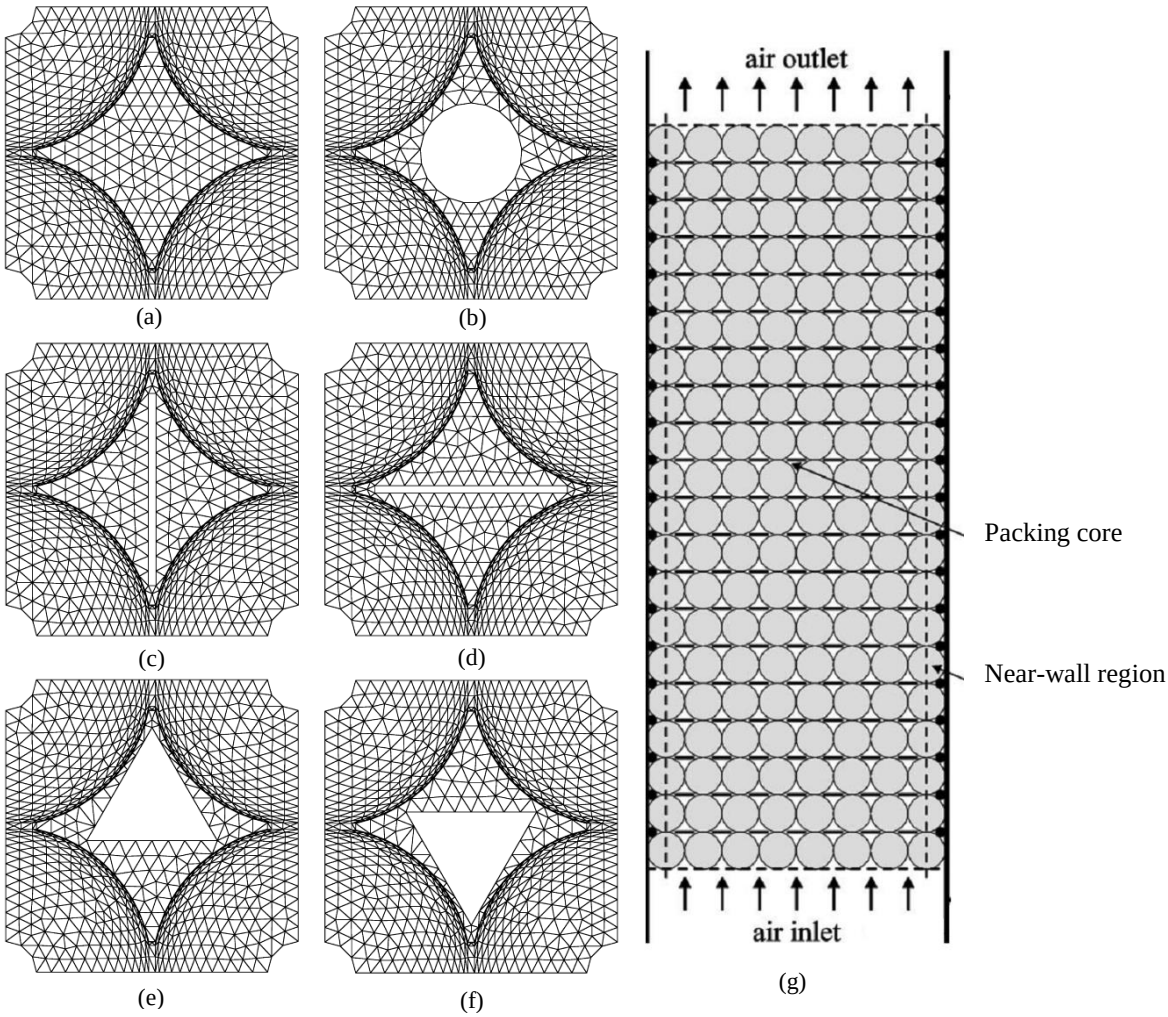

Figure 2-5 (a) to (f) Cross-sectional view of meshed geometry of the representative packing cells, and (g) arrangement of packed bed composed of unit cells [137]

If the unit cell is as simple as this and the flow sufficiently slow (*i.e.* low Reynolds number), then the permeability can be determined by analytical solution of the flow

problem for the unit cell. A variety of such analytical approaches have been proposed over the years, including the isolated-sphere model [138], Happel's model [29], Kuwabara's model [137], Brinkman's model [139] and the permeable sphere model [140-142]. The only slight distinction between "sphere-in-cell" type of models, like Happel's and Kuwabara's models, exist in the boundary conditions enforced on the surface of the fluid envelope. Tien et al. [143] compared the velocity profiles of the four models at different angular positions for a bed with porosity of 0.4. Both Happel's and Kuwabara's models produce necessarily the same results as anticipated; however in all cases, the values of Brinkman's model are slightly lower. Direct evaluation between the isolated-sphere model and the other three models is not feasible, since the value of the approach velocity in this model cannot be undoubtedly related to the superficial velocity. Instead, it is obvious that the velocity profiles obtained from the isolated-sphere model would still lie lower than the profiles based on Brinkman's model. Any one of these models can be employed to characterize granular media studies, excluding the isolated-sphere model [138]. For more complex unit cells and or flow scenarios, computational fluid dynamics (CFD) can be used on the unit cell [56-58].

Whilst the simplicity of the unit cell models is appealing, they are also limited in a couple of respects. The first is clearly the need for the solid structure to be open to being modelled as a regular packing – whilst exact regularity is not essential, the deviations cannot be large. Because the unit cell approach is predicated on a periodic symmetry, the models are also limited to bulk systems; wall effects cannot be considered – this is clearly an issue for µPBs where the wall effects are important.

2.2.2 **Particle packing algorithm method**

The second approach to modelling packed bed geometry is to mimic the way the bed is made. Many numerical algorithms for generating randomly packed beds have been advanced over the years, including those based on the discrete element method (DEM) [59-61] and Monte-Carlo based simulation [64, 65, 67, 144] amongst others [62, 145-147]. Discrete element method (DEM) [148, 149] is an explicit numerical model that solves Newton's Laws of motion for an assembly of (typically) rigid particles interacting via interaction functions. These interaction functions may be characterised by mechanical elements such as springs and dashpots [150], or soft potentials [151, 152]. The Monte-

Carlo based approaches mainly include the Monte-Carlo Rejection algorithm (overlap removal method) [153] and rain model Monte-Carlo method [154, 155]. The Monte-Carlo Rejection algorithm starts to generate the large collection of random points and then each random point is checked as to whether it is suitable as a particle centre coordinate. If a particle at that coordinate would overlap with other particles or structures in the core, it is rejected; otherwise it is accepted, and a particle is located at that position. There are also hybrid models such as the 'rain model' in which the filling process is mimicked by random placement of the particles (raining) followed by a subsequent compression step with Monte Carlo shaking routine to increase the packing fraction of the bed. Irrespective of the approach used here, the high density of packed beds means particle packing algorithms suffer from a long computational time scale and find it difficult to approach porosities typical of real beds. This means that permeabilities derived from such models may not reflect well the actual values.

2.2.3 **Reconstruction method**

The third approach to defining the geometry of a packed bed is termed 'reconstruction'. An efficient reconstruction method enables one to create structure and further analysis can be performed to achieve desired properties of the media. In this method, a model is created by forcing it to match some experimental inputs such as the porosity, particle-particle pair distribution function or data derived from images. This method becomes particularly useful when 3D imaging techniques are not available [156].

The Gaussian field approach [71-76] has established the base of many ENS studies of fluid flow in real porous media. A widely reconstruction approach to produce the discrete values representing the phases of the structure, is based on sequentially passing a normalized uncorrelated random Gaussian field through a linear filter firstly and then a nonlinear filter [157]. One approach to form 3D reconstruction from 2D was extended by Quiblier [71]. Alder et al. [158] performed the first studies with this method, considered reconstructed periodic images of sandstone resolved Stokes flow with periodic boundary conditions, using the finite difference method. The linear filter in this approach convolutes linearly the independent Gaussian field, giving another field that is still Gaussian distributed but correlated. Then, a threshold cut to the field performs by the nonlinear filter to create the last reconstructed structure. The statistical properties of the transformed field are

connected to that of the reference structure, through this nonlinear filter, and the problem leads to solving a nonlinear system of equations to find the coefficients of the linear filters. This technique has been further modified in [159, 160]. Another filtering approach is based on the linear filter with different functional form, which includes double level thresholding the corresponding correlated Gaussian random fields, initially proposed by Cahn [161], and was analysed in detail and employed by a number of researchers [162-165]. This approach is the basis for reconstructing many classes of non-particulate composite materials. However, the class of random media for which it works well is restricted, because of applying Gaussian random field [157].

Researchers have used models derived from the Gaussian field approach to study phenomena such as dispersion [68, 166, 167], flow with deposition in sandstone [168] and dissolution of mineral salt [169]. The convection–diffusion equation was solved in combination with the Stokes flow equation, to model immiscible two phase flow in reconstructed porous solids using the Lattice-Boltzmann method (LBM) [170], and LBM-based ENS to determine the permeability of reconstructed sandstone [171, 172]. Regarding the accuracy of this method, however, there is a controversial discussion as some researchers mentioned that ENS resultant data using reconstructions does not correspond more nearly with experiment [158, 172]. Similarly, Yao et al. (1997) [166] found one result that matched quite well their experimental data, while a second estimate was about five times greater than their experimental data. Hazlett [171] compared the permeability for the reconstructions and permeability by ENS on the main images from which the reconstruction statistics were achieved and reported to up to 60% difference. Finally, Humby et al. [54] developed a suite of LGA-based ENS tools for single and multiphase fluids in porous media to improve basic understanding of closure models and determining closure model parameters.

2.2.4 **Direct method**

The last approach involves direct use of experimentally determined structure using methods such as serial sectioning [173-175] as well as non-invasive imaging methods such as computed tomography (CT). A variety of imaging techniques have been used to study the structure of porous media and μPBs. A number of researchers have used scanning electron microscopy [77-79] and transmission electron microscopy [176, 177]. These

techniques are, however, tedious to extend to quantitative characterization of the three-dimensional (3D) structure of μPBs. Such analysis is possible using magnetic resonance imaging (MRI) [178, 179], scanning confocal microscopy [180], and X-ray micro-tomography [80]. The X-ray micro-tomography has the advantage of being able to reveal the transport processes occurring within the pore space in addition to resolving the bed structure that yields the pore space. The other methods, however, limited to systems containing protons (*i.e.* either the solid phase or void space must be proton-containing), and require access to expensive to buy and operate machines as well as the expertise to run them. These issues are not faced with scanning confocal microscopy, but it can only probe an order of 100 μm into the media [181].

X-ray micro-tomography offers a balance between the two methods: it can be used to image the entirety of a wide variety of materials, and easy-to-use bench-top systems are now available at modest prices [182]. This technique has been used in a non-destructive way to study multiphase flows[183], pores characterise of scaffolding in tissue [184, 185], tissue of bone analysis [186, 187], geosciences [188], cellular food products [189], fiber-polymer composite foam [190] and materials science [191]. Of particular interest here is the study of packing structure, micro-CT could be used in particle shape analysis [192], packing structure measurements of packed bed [193, 194], voidage fraction distribution [195] and phase distribution measurements [196].

In X-ray micro-tomography, the sample is rotated between a fixed X-ray source and detector. The source produces a polychromatic spectrum, where the X-ray intensity is a function of the photon energy. The spectrum is dependent upon the acquisition parameters and passes through the sample, where they are attenuated. The intensities of the attenuated X-rays are measured by the detector, and by applying a mathematical algorithm [197]. X-ray micro-tomography yields a series of planar images along an axis of a sample (*e.g.* along the length of the packed bed). These images are typically greyscale, with the grey level in a pixel being (allowing for noise) related directly to the solid density within the pixel. A more detailed explanation of the technique can be found in [197-199].

The projection images generated by the micro-CT scanner contain Poisson-distributed random noise [200] and beam hardening effect [201], which the first one is due to x-ray and light photon production processes at the source and the scintillating crystal; and the

second one has been known to be one of the major sources of error that leads to inaccuracy and artefact in the reconstructed images. Figure2-6 shows a typical example of cross-sectional reconstructed images from squared µPB by X-ray micro-CT, in which the particles are displayed bright (low grey values) and the background is dark (high black values).

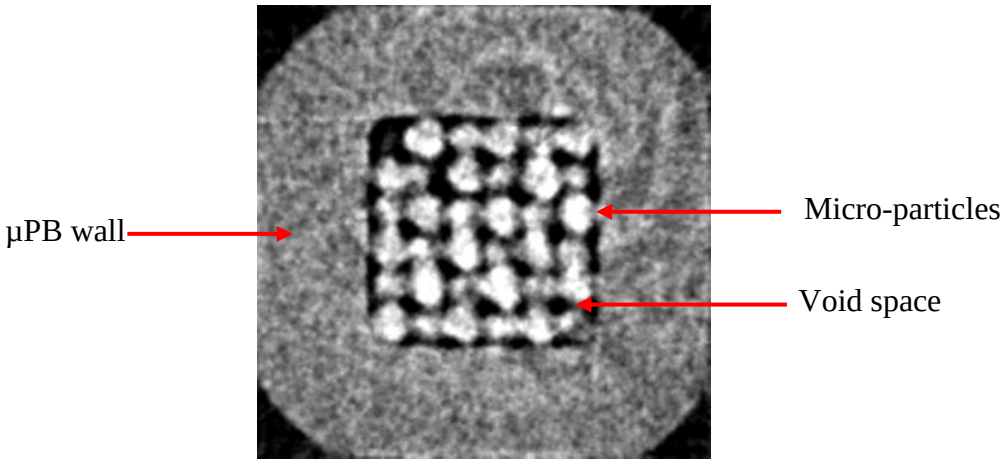

Figure 2-6 Cross-sectional image with X-ray micro-CT from a square µPB filled up with particles diameter of 38.5 µm

A critical step in using these images to reconstruct a 3D image of the solid structure and the pore space defined by it is finding the grey level (the threshold) that defines the boundary between solid and void (i.e. that transforms the grey-scale image into a binary image) [202-205]. Because of this criticality, many thresholding algorithms have been developed over the years [203, 206-209], and reviews for which may be found in [210, 211]. The plethora of thresholding methods that have been proposed reflects the common assertion that finding a threshold is a non-trivial task, and that there is no single threshold algorithm that is efficient for all sorts of problems. Whilst the threshold-identification issue is more an annoyance in many cases, it becomes a major issue for µPBs as the resolutions of bench-top X-ray micro-tomography systems are typically of the order of much of the pore space. In particular, as demonstrated below, small differences in the threshold can lead to significant changes in the pore structure and porosity. One alternative to thresholding are Hough Transform (HT)-based methods [212, 213]. However, the computational effort and memory requirements for such methods scales in a non-linear way with problem size [214], making them less than ideal for µPBs. Based on this need, a

new method is proposed for the accurate reconstruction of the structure of a µPB from X-ray micro-computed tomography data in the second chapter of this thesis.

Based on pore systems that obtained from tomographic images, some researchers have used ENS to model the flow in the complex interstitial pore space. From a number of volumes cut from X-ray tomographs of a sandstone, Spanne et al. [215] used a finite differences method to model the behaviour of the Stokes flow of a single phase Newtonian fluid. Also, for the ENS of immiscible multiphase fluid flow in pore systems obtained from X-ray tomographs of sandstone, Coles et al. [216] have used the LBM. LBM-based ENS have been used for single and multiphase flows on volumes cut from X-ray tomographs of sandstone [217, 218], with the finite-difference method used to solve the Stokes flow. In an effort to address issues related to the validity of this method, Mantle et al. [219] stated that LBM simulations on NMR-derived images of packed beds of several particles were in an agreement with the flow maldistribution detected by NMR velocimetry, reported by Manz et al. [220]. Bernsdorf et al. [221] performed the pressure drop analysis in a porous material and a bed packed with spherical catalyst particles by using LBM-based ENS on tomography-derived images.

2.3 Computational Fluid Dynamics approaches

The most realistic and extensively used approach to analyse the motion of a fluid within a complex heterogeneous structure is to use computational fluid dynamics (CFD) to solve the motion of a fluid mathematically from a set of governing equations. CFD can be broken down into two basic approaches, namely: (i) mesh-based approaches, and (ii) mesh-free approaches, which will be discussed with their details in the following sections.

2.3.1 **Background**

CFD simulation can give useful insight into system behaviour, and allows determination of parameters that are difficult to determine experimentally because of the challenges faced in measuring the small pressure drops involved in micro-devices. Moreover, data such as instantaneous pressure and velocity fields can be extracted along with a considerable amount of other data associated with the motion of a fluid in µPBs. CFD techniques are well defined and have established themselves as an accurate representation of fluid

behaviour. CFD can be broken down into two basic approaches, mesh-based approaches (Finite Element and Finite Volume methods) and mesh-free approaches.

In mesh-based approaches, the finite element and finite volume methods solve the Navier-Stokes equations by integrating the equations over a mesh of finite elements or volumes. The equations are coupled and non-linear and contain unknowns in which finite difference equations are substituted for the properties of the flow, which are solved using an iterative method. In order to solve the governing equations, the flow domain has to be suitably discretised into small volumes or elements leading to the solution of a partial differential equation. This process is referred to as meshing or grid generation. If a suitable grid or mesh is not produced, geometric fidelity issues occur with respect to the representation of the computational domain. Moreover, if a mesh of suitable quality is not created, instabilities occur when trying to solve the governing equations. Once a solution has been generated, properties of the flow can be extracted for each individual cell or element for analysis.

Mesh-based CFD methods have been used to study flow in pores spaces despite the challenges faced in use of these methods. The first and most major issue is the difficulties faced in meshing the complex geometry of the pore space; constructing a grid for irregular or complex geometry has never been an easy task, which can be even more computation costly than solving the problem itself [222]. Furthermore, when spheres are in contact with each other they produce an infinitely small contact point, which is difficult for a mesh generation discretization algorithm to fully describe. This phenomenon has become one of the major constraints when analysing packed beds using mesh-based approaches. An additional major constraint is the relatively large meshes which are produced relative to computational resources typically available.

On the other hand, mesh-free methods have been a most important research focus over the past years, for producing the next generation of more effective computational methods designed for more complicated problems. One preferable mesh-free method is Smoothed Particle Hydrodynamics (SPH) [83]. This method has two specific benefits in comparison with the long-established mesh-based numerical methods. Firstly, since SPH is a particle based method, by defining a suitable pore space, it is not needed to mesh the computational

geometry. Secondly, SPH is reasonably uncomplicated in numerical implementation, especially in comparison with mesh-based methods.

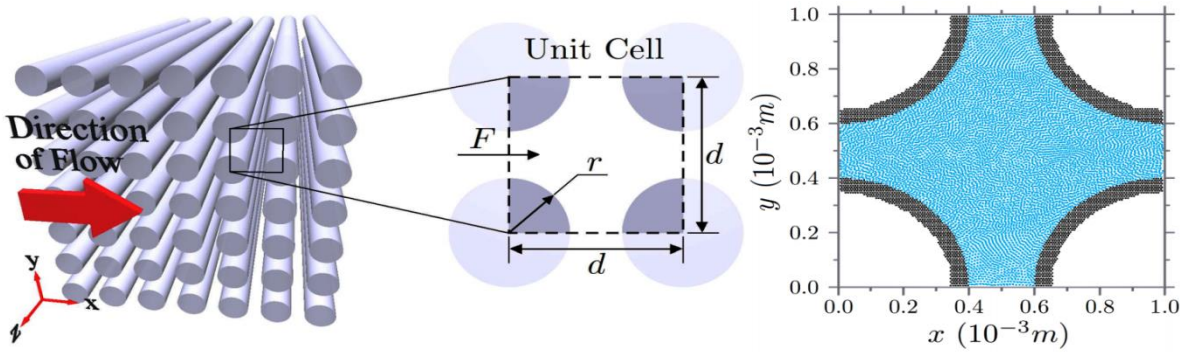

(a) (b) (c)

Figure 2-7(a) Square periodic array of infinite cylinders, (b) 2D unit cell of simulation and (c) configuration of fluid and boundary SPH particles after 5 seconds simulation [137]

As an example, the distributions of SPH particles and solid boundary position in a complex pore space are illustrated in Figure 2-7. Figure 2-7(a) shows a periodic array of infinite cylinders and direction of flow [223]. As shown in the Figure 2-7(b), a model of such an array of cylinders simplified to the two-dimensional unit cell, due to existence of symmetry. Fluid particles positioned on uniform two-dimensional hexagonal grids are shown in blue, and those arranged within the bounds of the solid cylindrical grains are indicated as boundary particles and shown in black. Figure 2-7(c) shows the disordered long time configuration of fluid SPH particles, after 5 seconds simulation.

For another instance of SPH particles distribution and solid boundary position, Jiang et al. [224] described a SPH based numerical model of the fluid flow in two-dimensional isotropic porous media. Figure 2-8 shows the predicted replacement due to the inserted body force of the SPH fluid particles through the void space enclosing the fixed porous material particles, where black solid diamonds indicate porous material particles, and grey open circles designate fluid particles. Flow direction is from left to right, where only the fluid particles with a stream wise velocity more than the x-direction average fluid velocity are shown. This model does not precisely determine the microscopic pore structures, however depicts the 2D porous structure, made by randomly embedding fixed position SPH particles inside the entire geometry of the porous system in terms of certain porosity,

where the desired porosity in Figure 2-8(a) and Figure 2-8(b) are 0.5 and 0.8, respectively. To investigate the influence of pore scale heterogeneity, in addition to the anisotropy of such flows, Tartakovsky et al. [225] developed a numerical model based on SPH to simulate immiscible and miscible fluid flows in porous media. By using randomly located non-intersecting circular grains of various sizes, models for heterogeneous porous media were created. Also, by randomly placing non-overlapping particles on either side of the gap between two fractal curves to generate a kind of micro-fracture, pore scale was introduced [225]. Figure 2-9 shows the moving of a more viscous, less dense non-wetting fluid (dark grey colour) by a less viscous, denser wetting fluid (light grey colour) in a fractured porous medium (black colour) in three consecutive time steps. In all these figures, the micro-fracture is in the direction of flow. It could be concluded, SPH method has to date only been applied to more regular or two-dimensional porous systems.

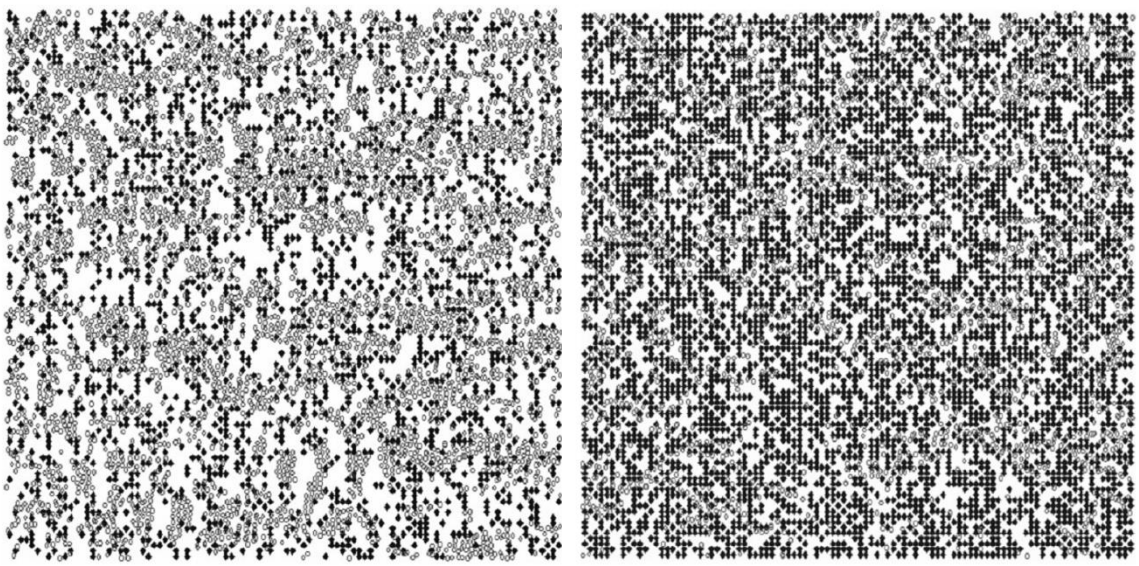

(a) **(b)**

Figure 2-8 Preferential flow paths in isotropic porous media with porosity equal to (a) 0.5, and (b) 0.8 [224].

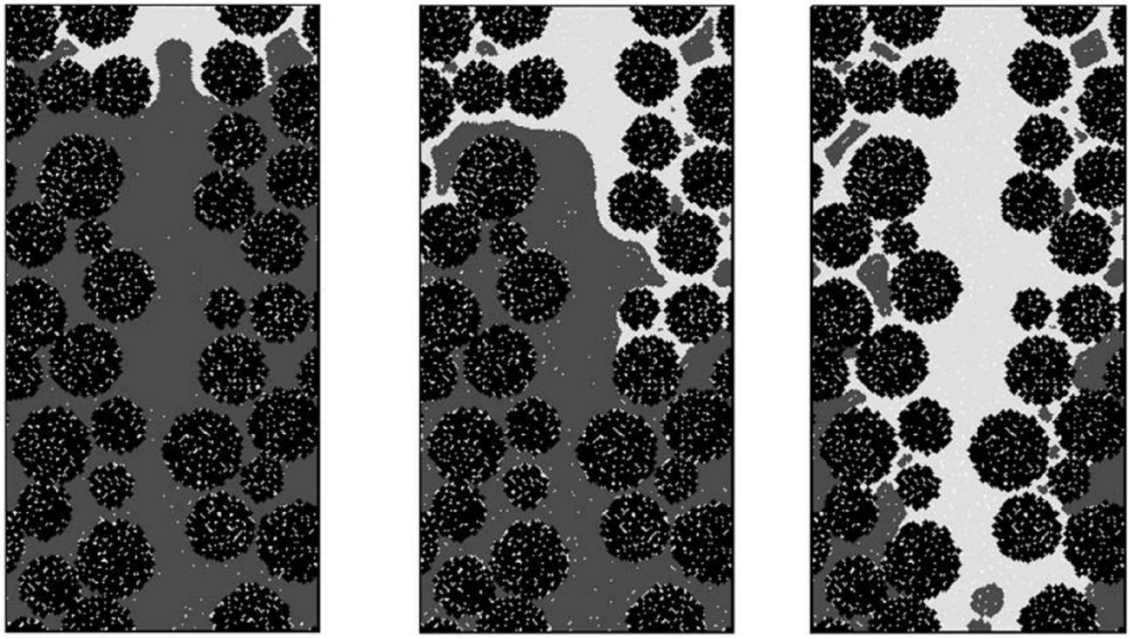

Figure 2-9 Displacement of a more viscous, less dense non-wetting fluid (dark grey colour) by a less viscous, denser wetting fluid (light grey colour) in a fractured porous medium [225]

Although of less concern for the specific study here, simulation-based study of multiphase fluid flow in microfluidic devices requires the moving boundaries of the separate phases to be tracked, and forces such as those arising from capillary and other effects to be accounted for due to the large ratio of surface area-to-volume ratios involved. Inclusion of such effects in traditional Eulerian grid based numerical procedures, such as FDM, FEM and FVM, is very computationally intensive and difficult indeed due to the need to move the mesh and track interfaces. Lagrangian non-grid based methods such as SPH, on the other hand, do not suffer such problems.

2.4 Smoothed Particle Hydrodynamics (SPH) method

2.4.1 **Background**

Smoothed particle hydrodynamics is an established mesh-free particle method. It was initially developed to solve astrophysical problems in three dimensional open spaces. The reason for that implementation was the similarity between the group motion of those particles and the transportation of a liquid or gas flow, which will be modelled by the governing equations of conventional Newtonian hydrodynamics [226]. In SPH method, a

set of particles that have material properties and have interaction with each other under the range restricted by a weight (smoothing) function, demonstrate the state of a system [83]. With the aid of these discrete particles, the discretization of the governing equations have been achieved and for calculating the acceleration, velocity and local density of the fluid, a diversity of particle-based formulations have been employed. Afterwards, the pressure of fluid is calculated and with the pressure gradient and density, the particle acceleration is obtained. In the following, first the equations of motion are presented, followed by a brief description of the incompressible SPH method and spatial derivative equations. Then, the time integration procedure is described. Finally, SPH solving algorithm and solution procedure are discussed.

2.4.2 **Fluid flow equations**

For modelling laminar incompressible Newtonian fluid flow, the mass and momentum conservation equations are:

$$\frac{d\rho}{dt} = -\rho \nabla . \mathbf{V} \tag{11}$$

$$\rho \frac{d\mathbf{V}}{dt} = -\nabla P + \mu \nabla^2 \mathbf{V} + \rho g \tag{12}$$

where ρ is the fluid density, P is the pressure and $\boldsymbol{V}$ is the velocity vector. Also, g represents the acceleration of gravity and μ is the dynamic viscosity of the fluid [227]. To conclude this system of equations, it is necessary to bring an equation to explain the change of density with pressure. The SPH formulation is inherently compressible. For simulation of an incompressible fluid, it is necessary to enforce the incompressibility by additional equations (means achieving near incompressibility), such as Poisson equation or equation of state. It is possible to directly solve the Poisson pressure equation as Equation (13) [228].

$$\nabla^2 P = \rho \frac{\nabla . \mathbf{V}}{\Delta t} \tag{13}$$

Solve the Poisson pressure equation is maybe computationally expensive and though this method makes it possible to use large time steps, it also carries a higher cost per time step [229-231].

2.4.3 **General SPH formulation**

In SPH formulation the various influences of the Navier-Stokes equation are simulated by a set of forces that act on an individual particle at a location $\acute{r}$, where these forces are given by scalar quantities that are interpolated at a location *r* by a weighted sum of contributions from all neighbouring particles inside a cut-off distance *h* in the space. This can be expressed in integral form as follows [232].

$$A_i = \int_{\Omega} A(\acute{r})\, W(r - \acute{r}, h) d\acute{r} \tag{14}$$

By approximating the integral interpolant by a summation interpolant, the numerical equivalent to Equation (14) is obtained [232].

$$A_i = \sum_j A_j V_j W(r_{ij}, h) \tag{15}$$

where j is iterated over all particles, V_j the volume attributed implicitly to the particle j, $r_{ij} = r_i - r_j$, where r is the position of a particle, and finally A is the scalar quantity that is being interpolated. The summation is over particles which lie within the radius of a circle centered at r_i. The following relation between volume, mass and density applies.

$$V = \frac{m}{\rho} \tag{16}$$

where m is the mass and ρ is the density. Combining this we get the basic formulation of the SPH interpolation function.

$$A_i = \sum_j A_j \frac{m_j}{\rho_j} W(r_{ij}, h) \tag{17}$$

where j repeats over all particles, m_j is the mass of particle j, r_j its position, ρ_j the density and A_j the scalar quantity at position r_i. This function can be used to approximate any continuous quantity field, and can be evaluated everywhere in the underlying space [232].

2.4.4 **Smoothing kernel**

The function $W(r_{ij}, h)$ is the smoothing kernel, which is a scalar weighted function. The function uses a position r and a smoothing length h. This radius can be seen as a cut-off for how many particles will be considered in the interpolation. This cut-off radius sets $W = 0$ for $|r_{ij}| > h$ [232].

2.4.5 **Spatial derivatives**

In SPH, the derivatives of a function can be obtained by using the derivatives of the smoothing kernel that results in the Basic Gradient Approximation Formula (BGAF) [233]:

$$\nabla A_i = \sum_j A_j \frac{m_j}{\rho_j} \nabla W(r_{ij}, h) \tag{18}$$

$$\nabla^2 A_i = \sum_j A_j \frac{m_j}{\rho_j} \nabla^2 W(r_{ij}, h) \tag{19}$$

These formulations can produce spurious results, and several corrected formulations have been developed. One of these is the Difference Gradient Approximation Formula (DGAF), which has the advantage that the force vanishes exactly when the pressure is constant [233].

$$\nabla A_i = \frac{1}{\rho_i} \sum_j m_j \, (A_j - A_i) \, \nabla W(r_{ij}, h) \tag{20}$$

The forces between two particles must observe Newton's Third Law that for every action there is an equal and opposite reaction. Pair-wise forces must be equal in size with opposite sign ($f_i = -f_j$). This means that the differentials in the Navier-Stokes equations that create these forces must be symmetrized. Monaghan developed a symmetrization, referred to as the Symmetric Gradient Approximation Formula (SGAF) [83]. This

formulation conserves linear and angular momentum exactly but is not as accurate as DGAF [233]. It is commonly used for the pressure gradient.

$$\nabla A_i = \rho_i \sum_j m_j \left(\frac{A_i}{{\rho_i}^2} - \frac{A_j}{{\rho_j}^2}\right) \nabla W(r_{ij}, h) \tag{21}$$

An alternative symmetrical formulation is as Equation (22) [226].

$$\nabla A_i = \sum_j \frac{m_j}{\rho_i} \left(A_i + A_j\right) \nabla W(r_{ij}, h) \tag{22}$$

The basic formulation of the Laplacian has been found to be somewhat unstable under certain conditions, and there exist a wide range of possible corrections. Shao and Lo established a correction well suited for the correction of the Laplacian in the viscous force [234].

$$\nabla.\left(\frac{1}{\rho}\nabla A\right) = \sum m_j \frac{8}{(\rho_i + \rho_j)^2} \frac{\left(A_i - A_j\right).\nabla W(r_{ij}, h)}{\left|\mathrm{r_{ij}}\right|^2 + \eta^2} \tag{23}$$

To remain the denominator non-zero, η variable is used, which is equal to $0.1h$.

2.4.6 **Solid boundary treatment**

Imposition of solid boundary condition is of prime importance to the solid-liquid modelling with SPH method, as the forces exchanged among the fluid and solid (i.e. drag) are decided via this condition. Solid boundary treatment in the SPH method includes three main techniques. The first technique uses dummy SPH particles, similar to the fluid SPH particles, which are attached like some layers of particles to the solid body [234, 235]. Potapov et al. solved a particulate flow problem using this approach for solid boundaries [236]. The second technique for imposition of solid boundary condition is to use the so-called mirror SPH particles. These particles have the same properties as the fluid SPH particles and provide a mirror effect on the other side of the solid boundary [229, 237]. As a result, when a fluid particle approaches the solid boundary and attempts to leave the domain, a mirror particle does the same and attempts to enter the domain, hence imposing enough force to avoid the fluid particle from penetrating the boundary. Shao reported that

although this approach produces acceptable results, it can be computationally expensive [238]. Also, this approach may encounter difficulty for geometrically complex solid surfaces [227]. The third technique is to use a set of boundary particles which exert repulsive forces to the neighbouring fluid SPH particles. The repulsive force is obtained from either the Lennard-Jones force [226] or gradient of the kernel function and to obtain satisfactory results, the repulsive force function must be chosen carefully [227].

2.4.7 **Numerical time integration**

To simulate the fluid flow each individual particle is moved through time by a global fixed time step. There are three different integration schemes, which will be explained in the following sections.

2.4.7.1 Euler scheme

In implicit Euler scheme the position is updated by Equation (24), however in explicit Euler scheme in addition to the position, velocity is updated in parallel by Equation (25) [239].

$$r_{t+\Delta t} = r_t + \Delta t V_t \tag{24}$$

$$V_{t+\Delta t} = V_t + \Delta t a_t \tag{25}$$

where a is acceleration and V is velocity. The semi-implicit Euler is no longer independent of the position and velocity updates, where the velocity update is the same as Equation (25), but the position update employs the result from the velocity update to calculate the new position [239].

$$r_{t+\Delta t} = r_t + \Delta t V_{t+\Delta t} \tag{26}$$

2.4.7.2 Verlet scheme

The Verlet scheme method initiates from molecular dynamics, and is based on the implicit Euler. The current velocity can be obtained using the forward first-order difference operator on positions given by [239].

$$V_t \approx \frac{r_t - r_{t-\Delta t}}{\Delta t} \tag{27}$$

Substituting Equation (25) into Equation (26) and using Equation (27) as the current velocity, the new position can be obtained as following.

$$r_{t+\Delta t} = r_t + \Delta t\,(V_t + \Delta t a_t) = r_t + \Delta t\left(\left(\frac{r_t - r_{t-\Delta t}}{\Delta t}\right) + \Delta t a_t\right)$$
$$= 2r_t - r_{t-\Delta t} + \Delta t^2 a_t \tag{28}$$

The Verlet scheme, Equation (28), is one of the computationally fastest integrators and it is generally stable, as the velocity is given implicitly [239].

2.4.7.3 Leap-Frog scheme

The integration structure in the leap-frog scheme, which has got its name from the fact that the velocities leap over the positions, is implicit Euler and yields:

$$r_{t+\Delta t} = r_t + \Delta t V_{t+1/2\Delta t} \tag{29}$$

$$V_{t+1/2\Delta t} = V_{t-1/2\Delta t} + \Delta t a_t \tag{30}$$

with the initial velocity offset determined by an Euler step:

$$V_{-1/2\Delta t} = V_0 - \frac{1}{2}\Delta t a_0 \tag{31}$$

The velocity at time *t* can be calculated by a midpoint approximation [239].

$$V_t \approx \frac{V_{t-1/2\Delta t} + V_{t+1/2\Delta t}}{2} \tag{32}$$

Therefore, to solve the set of derived equations in time, a two-step predictor–corrector procedure is employed. First, velocity V and density ρ at the intermediate time step, denoted by *, are evaluated. Pressure will be updated using ρ^* in Equation (13). Then the

intermediate velocity and density are corrected, and the new values of velocity, density and position are computed as the average of the intermediate and corrected values [227].

2.4.7.4 Neighbour searching algorithm

In the SPH method, only a limited number of particles are inside the support domain of dimension *kh* for the target particle, which are applied in the particle approximations. These particles in the support domain are usually mentioned to as nearest neighbouring particles (NNP) for that target particle. The procedure of detecting the nearest particles is known as nearest neighbouring particle searching (NNPS) [240]. Unlike a grid based numerical method, where the position of neighbour grid-cells are well defined once the grids are given, the nearest neighbouring particles in the SPH for a given particle can vary with time. The different NNPS approaches which can be used in SPH implementations include all-pair search, linked-list search algorithm, and tree search algorithm [83].

2.4.7.5 SPH algorithm

The SPH algorithm approximates a function and its spatial derivatives through averaging or summation over neighbouring particles. The special features in the SPH coding are generally involved under the main loop of time integration process, including the smoothing function and derivative calculation, particle interaction calculation, smoothing length evolution, spatial derivative estimation, boundary treatment, etc. A typical procedure for SPH simulation includes three main steps and some sub-steps, as below.

A. *Initialization step*: includes the input of the initial configuration of the problem geometry (dimensions and boundary conditions), discretization information of the initial geometry of particles, material properties, time step and other simulation control parameters.

B. *Main SPH step*: contains the major parts in the SPH simulation, and is implemented in the time integration loop. The following steps are required to be considered into the time integration process:

    - Nearest neighbouring particle searching (NNPS)

- Calculating the smoothing function (for the summation density approach) and its derivatives from the generated information of interaction particle pairs
- Calculating the density
- Calculating the stress term (viscous force and pressure gradient), internal forces arising from the particle- particle interactions, and the body forces
- Updating particle momentum, density, particle position, velocity, and checking the momentum conservation

C. *Output step*: the time step reaches to a prescribed one or at some interval, the resultant information is saved for later analyses or post-processing.

2.5 Conclusion

To summarize, in micro-packed beds (µPB) as a consequence of channel-to-particle diameter ratio being sufficiently small, the flow mal-distributions and wall friction are non-negligible. There are some correlations for correcting the permeability for the 'wall effect', however, their application to packed beds where this ratio is small such as in the case of µPBs is less good due to wall effects and porosity inhomogeneities. Furthermore, they are not always well suited to beds whose porosity deviates substantially from around fifty percent; something that we will show is an issue also for micro-packed beds. Also, they are far from perfect in that it appears as if they are not entirely generalised. Thus, a method that allows the determination of pressure drop in micro-packed beds in a general way is needed. As the amount of data available for such systems is scarce, in part due to the challenges of measuring the pressure drop in microfluidic channels, modelling has a part to play here.

Explicit numerical simulation (ENS) of flow in porous structure is concerned with numerically solving the momentum conservation equations of the interstitial fluid inside the domain defined by the pore walls. ENS requires two key elements: a model of the porous structure, particularly the pore space in which the fluid flows; and a method for solving for the flow within the porosity under a pressure gradient. Among some broad approaches relevant to build 3D models of the porous structure of packed beds, X-ray

micro-tomography is the best method. It has the advantage of being able to reveal the transport processes occurring within the pore space, in addition to resolving the bed structure that yields the pore space with modest prices in comparison with other methods. A critical step in using X-ray micro-tomography images to reconstruct a 3D image of the solid structure and the pore space defined by it, is finding the grey level (the threshold) that defines the boundary between solid and void. Whilst this threshold-identification issue is more an annoyance in many cases, it becomes a major issue for µPBs as the resolutions of bench-top X-ray micro-tomography systems are typically of the order of much of the pore space. Based on this need, a new method will propose for the accurate reconstruction of the structure of a µPB from X-ray micro-computed tomography data in Chapter 3 and Chapter 4 of this thesis.

The most broadly used approach to analyse the motion of a fluid within a complex heterogeneous structure is to use computational fluid dynamics (CFD) to solve the motion of a fluid mathematically from a set of governing equations. Using traditional mesh-based CFD methods to study flow in pores spaces encountered with some challenges. The first and most major issue is the difficulties faced in meshing the complex geometry of the pore space; constructing a grid for irregular or complex geometry has never been an easy task, which can be even more computation costly than solving the problem itself. Another main constraint is the relatively large meshes which are produced relative to computational resources typically available. On the other hand, mesh-free methods are alternative approaches to avoid the mentioned challenges around meshing the pore space. The advantage of mesh-free particle method is that by defining a suitable pore space, it is not needed to mesh the computational geometry, in addition to the fact that these methods are reasonably uncomplicated in numerical implementation, especially in comparison with grid based methods. The mesh-free method also overcomes the challenges normally faced when seeking to discretise the complex three-dimensional pore space of the packed bed. In Chapter 5 of this thesis, a meshless computational fluid dynamics technique to study fluid flow through µPBs, including determination of their permeability and the by-pass fraction due to wall effects, which are important in these beds, will report.

Chapter 3: **A new method for reconstruction of the structure of micro-packed beds of spherical particles from desktop X-ray microtomography images, Part A. Initial structure generation and porosity determination**

Moein Navvab Kashani[1], Vladimir Zivkovic[2], Hamideh Elekaei [1], Mark J.Biggs[1,3*]

1. School of Chemical Engineering, the University of Adelaide, SA 5005, Australia.
2. School of Chemical Engineering and Advanced Materials, Newcastle University, Merz Court, Newcastle-upon-Tyne, NE1 7RU, UK.
3. School of Science, Loughborough University, Loughborough, LE11 3TU, UK.

This is the version of the paper as it was submitted to *Chemical Engineering Science, Elsevier*.

* m.biggs@lboro.ac.uk

Statement of Authorship

Title of Paper	A new method for reconstruction of the structure of micro-packed beds of spherical particles from desktop X-ray microtomography images. Part A. Initial structure generation and porosity determination
Publication Status	☐Published ☐Accepted for Publication ☒Submitted for Publication ☐Publication Style
Publication Details	*Chemical Engineering Science*

Author Contributions

By signing the Statement of Authorship, each author certifies that their stated contribution to the publication is accurate and that permission is granted for the publication to be included in the candidate's thesis.

Name of Principal Author (Candidate)	Moein Navvab Kashani		
Contribution	Designed and performed experiments and modeling. Processed and undertook bulk of data interpretation. Prepared manuscript as primary author.		
Signature		Date	26/05/2015

Name of Co-author	Vladimir Zivkovic		
Contribution	Assisted with laboratory experiments and data interpretation. Reviewed final manuscript.		
Signature		Date	26/05/2015

Name of Co-author	Hamideh Elekaei		
Contribution	Assisted with data interpretation and manuscript preparation.		
Signature		Date	26/05/2015

Name of Co-author	Mark J. Biggs		
Contribution	Supervisor. Advised on experimental design, modelling, and data interpretation. Advised on manuscript preparation, revised manuscript, and corresponding author.		
Signature		Date	25/05/15

Abstract

Micro-packed beds (μPBs) are seeing increasing use in the process intensification context (*e.g.* micro-reactors), in separation and purification, particularly in the pharmaceutical and bio-products sectors, and in analytical chemistry. The structure of the stationary phase and of the void space it defines in such columns is of interest because it strongly influences performance. However, instrumental limitations – in particular the limited resolution of various imaging techniques relative to the particle and void space dimensions – have impeded experimental study of the structure of μPBs. We report here a new method that obviates this issue when the μPBs are composed of particles that may be approximated by monodisperse spheres. It achieves this by identifying in successive cross-sectional images of the bed the approximate centre and diameter of the particle cross-sections, replacing them with circles, and then assembling them to form the particles by identifying correlations between the successive images. The new method does not require specification of a threshold for binarizing the images and preserves the spherical geometry of the packing. The new method is demonstrated through its application to a packing of a near-monodispersed 30.5 μm particles of high sphericity within a 200 μm square cross-section column imaged using a machine capable of 2.28 μm resolution. The porosity obtained was, within statistical uncertainty, the same as that determined *via* a direct method whilst use of a commonly used automatic thresholding technique yielded a result that was nearly 10% adrift, well beyond the experimental uncertainty. Extension of the method to packings of spherical particles that are less monodisperse or of different regular shapes (*e.g.* ellipsoids) is also discussed.

Keywords: Micro-packed capillary; micro-packed bed; process intensification; porosity; X-ray microtomography; thresholding.

3.1 Introduction

Micro-packed beds (μPBs) are seeing increased use as miniaturization of processes becomes more prevalent. For example, they provide a means of greatly enhancing mixing and, thus, heat and mass transfer in the laminar flows that are inevitable in the microchannels encountered in process intensification [14, 28, 94, 106, 241]. They also bring an increased surface area-to-volume ratio that is useful if the particles within the bed are to act as an adsorbent or catalyst [109, 110]. The small test volumes and short residence times also make μPBs ideal for rapid, high-throughput catalyst screening [16, 111], and in the liquid chromatography context in the pharmaceutical sector [242]. They are also of relevance to micro-fluidized beds [243-246] in that they are clearly formed from packed beds. Beyond the process engineering context, μPBs are used in Micro Total Analysis Systems (μTAS), which have long been used for chemical and biochemical analysis [247], including in clinical chemistry (also known as lab-on-a-chip or LOC) [17-20].

Spherical particles are commonly used to form μPBs as they tend to ease the formation of more homogeneous bed structures that are known to give the best heat and mass transfer performance [248]. Use of smaller particles relative to the microchannel size also improves bed structure homogeneity as well as reduce 'wall effects' [248], which lead to the fluid preferentially channelling along the walls rather than passing through the bed. However, as pressure drop and, therefore, pumping power tends to increase as the particle size drops [249-251], a trade-off in the particle-to-microchannel size must be accepted. In order to assess this trade-off as well as other issues related to the structure of the μPBs, a capacity to gain detailed understanding of the bed structure as a function of the particle characteristics and preparation conditions would be useful.

A variety of techniques have been used to study the structure of μPBs. A number of workers have used scanning electron microscopy [77-79] and transmission electron microscopy [176, 177]. These techniques are, however, tedious to extend to quantitative characterization of the three-dimensional (3D) structure of μPBs. Such analysis is possible using magnetic resonance imaging (MRI) [178, 179], scanning confocal microscopy [180], and X-ray microtomography [80]. The last one has the advantage of being able to reveal

the transport processes occurring within the pore space in addition to resolving the bed structure that yields the pore space. It is, however, limited to systems containing protons (i.e. either the solid phase or void space must be proton-containing), and requires access to expensive-to-buy and operate machines as well as the expertise to run them. These issues are not faced with scanning confocal microscopy but it can only probe the order of 100 μm or so into media [181]. X-ray microtomography offers a balance between the two methods: it can be used to image the entirety of a wide variety of materials, and easy-to-use bench-top systems are now available at modest prices [182]. This technique has been used in a non-destructive way to study macroscale packed beds [193, 194], porous tissue scaffolds [184, 185], bone [186, 187], stone, rock, minerals and fossils [188], food products [189], and foams [190, 196] amongst other materials [191].

X-ray microtomography yields a series of planar digital greyscale images along an axis of a sample (e.g. along the length of a packed bed). When the size of the pixels in these images is small compared to the characteristic dimensions of the pore space and particles, the underlying geometry (e.g. spherical if bed is composed of spheres) is easily discerned. This is, however, not the case for μPBs where the resolution is comparable to the characteristic dimensions – here, instead, a sense of the underlying geometry is largely lost as illustrated in Figure 3-1, which shows a raw image and its binarized counterpart of a cross-section through a μPB composed of essentially spherical particles.

A second major issue in using typical X-ray microtomography imaging, which is encountered when seeking to reconstruct the 3D structure of μPBs, is the conversion of the grayscale images into their binary counterparts as shown in Figure 3-1. This requires the identification of the grey level (the ‘threshold’) that allows the partitioning of the pixels between the solid and void phases [202-205]. Many thresholding algorithms have been developed over the years [203, 206-209], reviews for which may be found in [210, 211, 252]. The plethora of these algorithms reflects the non-trivial nature of finding a threshold, and that there is no single algorithm that is successful for all problems. This threshold-identification issue is more a problematic, when the pixel size is much smaller than the system characteristic dimensions. However, it becomes a major issue for μPBs where a small change in the threshold leads to significant shifts in pixels from one phase to the other.

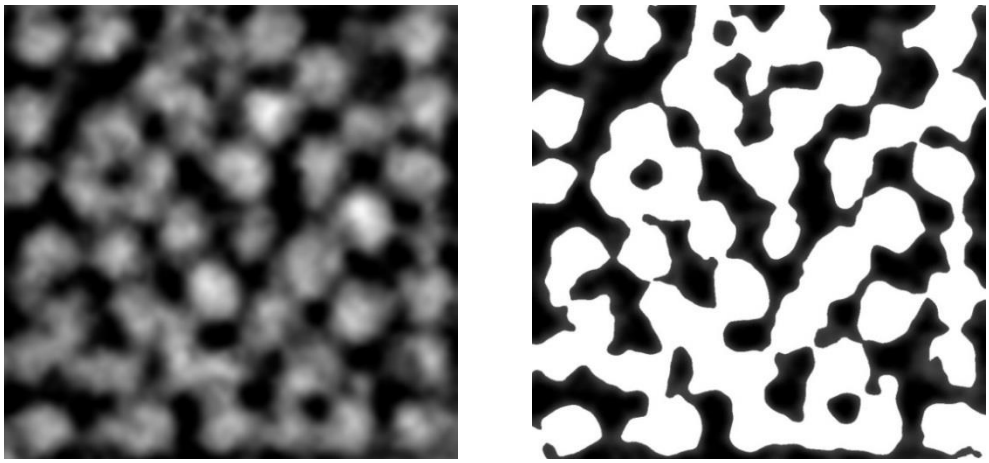

(a) (b)

Figure 3-1 Typical images of a cross-section of a μPB composed of near-monodisperse 30.5 μm diameter particles of high sphericity as derived from X-ray microtomography: (a) raw greyscale image; and (b) a binarized version of the raw image obtained using the Otsu [208] automatic thresholding algorithm.

Here we propose an approach to constructing 3D models of μPBs of near-spherical particles from X-ray microtomography images of them that avoids the two issues outlined immediately above. The method essentially involves two parts: (A) identifying approximate positions of the particles of the packing, and (B) 'relaxing' the particle packing from the first part using a Reverse Monte Carlo technique combined with simulated annealing. We provide details of the first part in this paper and demonstrate its validity by comparing the porosity obtained from the non-relaxed packing with a directly measured porosity. The second part and its application are outlined in an accompanying paper.

3.2 Description of the new method

The new method is composed of Parts A and B; attention here is restricted to the Part A, whilst the second part will be detailed in an accompanying paper, referred to as Part B hereafter. Part A is composed of the four steps that are summarized in Figure 3-2. The first two are applied to all the cross-sectional X-ray microtomographic images obtained along the length of the packing, Figure 3-2(a). The final two steps involve integration of the data

from all the cross-sectional images to form the 3D model. The four steps here have been implemented using the MATLAB Image Processing Toolbox [253] and ImageJ [254]. Integration of the functionality of these two pieces of software was achieved using MIJ, the MATLAB-ImageJ bi-directional communication package [255].

3.2.1 **Step 1. Pre-processing**

This step is applied independently to all *N* cross-sectional images. An image is first cropped to include only the region of interest (ROI), which normally is defined as that area within the μPB walls as illustrated in Figure 3-2(b). Smoothing is then applied to the image to supress as much noise [200, 201] as possible without destroying the edges of the solid phase; this is done by applying a symmetric 2-dimensional Gaussian filter of 3×3 pixels size and variance 0.5 to the image, Figure 3-2(b)→(c). An un-sharp mask is then applied to sharpen the edges without overly enhancing any noise remaining in the image [209] as shown in Figure 3-2(c)→1(d); this involves applying an average filter to the image, subtracting a blurred (un-sharp) version of the image from itself, and then adding the difference to the original image. Finally, the edges of the solid phase as detected by the X-ray microtomography are identified by applying a Sobel mask filter in combination with a Laplacian of Gaussian (LoG) filter in the two Cartesian directions, Figure 3-2(d)→(e). The use of the LoG, which is a form of second-derivative filter, is motivated by the fact that the Sobel filter is commonly misled by noise, creating false edges [256]. Application of the Sobel and LoG filter together leads to an image like that shown in Figure 3-2(e). As indicated by the red circles in this figure, there are still some solid areas whose size and location relative to others suggest they should not be stand-alone – these are dealt with in the next step of the method.

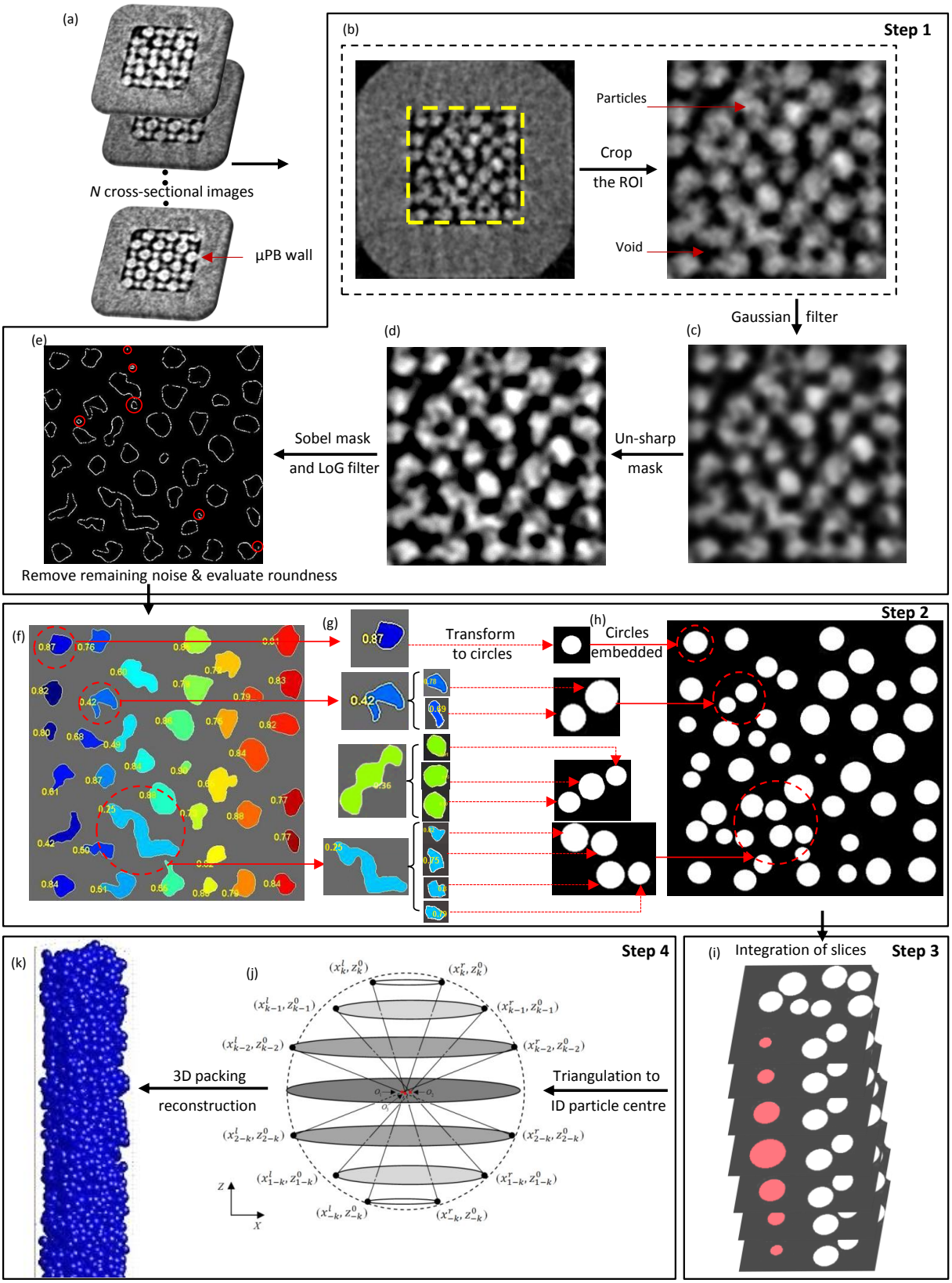

Figure 3-2 The steps of the new method to construct a 3D model of a µPB from X-ray microtomographic images of the bed.

3.2.2 **Step 2. Identifying particle cross sections in the cross-sectional images**

If the spherical particles were well resolved, the solids regions revealed by Step 1 would be circular in nature. As Figure 3-2(e) shows, however, this does not occur for μPBs because the resolution of X-ray microtomography is limited relative to the particle sizes typical of μPBs. To address this issue, two successive operations are applied independently to all the cross-sectional images.

In the first of these operations, the solid regions in an image that are far from circular in nature are subdivided into a number of regions that each are sufficiently circular to be considered as part of a single particle. This is done by first evaluating the 'roundness' of each solid region within the image using the expression

$$R_{O_i} = 4\pi \frac{A_i}{P_i^2} \tag{1}$$

where P_i and A_i are the perimeter and area of the region-i, respectively. A perfect circle has a roundness of unity whilst, as seen in Figure 3-2(f), it takes on a value less than this for any other shape. Experimentation showed here that the roundness can be used to determine the number of particles merged within a single solid region as follows

$0.65 \leq Ro \leq 1 \rightarrow$ region $\in$ single particle (2a)

$0.4 < Ro \leq 0.65 \rightarrow$ region $\in$ two particles (2b)

$0.3 < Ro \leq 0.4 \rightarrow$ region $\in$ three particles (2c)

$0 < Ro < 0.3 \rightarrow$ region $\in$ four particles (2d)

If any but condition (2a) applies for a region, Watershed segmentation using the distance transform [252] is employed successively on the region and the 'off-spring' regions derived from it until their roundness falls within the condition (2a), Figure 3-2(g).

Once all solid regions within the image have been determined to belong to a single particle, the image is subject to the second operation in this step, which sees each region replaced by a circle centred at the centroid of the region, Figure 3-2(h). The circle radius is determined by matching the area of the region with that which is closest to the cross

section selected from a sphere that has been sliced up into K segments ($K = d_p/R$) as illustrated in Figure 3-3, where d_p is the experimentally determined average diameter of the particles, and R is the inter-plane resolution of the X-ray microtomography machine used.

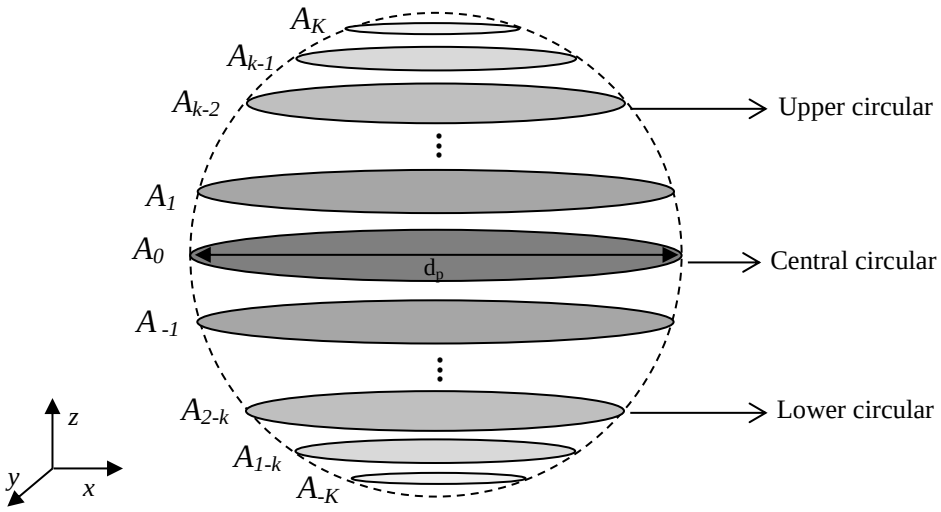

Figure 3-3 Partitioning of a spherical particle into sequential circular planes of area A_i for i = 0, ±1, …, ±K, where A_i=A_{-i}

3.2.3 **Step 3. Initial reconstruction of the bed particles**

This step sees all the particles in the μPB reconstructed by drawing correlations between circles in successive images starting from the top-most image. The top of a new particle is identified in an image when a circle of area A_K (or A_{K-1} in recognition of the finite resolution) is detected, Figure 3-3. Appropriate circles in the successive images are added to the particle until its bottom is detected, which occurs when a second circle of area A_K (or, if this is not detected, A_{K-1}, in recognition of the finite resolution) is detected after passing through circles of initially increasing and then decreasing area with a maximum in between of A_0.

3.2.4 **Step 4. Estimating the centroid of the bed particles**

For each particle, i, in the μPB the coordinates of its centroid are finally estimated by applying triangulation to the slices identified for the particle

$$X_i = \frac{\sum_{j=1}^{K} x_j}{K} \tag{3a}$$

$$Y_i = \frac{\sum_{j=1}^{K} y_j}{K} \tag{3b}$$

$$Z_i = \frac{\sum_{j=1}^{K} z_j}{K} \tag{3c}$$

Where

$$x_j = \left(\frac{(x_j^l z_{-j}^0 - z_j^0 x_{-j}^r)\left(x_{-j}^l - x_j^r\right) - (x_j^l - x_{-j}^r)(x_{-j}^l z_j^0 - z_{-j}^0 x_j^r)}{(x_j^l - x_{-j}^r)(z_{-j}^0 - z_j^0) - (z_j^0 - z_{-j}^0)(x_{-j}^l - x_j^r)} \right) \tag{3d}$$

$$y_j = \left(\frac{(x_j^l z_{-j}^0 - z_j^0 x_{-j}^r)\left(y_{-j}^l - y_j^r\right) - (y_j^l - y_{-j}^r)(x_{-j}^l z_j^0 - z_{-j}^0 x_j^r)}{(x_j^l - x_{-j}^r)(z_{-j}^0 - z_j^0) - (z_j^0 - z_{-j}^0)(x_{-j}^l - x_j^r)} \right) \tag{3e}$$

$$z_j = \left(\frac{(x_j^l z_{-j}^0 - z_j^0 x_{-j}^r)\left(z_{-j}^l - z_j^r\right) - (z_j^l - z_{-j}^r)(x_{-j}^l z_j^0 - z_{-j}^0 x_j^r)}{(x_j^l - x_{-j}^r)(z_{-j}^0 - z_j^0) - (z_j^0 - z_{-j}^0)(x_{-j}^l - x_j^r)} \right) \tag{3f}$$

The $\left(x_j^m, y_j^m, z_j^m\right)$ in Equation (3d)-(3f) are the coordinates of the m^{th} peripheral point on circle $j=1,\ldots,K$ as illustrated in Figure 3-4 for the *x*-*z* plane. The uncertainty associated with these coordinates is also estimated in the form of the standard deviation from the average; this uncertainty is used in Part B. By continuing this procedure over the whole length of µPB, the 3D structure of packing will be obtained as presented in Figure 3-2(k).

3.3 Experimental details for demonstrating the new technique

The new technique is demonstrated here by using it to reconstruct the packing of near-monodisperse 30.5 µm particles of high sphericity within a square cross-sectioned micro-capillary and estimating the porosity which is compared to the actual porosity determined directly.

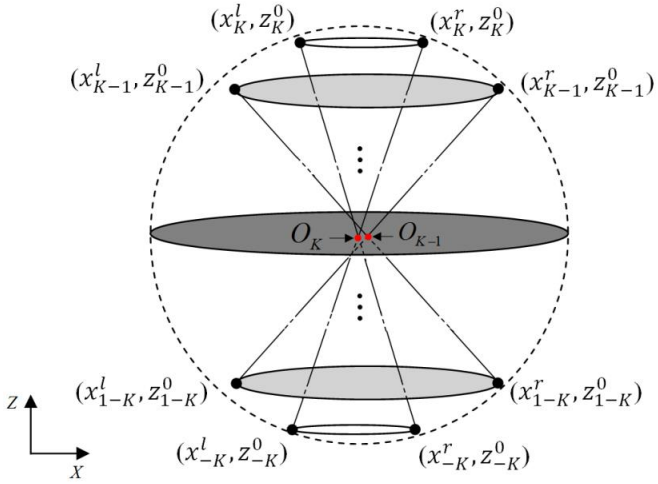

Figure 3-4 An illustration of the triangulation procedure in the *x*-*z* plane. The lines between the opposite edges of circles ±*k* intersect to yield an estimate of the sphere centroid O_k. The average centroid and the standard deviation (uncertainty) are derived from the set of these centroid points.

3.3.1 **Experimental setup**

The µPB was composed of a borosilicate micro-capillary of $D = 200$ µm internal square cross-section and 100 µm thick walls packed to a height of between 40-45 mm with soda-lime glass particles (Cospheric LLC; CA, USA) of average diameter $d_p = 30.5$ µm with a 1.5 µm standard deviation and sphericity of more than 95%. Figure 3-5(a) illustrates the method used to fill the µPB with the particles. A custom-built glass connector, details of which are provided in Figure 3-5(b), was used to connect a funnel to the top of the micro-capillary. The bottom of the micro-capillary was embedded within a wickable surface (double sided adhesive tape) so as to quickly and effectively remove the ethanol used to initially suspend the glass particles from the micro-capillary, leaving behind the dry µPB of interest here. The micro-capillary was initially filled with ethanol before some of the particle-in-ethanol suspension was poured into it whilst being tapped to enhance particle settling. This process was repeated until the micro-capillary was filled to between 40-45mm deep.

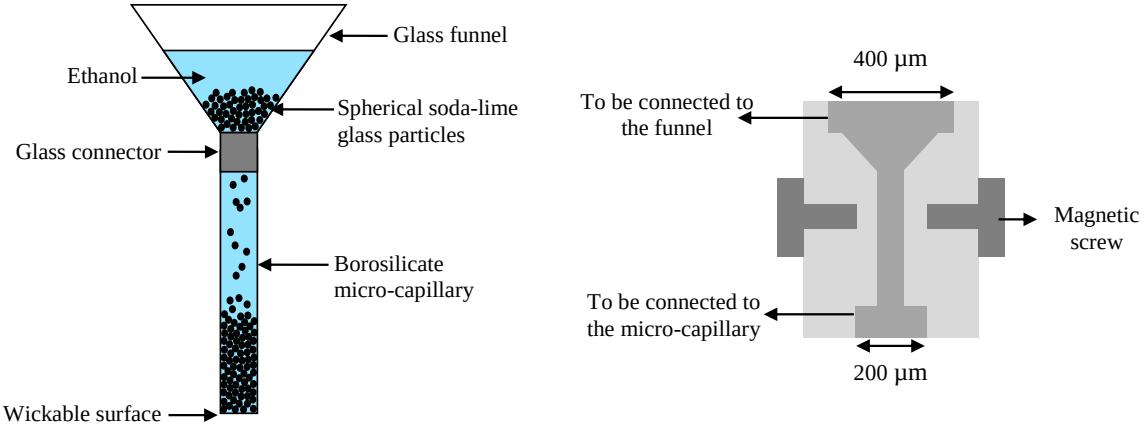

(a) (b)

Figure 3-5 (a) Schematic of method for making micro-packed capillaries (µPBs) considered here; (b) the details of custom-built glass rig used for packing the µPB.

A SkyScan1072 X-ray microtomography system (SkyScan, Belgium) was used (see Table 3-1 for relevant details of this system and the scanning parameters for the study). The radiographic images were saved in TIFF format.

Table 3-1 The X-ray microtomography system and scanning parameters

Parameters	Value
In-plane and vertical spatial resolutions	2.28 µm
Angular rotation step	0.45 degree
Rotation step	180 degree
Magnification	137.17
Source (Tension/Current)	55/110 kV/µA
Exposure time	2.7 ms
Filter material	Al 0.5 mm
Frame averaging	3

3.3.2 **Evaluating the porosity from the reconstructed µPB**

The porosity of reconstructions of µPBs was estimated *via* Monte Carlo (MC) integration. This involves depositing M points randomly within a reconstructed packed bed and counting the number that fall within the particles, M_S, and then using

$$\phi_{MC} = 1 - M_S / M \tag{4}$$

In the study here, M = 2450000 points was found to give a stable estimate of the porosity. The final porosity estimate and its uncertainty were obtained from 10 repeats of the MC integration.

3.3.3 **Direct measurement of the porosity of the μPB**

The actual porosity of the μPB was determined directly by measuring the mass of the glass particles in the bed and converting this to a solid volume using the density of the glass (2500 kg/m^3), and then dividing by the total measured volume of the bed. The volume of the bed was set equal to the product of the cross sectional area of the micro-capillary and the height of the packing, which was measured with a precision of 15 μm using a microscope. The mass of the glass particles was estimated as the difference between average mass of the μPB and the empty micro-capillary, both of which were measured using a high-precision balance (Sartorius AG Semi-microbalance, Germany; 0.01 mg precision). Their average mass in each case was that of ten separate measurements.

3.4 Results and Discussion

Figure 3-6(a) shows the cross-section obtained from the new method that corresponds to that shown in Figure 3-1. It is clear from this figure that the underlying spherical geometry is retained in the reconstruction. Figure 3-6(b) shows, however, that the 3D structure obtained *via* the new method includes some overlapping particles, which are shaded. This reflects the uncertainties associated with the identification of the centres of the particle cross-sections in each image as well as the assumption that the particles are spheres of identical size. These two issues will be addressed in Part B.

Figure 3-7(a) shows the 3D reconstruction of the μPB considered here along with some close-ups of the model. Comparing this to the structure obtained using the traditional thresholding approach; Figure 3-7(b), clearly shows the new method described here retains the underlying spherical geometry whilst the traditional approach does not. Detailed inspection of the structure obtained by the new method reveals the differences in the particle packing between the wall and interior of the bed, compare Figure 3-7(c) and (d), something that is not the case from the traditional image as seen in Figure 3-7(e) and (f). Whilst the new method yields structures that are more intuitive, they are not perfect in that

there are examples of where particles are overlapping each other or the micro-capillary wall, Figure 3-7(g) and (h), or are suspended in mid-air as seen in Figure 3-7(i).

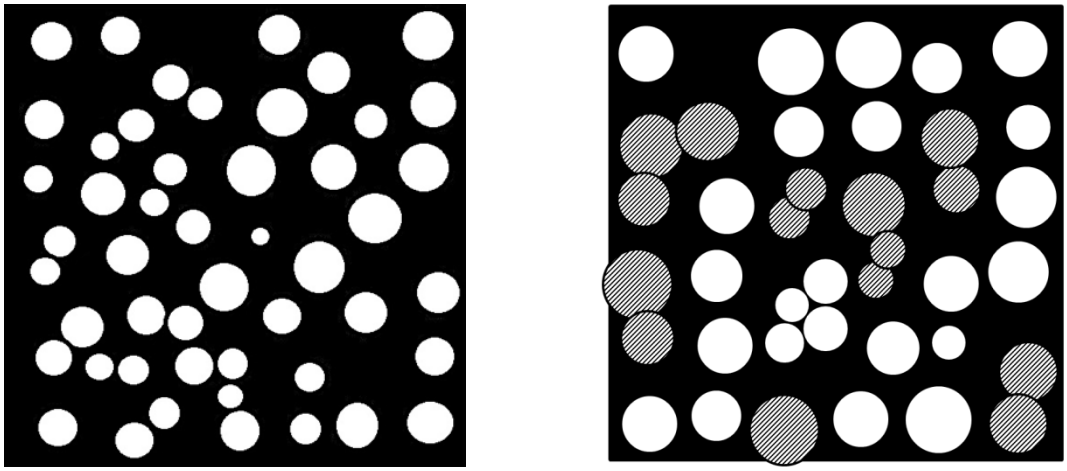

(a) (b)

Figure 3-6 Cross-sections derived from the new method: (a) that which corresponds to Figure 1; and (b) one that includes particles that overlap with each other and the bed walls (shaded circles) due to the reasons explained in the text.

As shown in Table 3-2, the porosity obtained from applying MC integration (ϕ_{MC}) over the reconstruction of the μPB is, within statistical uncertainty, the same as that obtained from the direct measurement (ϕ_D). The same cannot be said, however, for the porosity obtained from applying MC integration to the reconstructions yielded through application of the Otsu automatic thresholding method [208], which is one of the most widely used thresholding methods at present. In this case, the estimated porosity is around 9.7% lower, significantly outside the error margins associated with the direct measurement method.

Table 3-2 Porosity values (%) obtained with different methods

ϕ_T[1]			ϕ_{MC}[2]	ϕ_D[3]
Manual		**Automatic**		
60%	70%	80%		
37.3	40.6	42.3	48.5±1.6	52±2

1. Porosities derived from binarized images using different greyscale thresholds selected either manually or via the automatic Otsu method [208].
2. Porosity derived from applying Monte Carlo integration to the model built using the new method described here.
3. Porosity obtained via direct measurement of the actual μPB.

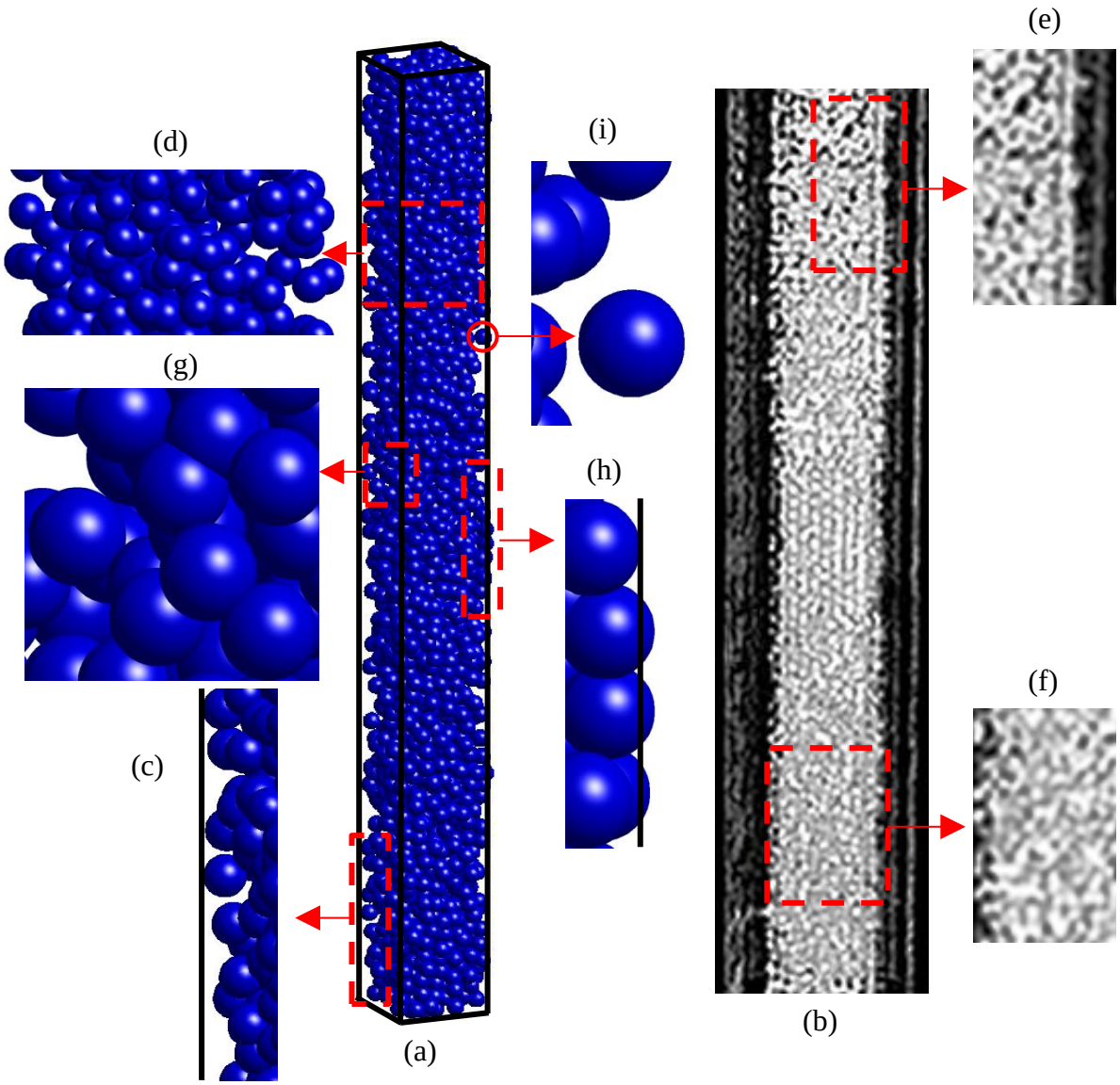

Figure 3-7 3D reconstruction of the μPB with (a) traditional thresholding approach; (b) processed micro-CT images with the new model; near wall area with this model (c) and thresholding approach (e); middle of bed with this model (d) and thresholding approach (f); overlap of particle-particle (g) and particle wall (h); and a suspended particle (i).

As anticipated in the Introduction to this paper, Table 3-2 also reveals that when thresholding is used as a basis for reconstructing a model of the μPB, the porosity changes substantially with the threshold used. The increase in porosity with the threshold value is linear, with the rate being around 0.25% *per* percent-grayscale. Thus, using a greyscale threshold of 60%, the error in the voidage is around 15%, decreasing to around 10% for the threshold yielded by the Otsu automatic thresholding method [208] (*i.e.* 80%).

Although the porosity yielded using the 3D structure obtained from the new method here cannot be statistically differentiated from the actual, it is lower than these values. This trend arises from the fact that the 3D structure yielded by the method includes overlapping particles, and particles overlapping with the micro-capillary walls as shown in Figure 3-7. This issue will be addressed in Part B. Although we have applied the new method to a μPB composed of near-monodisperse particles of high sphericity, it is conceivable that it can be applied to less-ideal beds. For example, dispersion in spherical particle sizes, including multimodal particle sizes could be considered by selecting appropriately from a library of circular cross-sections in Step 2, rather than just the one as done here, in conjunction with establishing cross-correlations between slices. Extension to beds composed of particles whose cross-sections are elliptical in nature is also possible if this is done provided the roundness metric in Equation (1) and the associated criteria in Equation (2) are generalised.

3.5 Conclusion

Whilst benchtop X-ray microtomography systems can yield three-dimensional (3D) images of the structure and porosity of packed beds, they are generally of poor quality when the beds are part of microfluidic devices due to the low resolution of the X-ray systems relative to the dimensions of the particles and porosity. This manifests as a loss of the underlying particle geometry and the conversion of the grayscale images into binary counterparts being sensitive to the greyscale threshold used to partition the pixels between the solid and void phases. A new method is described here that obviates both these issues when the micro-packed beds (μPBs) are composed of largely monodisperse particles of high sphericity. The method has been demonstrated by applying it to a μPB. The recovered structure appears reasonable and has a porosity that is, within experimental uncertainty, equal to the value measured directly. In comparison, use of the well-known Otsu automatic thresholding method to partition the greyscale images into solid and void regions yielded a model in which the underlying spherical geometry and various other structural details were destroyed, and a porosity that was nearly 10% less than the actual. Whilst the new, alternative method described herein offers a major improvement over such commonly used methods, the monodispersity assumption and uncertainties associated with locating particle

centres in the packing means anomalies are present in the models yielded here; for example, some overlapping particles. A method for addressing this issue is outlined in Part B of this work.

Chapter 4: **A new method for reconstruction of the structure of micro-packed beds of spherical particles from desktop X-ray microtomography images, Part B. Structure refinement and analysis**

M. Navvab Kashani,[1] V. Zivkovic,[2] H. Elekaei,[1] L.F. Herrera,[3] K. Affleck,[1] M.J. Biggs[1,4,*]

1. School of Chemical Engineering, the University of Adelaide, SA 5005, Australia.
2. School of Chemical Engineering and Advanced Materials, Newcastle University, Merz Court, Newcastle-upon-Tyne, NE1 7RU, UK.
3. School of Engineering and Information Technology, Charles Darwin University, NT 0909, Australia.
4. School of Science, Loughborough University, Loughborough, LE11 3TU, UK.

This is the version of the paper as it was submitted to *Chemical Engineering Science*, *Elsevier*.

* m.biggs@lboro.ac.uk

Statement of Authorship

Title of Paper	A new method for reconstruction of the structure of micro-packed beds of spherical particles from desktop X-ray microtomography images. Part B. Structure refinement and analysis
Publication Status	☐Published ☐Accepted for Publication ☒Submitted for Publication ☐Publication Style
Publication Details	*Chemical Engineering Science*

Author Contributions

By signing the Statement of Authorship, each author certifies that their stated contribution to the publication is accurate and that permission is granted for the publication to be included in the candidate's thesis.

Name of Principal Author (Candidate)	Moein Navvab Kashani		
Contribution	Performed experiments, analysis and simulation. Processed and undertook bulk of data interpretation. Prepared manuscript as primary author.		
Signature		Date	26/05/15

Name of Co-author	Vladimir Zivkovic		
Contribution	Assisted with results analysis and data interpretation. Reviewed final manuscript.		
Signature		Date	26/05/15

Name of Co-author	Hamideh Elekaei		
Contribution	Assisted with data interpretation and manuscript preparation.		
Signature		Date	26/05/15

Name of Co-author	Luis F. Herrera		
Contribution	Assisted with Monte Carlo Integration coding and data interpretation.		
Signature		Date	26/05/15

Name of Co-author	Kathryn Affleck		
Contribution	Assisted with sample preparation.		
Signature		Date	25/05/15

Name of Co-author	Mark J. Biggs		
Contribution	Supervisor. Advised on experimental design, modelling, and data interpretation. Advised on manuscript preparation, revised manuscript, and corresponding author.		
Signature		Date	25/05/15

Abstract

The authors have reported elsewhere [257] a new method that derives models of micro-packed beds (μPBs) of near-spherical particles from X-ray microtomography grayscale images of limited resolution compared to the characteristics dimensions of the particles and porosity. The new method is distinguished by it not requiring a grayscale threshold to partition the images into solid and void phases, and its retention of the underlying spherical geometry, two issues that are particularly problematic when more traditional approaches are used to build models of μPBs. Here it is shown that a reverse Monte Carlo (RMC) algorithm combined with simulated annealing (SA) can refine the models obtained from this new method to eliminate particle overlaps and incorporate particle size distributions. Application of the RMC-SA to an initial model of a μPB yielded a porosity estimate that was, within experimental uncertainty, the same as its directly measured counterpart. It was further shown that the porosity of μPBs is near unity at the bed wall and oscillates in a decaying fashion normal to the wall up to a distance of around three particle diameters into the bed. This leads to the porosity decreasing with increasing channel-to-particle diameter ratio. The opposite was observed, however, for the average number of particle-particle contacts (the mean coordination number). This latter behaviour has two origins: a volumetric one in which the bulk of the bed where the coordination number is maximal and constant exerts increasing influence, and a packing one in which the packing density inherently decreases with the channel-to-particle diameter ratio.

Keywords: Microfluidics; micro-packed bed (μPB); porosity; mean coordination number; wall effect; Reverse Monte-Carlo and simulated annealing.

4.1 Introduction

Packings of near-spherical particles of 10s of microns diameter or smaller within channels of a few 100s of microns or less are commonly used in microfluidic applications ranging from microanalysis [22-26] through to process intensification [7-10]. Understanding the variation of the three-dimensional (3D) structure of such micro-packed beds (µPBs) as a function of the material characteristics and preparation conditions is critical to optimizing their performance [248]. There are a variety of experimental methods available for imaging the 3D structure of µPBs, but one of the most convenient is benchtop X-ray microtomography due to its modest cost and ease of use. However, its limited resolution relative to the porosity and particles in µPBs presents significant challenges when seeking to transform microtomography images of such beds into 3D models suitable for detailed quantitative analysis. The first challenge is the identification of an appropriate threshold for turning the grayscale images obtained from X-ray microtomography such as that shown in to Figure 4-1(a) into a binary image of solid and void only as shown in Figure 4-1(b) and (c). The second challenge is the loss of the underlying spherical geometry as also clearly demonstrated in Figure 4-1.

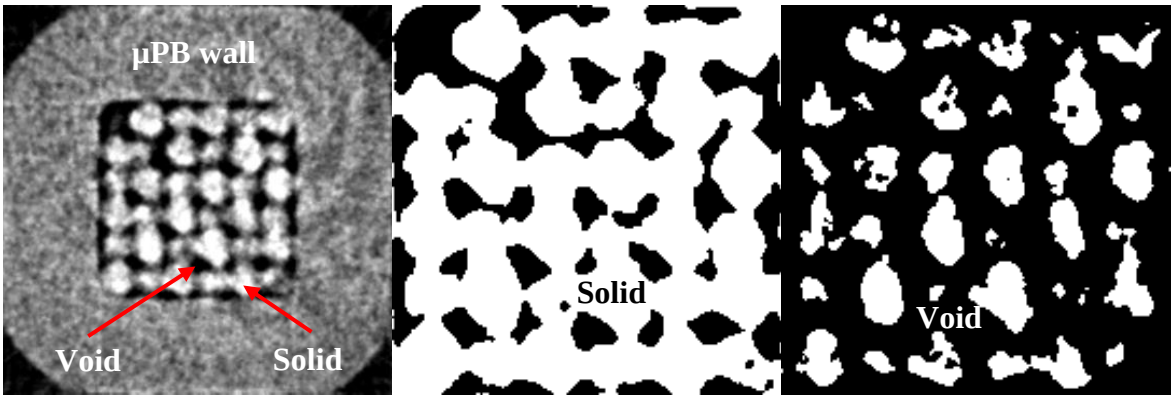

(a) (b) (c)

Figure 4-1 X-ray microtomography related images of a cross-section through a µPB composed of 38.5 µm diameter particles of high sphericity within a 200 µm square capillary: (a) raw grayscale image ; (b) a binarized version of the greyscale image using a threshold of 60% of the grayscale range; and (c) a binarized version of the greyscale image using a threshold identified by the Otsu [208] method (80% of the grayscale range).

In the first part of this two-part contribution [257], hereafter referred to as Part A, we have outlined a method for converting benchtop X-ray microtomography grayscale images for µPBs into 3D models of sphere packings that does not rely on the identification of a grayscale threshold for partitioning the pixels between the solid and void phases. It was shown that this new method can yield a model of a µPB whose porosity is, within experimental error, equal to the directly measured counterpart. The models obtained by the method outlined in Part A are, however, imperfect in that they include particles that overlap each other and the channel walls, and particles that have no contact with any other particle. This reflects the fact that the method for identifying the particle positions is subject to some uncertainty and the particle sizes are all assumed equal to the experimentally determined mean (*i.e.* the particle sizes are not distributed as would be the case in reality). Here we detail the use of a Reverse Monte Carlo (RMC) simulation [258] combined with Simulated Annealing (SA) [259] to refine the structure obtained from the method described in Part A to address these two issues. The approach is first described and then demonstrated by using it to determine the porosity and topology of µPBs of near-spherical particles as a function of the particle-to-bed diameter.

4.2 Description of the new method

In order to eliminate particle-particle and particle-wall overlaps and suspended particles, Reverse Monte Carlo (RMC) was combined with Simulated Annealing (SA) to shift the particle size distribution (PSD) towards the experimentally-determined distribution and move the particle positions within the confines of their uncertainty. This involved repeatedly applying with equal probability the following two types of 'moves' to randomly selected spheres in the model derived from the method described in Part A:

1. **Changing the size of the particle** by an amount δd within the constraints of the experimental PSD

$$\delta d = \delta d_{max}(\xi - 0.5) \quad (1)$$

where $\delta d_{\max}$ is the maximum possible change in the diameter allowed, and ξ is a random number selected in a uniform way from the range [0,1).

2. **Displacing the position of the sphere** in the three coordinate directions by δx_α within the degree of uncertainty associated with the estimated positions of the sphere centroid

$$\delta x_\alpha = \delta x_{\alpha,max}(\xi_\alpha - 0.5) \quad (2)$$

where $\delta x_{\alpha,max}$ is the maximum possible displacement allowed in the α-coordinate direction, and ξ_α are corresponding random numbers independently selected in a uniform way from the range [0,1).

The maximum particle diameter change and displacement allowed were adapted so as to yield a move acceptance ratio (the ratio of accepted moves to total attempted moves) of between 30 and 50%.

Each attempt at a move was accepted provided a random number selected uniformly from the range [0,1) was less than the probability given by [260]

$$P = \min(1, \exp[-\Delta F/T]) \quad (3)$$

where ΔF is the change the move would create in the functional we are seeking to minimise if accepted, and T is a 'temperature' that decreases monotonically during the course of the simulation; the cooling rate over two successive steps of $T(s)/T(s-1) = 0.9$ was used in the work reported here. Equation (3) ensures the move is always accepted if it brings a decrease or no change in the functional (*i.e.* $\Delta F \leq 0$) whilst allowing for it to also be accepted with a probability less than unity if the functional will increase with the move (*i.e.* $\Delta F > 0$). The use of the monotonically decreasing 'temperature' means the chances of such an 'uphill step' in F being accepted decreases from a maximum at the start of a simulation, all else being equal.

The functional that was minimized is

$$F = W_{pp}F_{pp} + W_{pw}F_{pw} + W_pF_p + W_sF_s \quad (4)$$

where the F_i and W_i are sub-functionals and associated weights, respectively, that relate to the differences that must be minimised in the simulation. The first term in this equation seeks to eliminate the particle-particle overlaps within the bed

$$F_{pp} = \sum_{ij} \left(\frac{D_{ij}}{d_{ij}} \right)^2 \tag{5}$$

where the summation is over all particle pairs, and D_{ij} is their overlap given by

$$D_{ij} = \begin{cases} \left\| \mathbf{x}_i - \mathbf{x}_j \right\| - d_{ij} & \text{if } \left\| \mathbf{x}_i - \mathbf{x}_j \right\| < d_{ij} \\ 0 & \text{if } \left\| \mathbf{x}_i - \mathbf{x}_j \right\| \geq d_{ij} \end{cases} \tag{6}$$

where $\mathbf{x}_i$ and $\mathbf{x}_j$ are the vectors defining the centroids of the particles *i* and *j* relative to an origin, and d_{ij} is the minimum distance that may exist between them in the absence of an overlap, which is given by the sum of the particle radii

$$d_{ij} = \frac{d_i + d_j}{2} \tag{7}$$

The second term in Equation (4) is similarly aimed at eliminating the particle overlaps with the confining walls of the µPB

$$F_{pw} = \sum_{iw} \left(\frac{D_{iw}}{d_i} \right)^2 \tag{8}$$

where the summation is over all particle-wall pairs, and D_{iw} is their overlap given by

$$D_{iw} = \begin{cases} (\hat{\mathbf{n}}_w \cdot \mathbf{x}_i + p_w) - d_{iw} & \text{if } (\hat{\mathbf{n}}_w \cdot \mathbf{x}_i + p_w) < d_{iw} \\ 0 & \text{if } (\hat{\mathbf{n}}_w \cdot \mathbf{x}_i + p_w) \geq d_{iw} \end{cases} \tag{9}$$

where $\hat{\mathbf{n}}_w$ is the unit normal to the wall-*w* and p_w its distance from the origin, and d_{iw} is the minimum distance that may exist between the particle and wall in the absence of an overlap, which is given by the particle radius

$$d_{iw} = \frac{d_i}{2} \tag{10}$$

The penultimate term in Equation (4), which is aimed at limiting the displacement of the particle centroids to within a region around their initial position commensurate with its uncertainty, is of the form

$$F_p = \sum_i D_{i0} \tag{11}$$

where the summation is over all particles, and D_{i0} is the amount the displacement of the particle from its initial position exceeds the uncertainty associated with the initial centroid position of the particle-i, which is given by

$$D_{i0} = \begin{cases} \|\mathbf{x}_i - \mathbf{x}_{i0}\| - \sigma_i & \text{if } \|\mathbf{x}_i - \mathbf{x}_{i0}\| > \sigma_i \\ 0 & \text{if } \|\mathbf{x}_i - \mathbf{x}_{i0}\| \leq \sigma_i \end{cases} \tag{12}$$

where $\mathbf{x}_{i0}$ is the position of the particle in the initial 3D structure obtained from the method described in Part A, and σ_i is the standard deviation associated with this position.

The final term in Equation (4) is aimed at minimising the difference between the experimental particle size distribution and that of the particle ensemble in the 3D model. It does this by considering the deviation between the mean, μ, standard deviation, σ, and skewness, κ, of the two distributions

$$F_s = \frac{(\mu_e - \mu_m)^2}{\mu_e^2} + \frac{(\sigma_e - \sigma_m)^2}{\sigma_e^2} + \frac{(\kappa_e - \kappa_m)^2}{\kappa_e^2} \tag{13}$$

where the subscripts e and m refer to the values from experiment and the model, respectively.

The weights for each term in Equation (4) are necessary to ensure the four terms are all of the same order. To achieve this, at the end of every 1000th step the weights were adapted by multiplying them by 1.1 or 0.9 if their associated sub-functionals were above or below the average of all the sub-functionals.

4.3 Application of the new method

The new approach was applied to models of µPBs constructed using the approach outlined in Part A. The materials were also essentially the same as in Part A except, as specified in Table 4-1, a wider range of particle and channel sizes were used to give a total of eight

different channel-to-particle diameter ratios. The PSD for the 30.5 μm sized particles, which was determined using a Mastersizer 2000 (Malvern, UK) fitted with an Hydro 2000MU dispersion unit, is shown by way of example in Figure 4-2 with its standard deviation and skewness.

Table 4-1 Characteristics dimensions of the μPBs considered in the study reported here

Micro-capillary size*, D (μm)	Particle size†, d_p (μm)	$D/\overline{d_p}$
200	38.5	5.2
200	34.5	5.8
200	30.5	6.6
200	26.5	7.6
400	38.5	10.4
400	34.5	11.6
400	30.5	13.2
400	26.5	15.2

* The micro-capillary cross-sections are square and they were filled to a depth of 50 mm.
† The standard deviation in the diameters of the soda-lime glass particles is 1.5 μm, and their sphericity 95%.

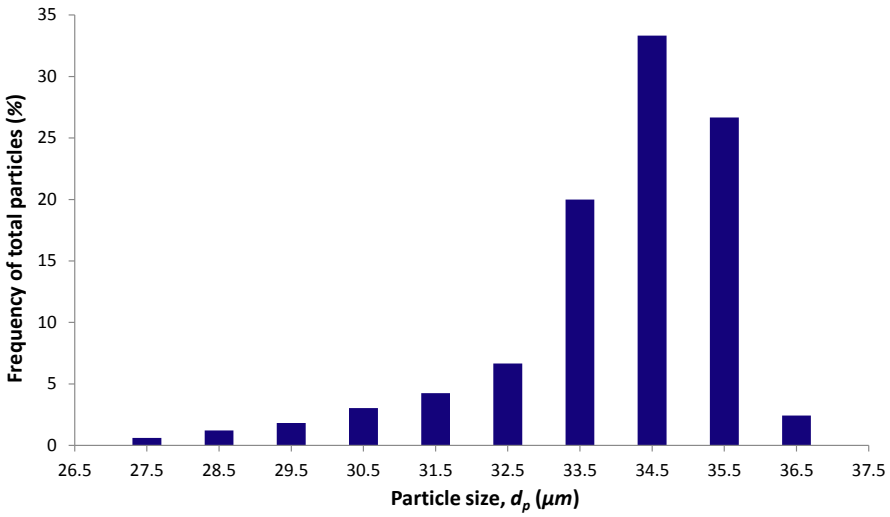

Figure 4-2 Particle size distribution (PSD) for the particles with an average diameter of 34.5 μm. The standard deviation and skewness are σ_e = 1.51 μm and κ_e = −1.63, respectively.

As in Part A, the images of the µPBs were acquired using A SkyScan1072 X-ray micro-CT system (SKYSCAN, Belgium). The reader is referred to Part A for the methodological details.

4.4 Results and Discussion

4.4.1 **Overview of initial interpretation of X-ray microtomography images of µPBs**

Figure 4-3 shows examples of cross-sectional images from the eight different µPBs considered in the study reported here; see Figure 4-1(a) for how to interpret these greyscale images. These illustrate the challenges faced in imaging the particles and pore space. In particular, the degree to which one can discern the spherical geometry diminishes rapidly as the particle size decreases much below the largest within the smallest micro-channel (*i.e.* for $D/d_p > 5.8$), and the boundary between the solid and void phases is not easily discerned.

By way of example, the transformation seen between Figure 4-4(a) and Figure 4-4(b) illustrates the outcome of application of the approach detailed in Part A to one of the cross-sectional images in the $D/\overline{d_p}$=5.2 µPB. As the circles with the red outlines highlight, some of the circular cross-sections extracted using the method of Part A lead to particle-particle and particle-wall overlaps. These can be removed by application of the methodology detailed in Section 2 above.

4.4.2 **Structural change during a RMC-SA simulation**

Figure 4-5(a) shows a typical variation of the objective function in Equation (4); the corresponding changes in the four parts that make up this objective function (not shown) are similar to what is seen here for the overall functional. The simulation in this example continued for approximately 1.3M steps before the objective function ceased to change. The values of the objective functions typically dropped to between 1-10% of the initial value, indicating the ability of the approach to substantially eliminate overlaps and bring about a particle size distribution that matches the experimental one. These changes are illustrated in the transformation seen between Figure 4-4(b) and Figure 4-4(c), and in the shift in the character of the PSD as shown in Figure 4-5(b). The latter figure clearly shows

that the PSD of the model broadens over the course of the simulation from its initial non-disperse character (black bar) to that seen experimentally (dotted bars *vs.* broken line).

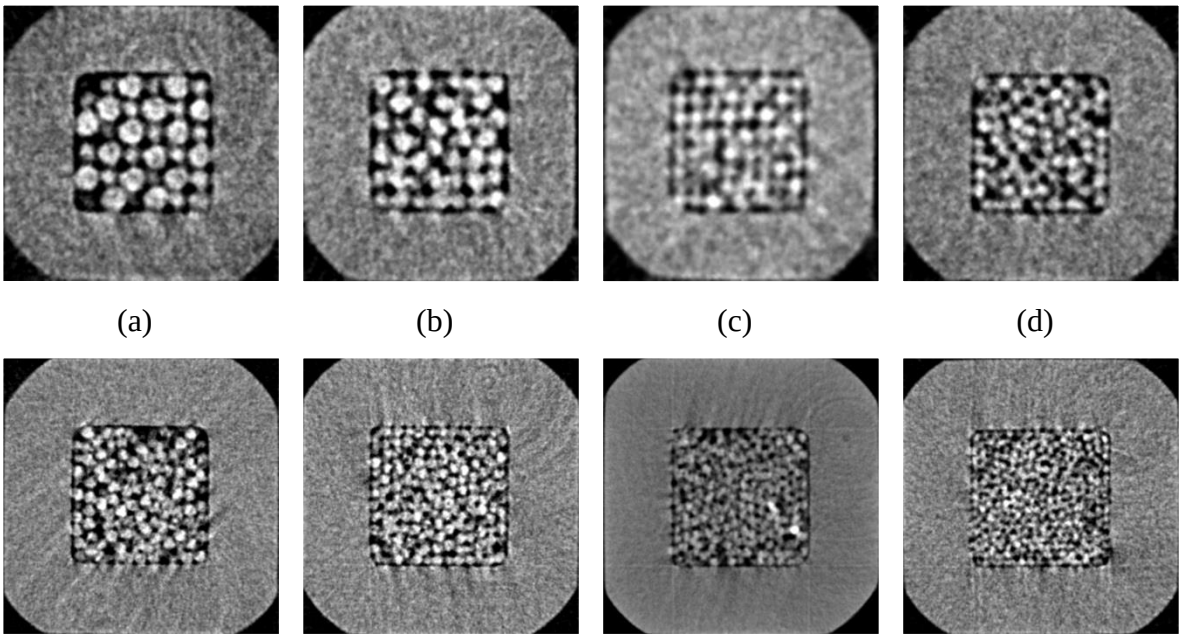

(a) (b) (c) (d)

(e) (f) (g) (h)

Figure 4-3 Example X-ray microtomography images of cross-sections of µPBs for channel-to-particle diameter ratios, $D/\overline{d_p}$, equal to (see Table 4-1 for more details): (a) 5.2; (b) 5.8; (c) 6.6; (d) 7.6; (e) 10.4; (f) 11.6; (g) 13.2; and (h) 15.2.

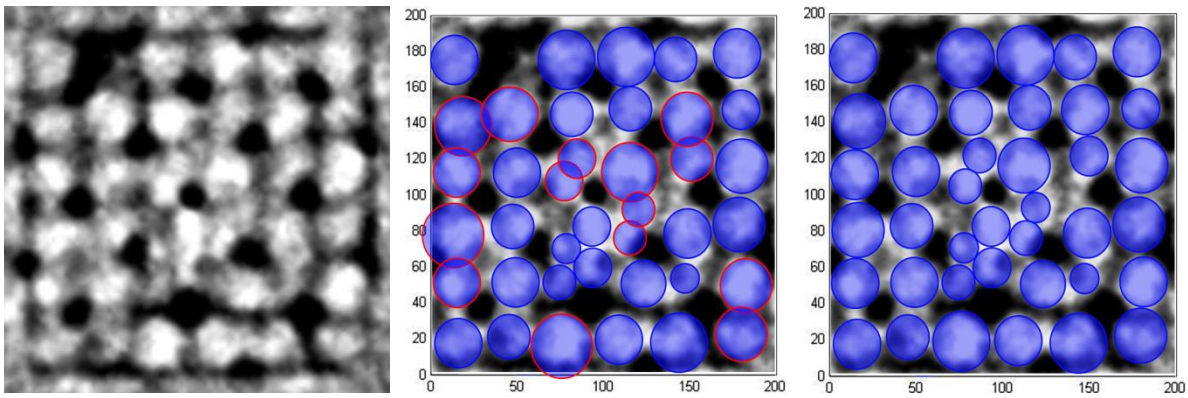

(a) (b) (c)

Figure 4-4 Example cross sections from key stages in the model construction: (a) a close-up of an X-ray microtomography image of a cross-section through the $D/\overline{d_p} = 5.2$ µPB; (b) the particle cross-sections identified through application of the methodology in Part A to the X-ray image, with the particles that are overlapping either each other or the walls shown with red outlines; and (c) the particle cross-sections shown in part (b) after application of the RMC-SA algorithm described herein to eliminate overlaps and obtain a PSD that is in line with the experimental one.

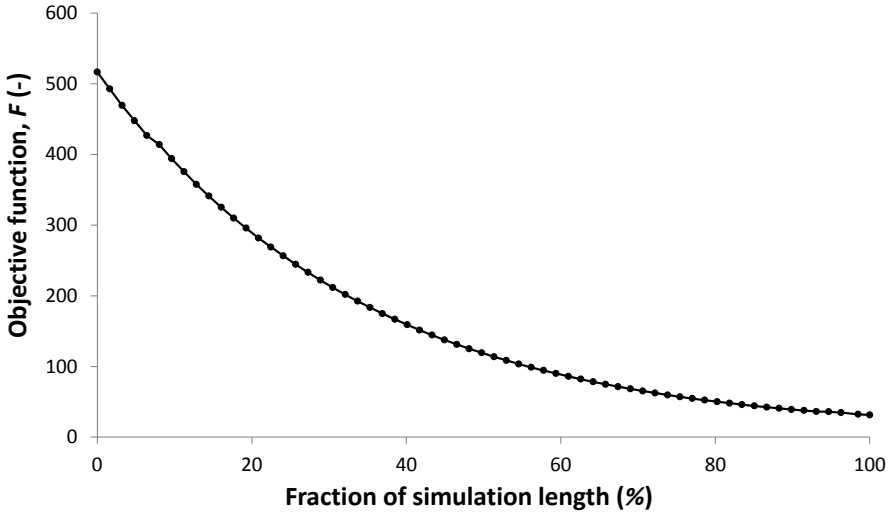

(a)

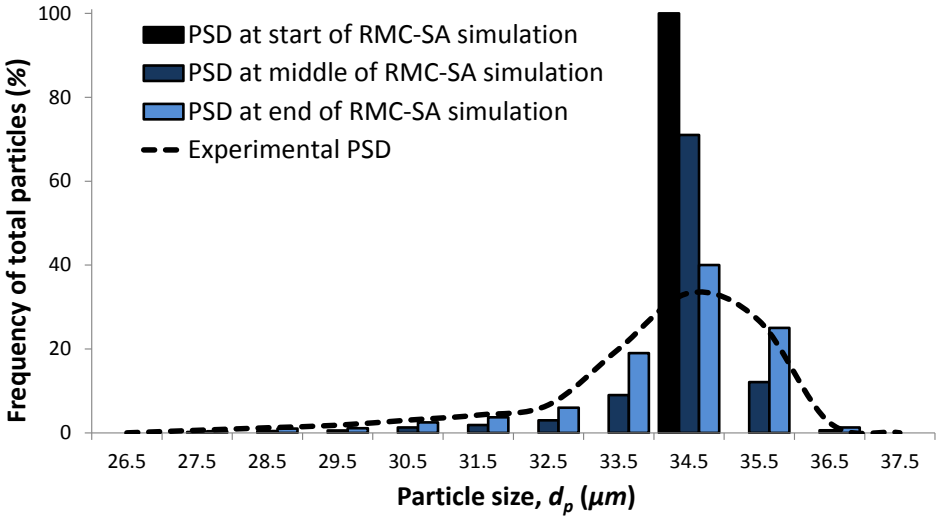

(b)

Figure 4-5 Variation of key structure-related metrics during a typical RMC-SA simulation: (a) objective function, *F*, (each point is an average over 100 steps); and (b) PSD (note the initial distribution is a single bar centred at 34.5 μm)

4.4.3 **Qualitative analysis of packing structure in μPBs**

Figure 4-6 shows a typical 3D model obtained from application of the RMC-SA algorithm on the processed images in the Part A. The random nature of the packing is revealed in the various zooms on the packing, particularly that shown in part (c). Part (e) of this figure shows the porosity is far more open near the bed wall, as anticipated. Interestingly, this part of the figure also shows that the model includes some particles that have no contacts

with surrounding particles when located near the wall. Whilst this may reflect the RMC-SA algorithm is not entirely effective in removing non-physical occurrences, they were largely observed to occur near the wall, suggesting that surface forces between the particles and the capillary wall may be playing a role, something that some of the authors here have observed in other systems [261, 262]. Although few in number, Figure 4-6(g) also shows that some particle overlaps remain at the end of the RMC-SA. These overlaps are, however, very minor in nature, with the degree of overlap being generally less than 1% (i.e. $D_{ij}/d_{ij} < 1\%$). Inspection of these defects in the model always revealed a situation where particle size and position adjustment would not remove the problem without compromising the functional, perhaps indicating that inclusion of non-spherical character may be of benefit (the sphericity of the particles was high, but not perfectly so).

4.4.4 **Quantitative analysis of porosity in μPBs**

Figure 4-7 shows the variation of the μPB porosity, determined *via* Monte Carlo integration on the reconstructed structures as described in Part A, with the channel-to-particle diameter ratio, in addition to data drawn from the literature and the value we obtained *via* direct measurement for the $D/\overline{d_p} = 6.6$ μPB (see Part A for details of this measurement). The first thing to note is the porosity obtained from the reconstructed structure of the $D/\overline{d_p} = 6.6$ μPB, $53.6 \pm 1.4\%$, is statistically the same as that determined directly, $52 \pm 2\%$. This represents a further improvement on estimating the porosity compared to what was already a significant improvement gained in Part A, providing further reassurance that the model structures obtained here are representative of the actual.

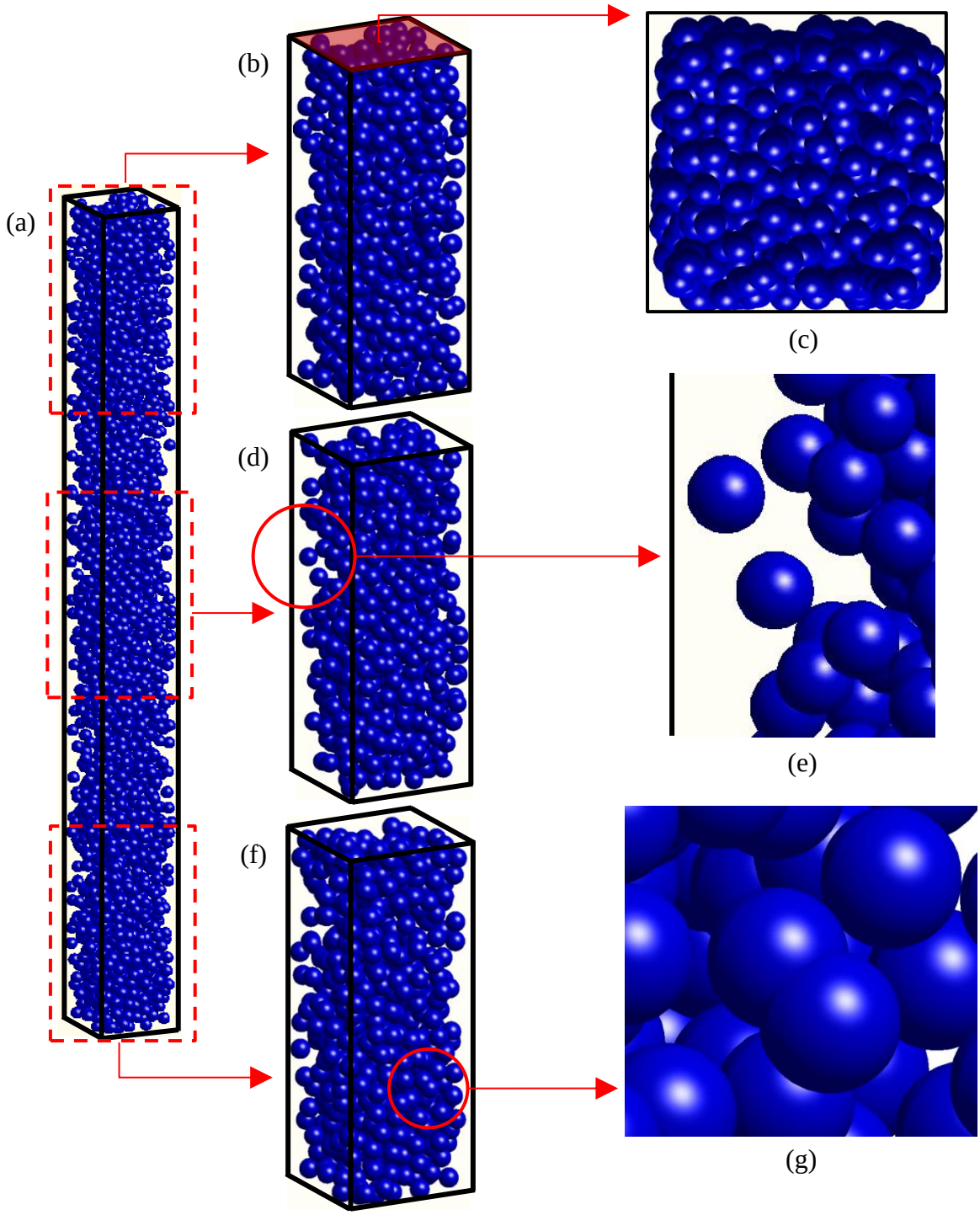

Figure 4-6 A model of the $D/\overline{d_p} = 5.2$ µPB shown from various perspectives: (a) complete bed; (b) a zoom on top third; (c) further zoom on top region of the bed to illustrate its random structure; (d) zoom on middle third; (e) further zoom on middle region of the bed to show the packing structure near the wall; (f) zoom on bottom third of the bed; and (g) further zoom on bottom region of the bed to show two particles that are still overlapping to some extent.

Figure 4-7(a) shows that the porosity of μPBs essentially decreases monotonically with bed-to-particle diameter ratio. This behaviour reflects the decreasing influence of the confining walls on the packing structure on a volumetric basis as suggested by the axially-averaged particle density maps shown in the Supplementary Information, which were derived by averaging the greyscale images obtained along the length of the μPB. This decreasing trend is not dissimilar to that seen by De Klerk [263] for a macroscale PB of circular cross section. The overall porosities are higher here, however, due at least in part to the inaccessibility of the corners of the square cross-section of our μPBs as indicated by the broken line in Figure 4-7(b), which shows the porosity is near-unity for a distance of up to ~25% of the average particle diameter from the corner. Another potential origin of the differences seen between the two data sets is the sedimentation method used to create the μPBs here, which is likely to result in a much looser packing compared to that obtained in macroscale beds where gravity effects are proportionately more significant and tapping is more effective.

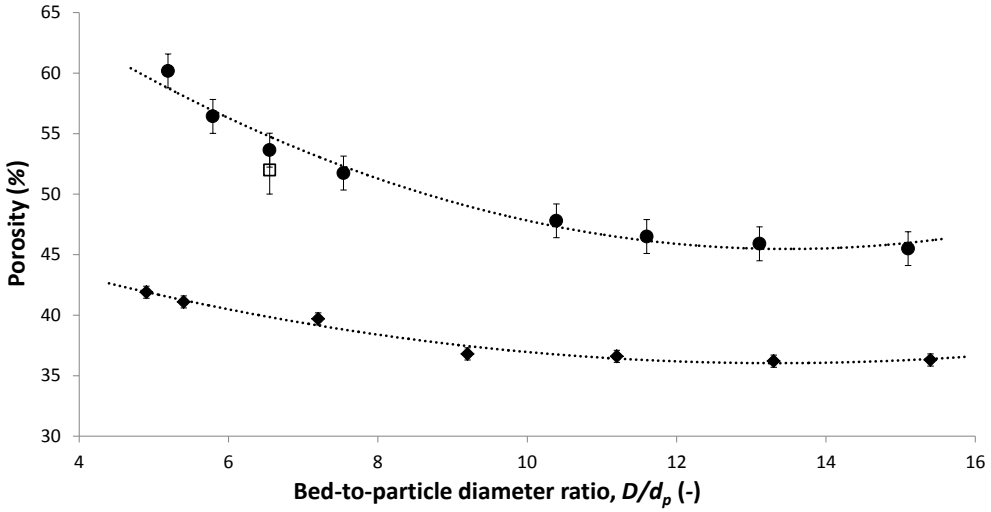

(a)

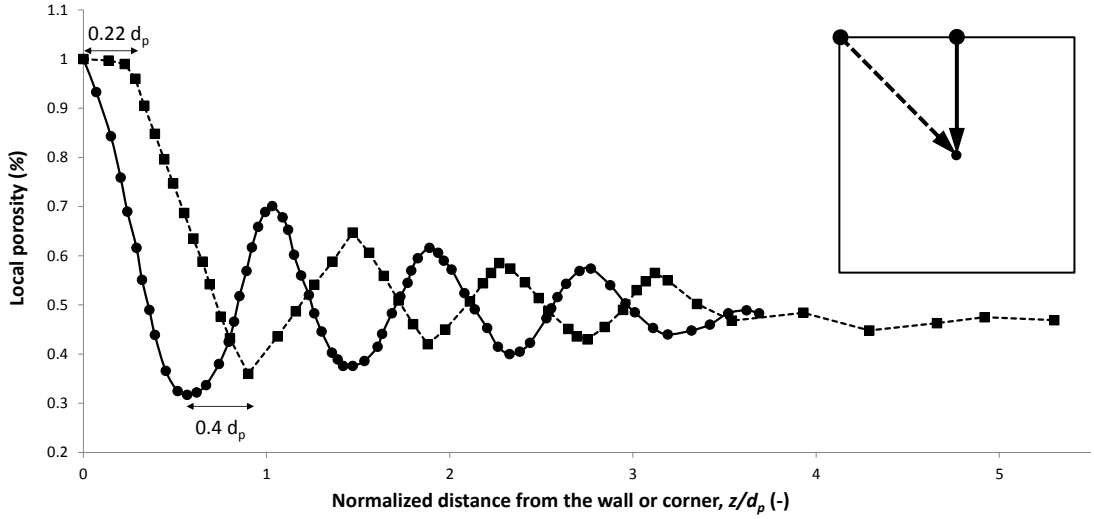

(b)

Figure 4-7 Porosity character of μPBs as derived from the models: (a) variation of porosity with the bed-to-particle diameter ratio (circles), and the direct measurement as described in Part A for the $D/\overline{d_p} = 6.6$ μPB (open square) and data obtained by De Klerk [263] for a macroscale packed beds of cylindrical cross-section (diamonds); and (b) variation of porosity with normal distance from the wall (solid line) and diagonal distance from the corner (broken line) for $D/\overline{d_p}$=7.54 (similar data for all the other μPBs are provided in the Supplementary Information). The lines are a guide for the eye only.

Figure 4-7(b) shows that the porosity variation normal to the walls is highly inhomogeneous, with the porosity oscillating significantly for up to around three particle diameters before stabilising. These oscillations are also seen in along the diagonals, although shifted by around 40% of the particle diameter. These results mean that μPBs whose bed-to-particle diameter ratio is less than 6 are dominated by these inhomogeneities (see Figure 4-S2 in the Supplementary Information for the data for all the other PBs).

The contacts between particles in a packed bed can be joined to form a network [264]. These networks are characterised by a mean coordination number, $\overline{Z}$, which represents the average number of contacts experienced by the particles in the bed. Figure 4-8(a) shows that this coordination number increases with the bed-to-particle diameter ratio in an initially non-linear manner up to a diameter ratio of around 8 before it continues to rise in what appears to be a linear manner. The mean coordination number of the μPBs whose diameter ratio exceeds around 10 take on values commensurate with those associated with

random packings of monodisperse spheres, which fall between 5.5 for 'loose packings' through to around 6.5 for 'close packings' [265]. It is not clear from the data available here if the mean coordination number will pass beyond this limit, but this may well occur due to the dispersity in the particles sizes.

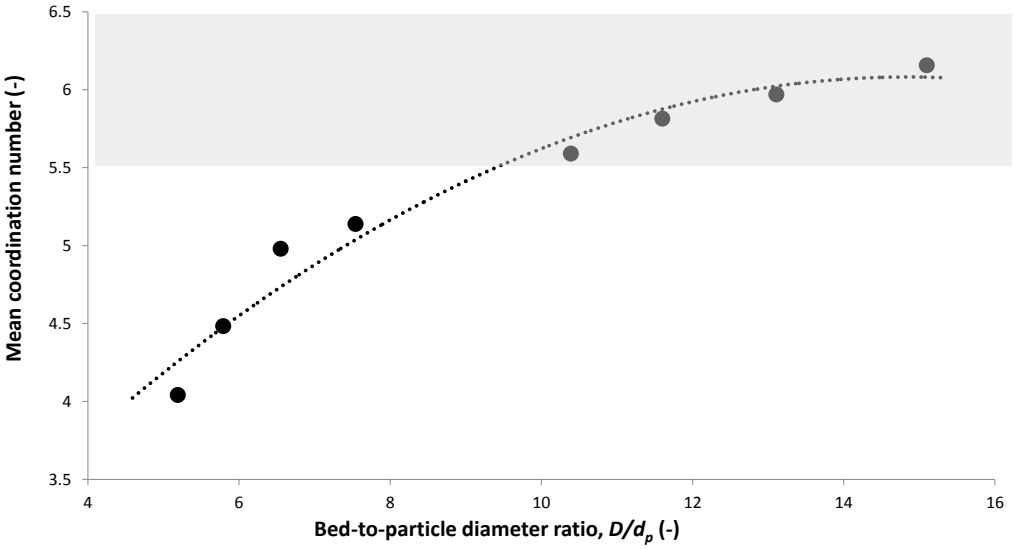

(a)

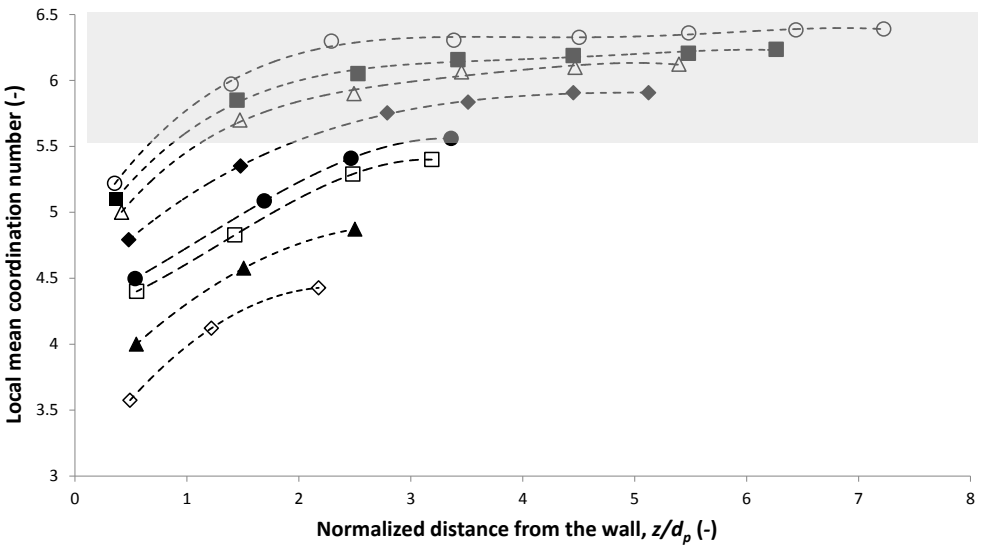

(b)

Figure 4-8 Coordination number variation with: (a) bed-to-particle diameter ratio; and (b) normalized distance from the bed wall for $D/\overline{d_p}$ =5.2 (open diamonds); 5.8 (solid triangles); 6.6 (open squares); 7.5 (solid circles); 10.4 (solid diamonds); 11.6 (open triangles); 13.1 (solid squares) and 15.1 (open circles)

This increasing trend with channel-to-particle diameter ratio can be understood by considering Figure 4-8(b), which shows the variation of the local mean coordination number with normal distance from the wall for the various μPBs considered here. This reveals that the mean coordination number increases from a minimum at the wall – as expected due to the presence of the wall on the outside of the outermost layer of particles – until it reaches a plateau in the bulk of the bed. Thus, the increasing trend seen in Figure 4-8(a) *in part* has its origins in the increasing influence the bulk of the bed has on the mean coordination number as the bed size increases relative to the particle size. The change-down in the slope seen at $D/\overline{d_p} \approx 6$ reflects the plateau in the local coordination number occurs at $z/\overline{d_p} > 3$. Figure 4-8(b) also reveals that the mean coordination number at a given normalised distance from the wall also increases with channel-to-particle diameter ratio. This clearly suggests that there is a second origin of the increasing trend see in Figure 4-8(a) beyond the volumetric one. As the values of the local mean coordination number in the bulk of the bed appear to fall between the 'loose packing' and 'close packing' limits, this suggests that the degree of packing achieved in the beds investigated here increases with the channel-to-particle diameter ratio.

4.5 Conclusions

In Part A [257], we reported a new method that derives models of micro-packed beds (μPBs) of near-spherical particles from X-ray microtomography grayscale images of limited resolution compared to the characteristics dimensions of the particles and porosity. The new method is distinguished by it not requiring a grayscale threshold to partition the images into solid and void phases, and its retention of the underlying spherical geometry, two issues that are particularly problematic when more traditional approaches are used to build models of μPBs. Whilst the models obtained from the new method provide a far better basis for estimating the porosity of μPBs, they contain defects in the form of particles that overlap each other and the bed wall, and which do not contact any other sphere ('suspended particles'). It is shown here that a reverse Monte Carlo (RMC) algorithm combined with simulated annealing (SA) can eliminate these defects by addressing the two major issues in the approach taken in Part A: (1) shifting from a single particle size (equal to the mean) to the experimentally identified particle size distribution;

and (2) refining the particle positions within constraints defined by the uncertainty in their initial determination.

A μPB model obtained *via* application of RMC-SA to an initial model built using the approach in Part A yielded a porosity that was consistent with its directly determined counterpart. This approach also yielded a variation of porosity with channel-to-particle size ratio that was consistent with this experimental data and, allowing for different bed cross-sections (square *vs.* circular) data published elsewhere. The porosity was found to be near unity at the wall of the μPBs and to vary in an oscillatory manner normal to it for up to three particle diameters into the bed. The mean coordination number was also found to vary over the same distance from the bed wall where it was a minimum. The values of the mean coordination number in the bulk of the bed fell between that associated with 'loose random packings', which occurred for the bed of the smallest bed-to-particle diameter ratio, to 'close packings' in the largest beds relative to the particles. These observations suggest there are two origins for the variation in the mean coordination number with bed-to-particle size ratio: a volumetric one in which the bulk value exerts increasing influence as the ratio increases, and the degree of packing, where this too increases with the size ratio.

4.6 Supplementary information

Figure 4-S1, which shows for the various μPB the average cross-sectional solid density maps obtained by averaging all images taken along the length of the beds, indicates the particles adjacent to the capillary walls are well ordered in all the μPBs. The rings of particles sitting immediately adjacent to the outermost ring are also well structured in all the μPB, although the ordering is not as great except for all but the three smallest bed-to-particle diameter ratios. The particles within the two outer rings are well ordered for these three smaller beds, whilst the opposite is true for the remaining μPBs. These behaviours are reflected in Figure 4-S2.

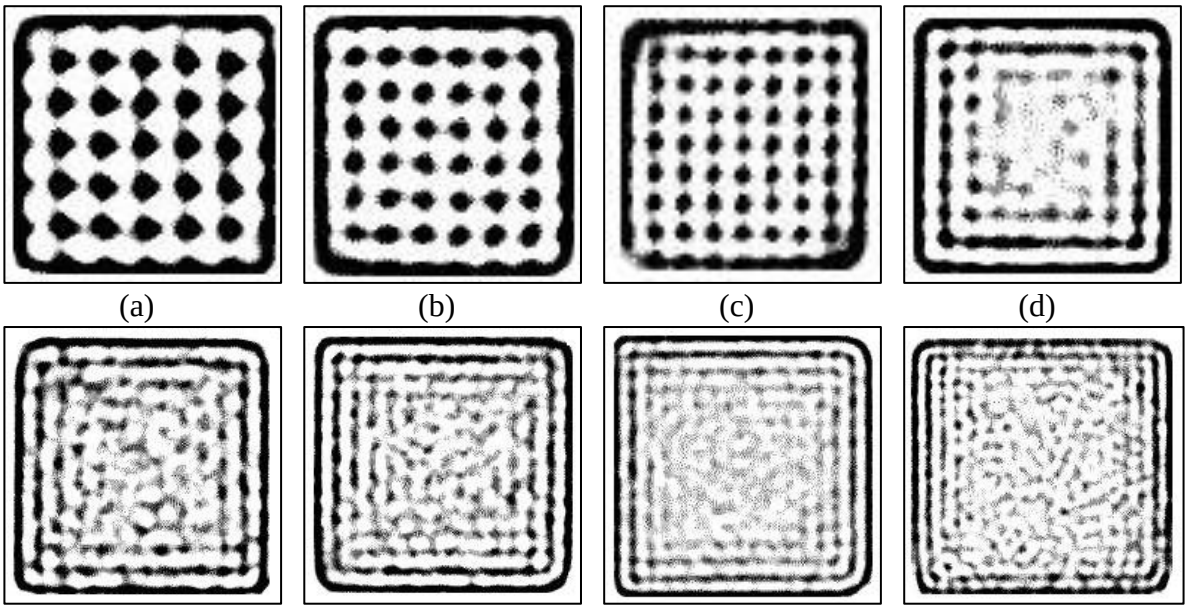

Figure 4-S1 Solid density maps obtained by averaging over the X-ray microtomography images along the µPBs for $D/\overline{d_p}$ equal to: (a) 5.2; (b) 5.8; (c) 6.6; (d) 7.5; (e) 10.4; (f) 11.6; (g) 13.1 and (h) 15.1.

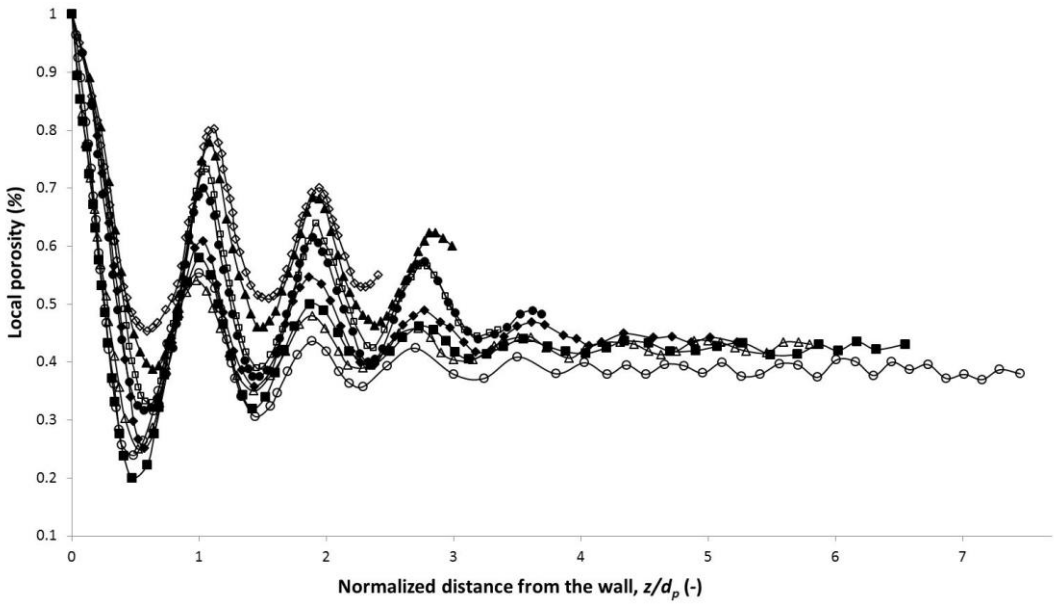

Figure 4-S2 Variation of porosity with normal distance from the wall for $D/\overline{d_p}$ =5.2 (open diamonds); 5.8 (solid triangles); 6.6 (open squares); 7.5 (solid circles); 10.4 (solid diamonds); 11.6 (open triangles); 13.1 (solid squares) and 15.1 (open circles).

Chapter 5: **Explicit numerical simulation-based study of the hydrodynamics of micro-packed beds**

M. Navvab Kashani,[1] H. Elekaei,[1] V. Zivkovic,[2] H. Zhang,[1] M. J. Biggs,[1,3*]

1. School of Chemical Engineering, the University of Adelaide, SA 5005, Australia
2. School of Chemical Engineering and Advanced Materials, Newcastle University, Merz Court, Newcastle-upon-Tyne, NE1 7RU, UK.
3. School of Science, Loughborough University, Loughborough, LE11 3TU, UK

This is the version of the paper as it was submitted to *Chemical Engineering Science, Elsevier*.

* m.biggs@lboro.ac.uk

Statement of Authorship

Title of Paper	Explicit numerical simulation-based study of the hydrodynamics of micro-packed beds
Publication Status	☐Published ☐Accepted for Publication ☒Submitted for Publication ☐Publication Style
Publication Details	*Chemical Engineering Science*

Author Contributions

By signing the Statement of Authorship, each author certifies that their stated contribution to the publication is accurate and that permission is granted for the publication to be included in the candidate's thesis.

Name of Principal Author (Candidate)	Moein Navvab Kashani		
Contribution	Developed coding and simulation. Processed and undertook bulk of data interpretation. Prepared manuscript as primary author.		
Signature		Date	26/05/15

Name of Co-author	Hamideh Elekaei		
Contribution	Assisted with code development, data interpretation and manuscript preparation.		
Signature		Date	26/05/15

Name of Co-author	Hu Zhang		
Contribution	Provided advices on simulation.		
Signature		Date	26/05/15

Name of Co-author	Vladimir Zivkovic		
Contribution	Assisted with results analysis and data interpretation.		
Signature		Date	26/05/15

Name of Co-author	Mark J. Biggs		
Contribution	Supervisor. Advised on modelling and data interpretation. Advised on manuscript preparation, revised manuscript, and corresponding author.		
Signature		Date	25/05/15

Abstract

Knowledge of the hydrodynamic character of micro-packed beds (μPBs) is critical to understanding pumping power requirements and their performance in various applications, including those where heat and mass transfer are involved. The report here details use of smoothed particle hydrodynamics (SPH) based simulation of fluid flow on models of μPBs derived from X-ray microtomography to predict the hydrodynamic character of the beds as a function of the bed-to-particle diameter ratio over the range $5.2 \leq D/d_p \leq 15.1$. It is shown that the permeability of the μPBs decreases in a non-linear but monotonic manner with this ratio to a plateau beyond $D/d_p \approx 10$ that corresponded to the value predicted by the Ergun equation. This permeability variation was reasonably well-represented by the model of Foumeny (*Intnl. J. Heat Mass Transfer,* **36,** 536, 1993), which was developed using macroscale packed beds of varying bed-to-particle diameter ratios. Five other correlations similarly determined using macroscale beds did not match at all well the SPH results here. The flow field within the μPBs varied in an oscillatory manner with radial position (*i.e.* channelling occurred at multiple radial positions) due to a similar variation in the porosity. This suggests that use of performance models (*e.g.* for heat and mass transfer) derived for macroscale beds may not be suitable for μPBs. The SPH-based approach here may well form a suitable basis for predicting such behaviour, however.

Keywords: Porous media; micro-packed bed; pressure drop; permeability; smoothed particle hydrodynamics (SPH); Lagrangian.

5.1 Introduction

Microfluidics, the science and technology utilised in the processing and manipulation of small amounts of fluids in conduits having dimensions of the order of tens to hundreds of micrometres [3, 95, 266], is a fast growing research field with a wide range of potential applications. Its genesis in the early 1990s [267] was in the form of what is now widely termed 'Micro Total-Analysis-System' (μTAS) [22, 23], which has since been employed in a range of applications in chemical and biological analysis, including in clinical chemistry [17, 19], medical diagnostics [85, 268], cell biology (*e.g.* chemotaxis studies) and immunology [87, 269]. Microfluidics is also of relevance beyond μTAS, including in colloid science [89, 270], plant biology [90, 271], and process intensification [7-9]. In the latter, specific applications include micro-chemical engineering technology [11, 91, 92, 94], which leads to higher product yields and new reaction pathways not possible in larger scale systems [3, 16, 95, 96], and control of extreme reactions [11-13, 15, 97].

Despite the many potential benefits of microfluidics, the laminar flow that arises from the small dimensions and often simple geometries involved [98, 99] means mixing and, hence, mass and heat transfer are poor [10, 100]; for example: the mixing length, which is the distance that a liquid must travel to become fully intermixed, can be of the order of centimetres or even meters, much greater than is available in typical microfluidic configurations where miniaturization is clearly the desired end-point. One way of addressing the mixing challenge is to use a packed bed, also termed a micro-packed bed (µPB) [101-103]. This approach also facilitates an increase in the surface area-to-volume ratio, which is useful if the particles within the bed are to act as an adsorbent or catalyst [28, 106, 109, 110].

Whilst µPBs take many shapes and sizes – see for example the simple, long and narrow T-shaped bed of Jensen and co-workers [105] *vs.* their more complex, wide but shallow bed elsewhere [103] – they are generally characterised by small bed-to-particle diameter ratios. This small ratio leads to the bed walls having a significant influence on the µPB behaviour compared to the typical macroscale counterparts. The higher porosity near the walls [257, 272] combined with the fact that the wall region constitutes a significant volume of µPBs means significant fluid flow may tend to channel along the walls [117, 118]. Further flow

inhomogeneities may also arise in beds constituted from particles of regular shape and size due to confined packing-induced oscillations in the porosity [53, 273]. These factors open up the possibility that the performance of the µPBs (*e.g.* in mixing) may be less than hoped for. They may also lead to the character of the pressure drop differing from that of typical macroscale packed beds, although opinion appears mixed on this point (see [53, 124] vs. [47, 125] vs. [44]). Given the pumping power required to overcome pressure drop is a significant issue in the microfluidic context, as is its performance under any circumstances, it is clearly desirable to be able to predict the hydrodynamic character of µPBs.

Given the flow in microfluidic devices is in general laminar, it is anticipated that the relationship between the flow rate through a µPB and the pressure drop, Δp, along its length, *L*, will be described by Darcy's Law, which may be expressed as

$$v = -\frac{k}{\mu}\frac{\Delta p}{L} \tag{1}$$

where v is the flow rate *per* unit cross-sectional area, often termed the superficial velocity, μ is the fluid viscosity, and *k* is the bed permeability, a characteristic related to the nature of the packing. One of the earliest permeability models is due to Ergun [45]

$$k = \frac{\varepsilon^3 d_p^2}{150(1-\varepsilon)^2} \tag{2}$$

where ε is the bed porosity and d_p the diameter of the particles that it is made up of. There are many other expressions that have also been developed for the permeability of macroscale packed beds [42, 43], but many will probably not be valid for µPBs because their much smaller bed-to-particle diameter ratio [46], D/d_p, means wall effects are likely to have greater influence. Expressions have, however, been developed for macroscale beds of smaller bed-to-particle diameter ratios. One of the earliest such permeability models is that of Mehta & Hawley [132], who derived the modified-Ergun equation

$$k = \frac{\varepsilon^3 d_p^2}{150M^2(1-\varepsilon)^2} \tag{3}$$

where M is a factor that accounts for the bed-to-particle diameter ratio

$$M = 1 + \frac{2}{3(1-\varepsilon)}\frac{d_p}{D} \tag{4}$$

As an alternative, Reichelt [127] proposed the expression

$$k = \frac{\varepsilon^3 {d_p}^2}{A_w M^2 (1-\varepsilon)^2} \tag{5}$$

where A_w is a parameter obtained from fitting the model to experimental data. Others have also used this expression more recently with other experimental data [48, 49], including Eisfeld & Schnitzlein [118], who used 2300 data points from a large number of sources. Foumeny et al. [53] used Equation (5) with the following expression

$$A_w = \frac{130}{M^2} \tag{6}$$

Combined with the diameter ratio-dependent porosity expression as

$$\varepsilon = 0.383 + 0.25\left(\frac{D}{d_p}\right)^{-0.923} \cdot \frac{1}{\sqrt{0.723\frac{D}{d_p} - 1}} \tag{7}$$

whilst Raichura [50] obtained the following *via* use of other experimental data

$$A_w = \frac{103}{M^2}\left(\frac{\varepsilon}{1-\varepsilon}\right)^2 \left[6(1-\varepsilon) + \frac{80}{D/d_p}\right] \tag{8}$$

Cheng [48] proposed the following expression based on a capillary type model

$$A_w = \frac{1}{M^2}\left[185 + 17\left(\frac{\varepsilon}{1-\varepsilon}\right)\left(\frac{D}{D-d_p}\right)^2\right] \tag{9}$$

Finally, Di Felice and Gibilaro [51] proposed a model based on a sub-division of a packed bed into two zones to yield

$$k = \frac{{d_p}^2 \varepsilon^3 (2.06 - 1.06 \left(\frac{D/d_p - 1}{D/d_p} \right)^2)}{150(1-\varepsilon)^2} \quad (10)$$

Whilst all the above expressions attempt to capture the effect of the bed-to-particle diameter ratio, they have all been determined using macroscale data; it is not known how relevant these are for µPBs.

Assessing the validity of the Equations (2)-(10) for µPBs could be undertaken through experimental means. However, determination of pressure drop in such systems is challenging due to the relatively small pressure drops and the intricacies of their measurement arising out of the miniaturisation. An alternative is to simulate the flow in models of the pore space of real µPBs. This is done here using smoothed particle hydrodynamics (SPH) [274] on models of µPBs derived from application of a method recently developed by the authors [257, 272] to X-ray tomographic images of real beds of varying bed-to-particle diameter ratios. SPH has been used as it obviates the difficult task of building meshes in the complex three-dimensional (3D) geometry of the µPB pore spaces.

The remainder of the paper is structured as follows. We first detail the governing flow equations and SPH formulation based on these along with the solution algorithm. The model is then benchmarked against the results for flow around a single sphere, which is prototypical of µPBs. Results are then presented for the µPBs and compared with expressions (2)-(9). Consideration of the correlation between the inhomogeneities in the bed porosity and localised flow profiles are also discussed before conclusions are drawn.

5.2 Model

5.2.1 **Governing equations**

Smoothed particle hydrodynamics (SPH) is based on the Navier–Stokes equations in the Lagrangian frame. For isothermal fluid flow, these equations take the form

$$\frac{d\rho}{dt} = -\rho \, \nabla . \mathbf{v} \quad (10)$$

And

$$\rho \frac{d\mathbf{v}}{dt} = \nabla . \boldsymbol{\sigma} + \rho \mathbf{g} \tag{11}$$

where ρ, $\mathbf{v}$ and $\boldsymbol{\sigma}$ are the fluid density, velocity and stress tensor, respectively, and $\mathbf{g}$ is the acceleration due to body forces at play such as, for example, gravity. The stress tensor for a Newtonian fluid may be expressed as

$$\boldsymbol{\sigma} = -P\mathbf{I} + \boldsymbol{\tau} \tag{12}$$

where, P is the hydrostatic pressure, $\mathbf{I}$ the unit tensor, and $\boldsymbol{\tau}$ the shear stress tensor that may be expressed as

$$\boldsymbol{\tau} = -\mu \left[\nabla \mathbf{v} + (\nabla \mathbf{v})^T \right] \tag{13}$$

where μ is the dynamic viscosity of the fluid.

5.2.2 **SPH formulation**

In SPH [240], the fluid is represented by a discrete set of particles of fixed mass, m_i, that move with the local fluid velocity, $\mathbf{v}_i$. The velocity and other quantities associated with any particle-i are interpolated at a position r through a summation of contributions from all neighbouring particles weighted by a function, $W(\mathbf{r}, h)$, with a compact support, h, as illustrated in Figure 5-1.

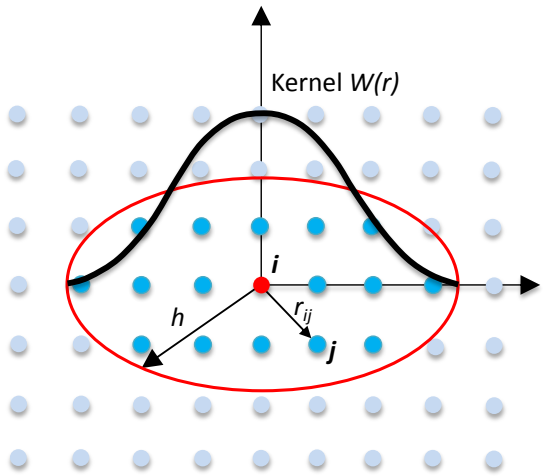

Figure 5-1 An illustration of an SPH weighting function with compact support that is used to evaluate quantities at a point r such as, for example, the density as shown in Equation (15).

For example, the density of a particle-*i* is given by [275]

$$\rho_i = \sum_j m_j \, W(r_{ij}, h) \tag{14}$$

where r_{ij} is the distance between particles *i* and *j*.

The pressure gradient associated with particle-*i* is given by [275, 276]

$$(\nabla P)_i = \rho_i \sum_j m_j \left(\frac{P_j}{{\rho_j}^2} + \frac{P_i}{{\rho_i}^2} \right) \nabla_i W_{ij} \tag{15}$$

where P_i is the pressure associated with particle-*i*.

Finally, the divergence of the shear stress tensor attached to a particle-*i* is given by [277]

$$(\nabla . \boldsymbol{\tau})_i = \rho_i \sum_j m_j \left(\frac{\boldsymbol{\tau}_j}{{\rho_j}^2} + \frac{\boldsymbol{\tau}_i}{{\rho_i}^2} \right) . \nabla_i W_{ij} \tag{16}$$

where the components of the shear stress tensor, which are derived from Equation (13), are given by

$$\tau_i{}^{\alpha\beta} = -\mu \left(\sum_j \frac{m_j}{\rho_j} \, v_{ij}^{\beta} \frac{\partial W_{ij}}{\partial x_i^{\alpha}} + \sum_j \frac{m_j}{\rho_j} \, v_{ij}^{\alpha} \frac{\partial W_{ij}}{\partial x_i^{\beta}} \right) \tag{17}$$

where $\mathbf{v}_{ij} = \mathbf{v}_i - \mathbf{v}_j$.

Combined, these equations lead to the following SPH formulation for the momentum equation

$$\frac{\mathrm{d}\mathbf{v}_i}{dt} = -\sum_j m_j \left(\frac{P_j}{{\rho_j}^2} + \frac{P_i}{{\rho_i}^2} \right) \nabla_i W_{ij} + \sum_j m_j \left(\frac{\boldsymbol{\tau}_j}{{\rho_j}^2} + \frac{\boldsymbol{\tau}_i}{{\rho_i}^2} \right) . \nabla_i W_{ij} + \mathbf{g} \tag{18}$$

A variety of weighting functions have been used over the past three or more decades [240]. The stability properties of SPH simulations strongly depend on the second derivative of the weighting function [240]. Although the cubic spline is widely employed, the piecewise-linear nature of its second derivative leads to instabilities in SPH simulations involving incompressible viscous creeping flows [240]. This can be avoided by use of higher-order splines [235, 240] such as the quintic spline that is employed here as a compromise between stability and accuracy requirements and efficiency

$$W(q,h) = \frac{3}{359\pi h^3} \times \begin{cases} (3-q)^5 - 6(2-q)^5 + 15(1-q)^5 & 0 \le q < 1 \\ (3-q)^5 - 6(2-q)^5 & 1 \le q < 2 \\ (3-q)^5 & 2 \le q < 3 \\ 0 & q > 3 \end{cases} \quad (19)$$

where $q = r/h$.

5.2.3 **Solution technique**

A two-step predictor-corrector scheme is used to solve Equation (18) based on an explicit projection method in which the pressure required to enforce the incompressibility is found *via* projecting an estimate of the velocity field onto a divergence-free space, $\nabla . \mathbf{v} = 0$, which this conforms with the continuity equation [229]. Here, the variables are updated from a previous time step, *t*, to a new time step, *t*+1. This is done firstly by estimating the particle positions and velocities using the shear stress and body force terms of the momentum equation in Equation (18) only (particle indices have been dropped for convenience)

$$\mathbf{v}^* = \mathbf{v}_t + \left(\frac{1}{\rho}\nabla . \boldsymbol{\tau} + \mathbf{g}\right)\Delta t \quad (20)$$

$$\mathbf{r}^* = \mathbf{r}_t + \mathbf{v}^* \Delta t \quad (21)$$

where $\mathbf{v}_t$ and $\mathbf{r}_t$ are the particle velocity and position at time *t*, respectively, and Δt the time step size. The fluid density is then updated by using the intermediate particle positions, $\mathbf{r}^*$, in Equation (14).

The new particle velocities are then evaluated by applying a correction to the initial velocity estimates

$$\mathbf{v}_{t+1} = \mathbf{v}^* + \Delta \mathbf{v}^{**} \quad (22)$$

where the velocity correction is evaluated using the pressure gradient term of the momentum equation only

$$\Delta V^{**} = -\frac{1}{\rho^*}\nabla P_{t+1}\, \Delta t \quad (23)$$

The pressure gradient at the new time, ∇P_{t+1} , is obtained by enforcing incompressibility where $\nabla . \mathbf{v} = 0$ as *per* the continuity Equation (10). Therefore, by combining Equation (22) and Equation (23) and taking the divergence, we obtain

$$\nabla . \left(\frac{\mathbf{v}_{t+1} - \mathbf{v}^*}{\Delta \mathrm{t}} \right) = -\nabla . \left(\frac{1}{\rho^*} \nabla P_{t+1} \right) \tag{24}$$

Imposing the incompressibility condition at the new time step, $\nabla . \mathbf{v}_{t+1} = 0$, leads to the Pressure Poisson Equation (PPE)

$$\nabla . \left(\frac{1}{\rho^*} \nabla P_{t+1} \right) = \frac{\nabla . \mathbf{v}^*}{\Delta \mathrm{t}} \tag{25}$$

The left hand side of this equation is discretised using Shao's approximation for the Laplacian in SPH [278], which is a hybrid of a standard SPH first derivative with a finite difference computation [229]

$$\nabla . \left(\frac{1}{\rho} \nabla P \right)_i = \sum\nolimits_j m_j \, \frac{8}{\left(\rho_i + \rho_j \right)^2} \frac{\left(P_i - P_j \right) . \mathbf{r}_{ij} . \nabla_i W_{ij}}{\left| \mathbf{r}_{ij} \right|^2 + \eta^2} \tag{26}$$

where, η is a small value (*e.g.* $0.1 \times h$) to ensure the denominator always remains non-zero. Likewise, $\nabla . \mathbf{v}^*$ in Equation (25) is discretised in SPH using the following equation

$$(\nabla . \mathbf{v}^*)_i = \rho_i \sum\nolimits_j m_j \left(\frac{\mathbf{v}_j^*}{\rho_j^2} + \frac{\mathbf{v}_i^*}{\rho_i^2} \right) . \nabla_i W_{ij} \tag{27}$$

Discretisation of the PPE equation leads to a system of linear equations, $\mathbf{Ax} = \mathbf{b}$, in which $\mathbf{x}$ is the vector of unknown pressure gradients to be determined, and the matrix $\mathbf{A}$ is not necessarily positive definite or symmetric. In the present work, the bi-Conjugate Gradient algorithm [279] was used to solve this set of equations.

The new particle positions are finally obtained using

$$\mathbf{r}_{t+1} = \mathbf{r}_t + \frac{(\mathbf{v}_t + \mathbf{v}_{t+1})}{2} \Delta t \tag{28}$$

5.2.4 **Boundary and initial conditions**

One of the challenges in the SPH method is the implementation of proper physical conditions at solid boundaries. In the work here, these boundaries were modelled using two types of virtual SPH particles as illustrated in Figure 5-2. Similar to what was done in

Libersky *et al.* [280], the virtual particles of the first type (show in orange in Figure 5-2) fill the interior of the solid by placing then as a mirror image to any fluid particles that fall within the smoothing area λh_i outside the solid. These virtual particles have the same density and pressure as the corresponding real particles, but opposite velocities. These virtual particles are insufficient to prevent the real fluid particles from penetrating into the solid on occasion. To overcome this issue, virtual particles of a second type (shown in red in Figure 5-2) are located at the fluid/solid interface as done in Monaghan [281]. These particles, which are fixed, interact with the fluid particles *via* a similar expression of Lennard-Jones of the form

$$\mathbf{F}_{rep} = \begin{cases} \varepsilon \left[\left(\frac{L_0}{r_{ij}} \right)^{12} - \left(\frac{L_0}{r_{ij}} \right)^{4} \right] \frac{\mathbf{x}_{ij}}{{r_{ij}}^2} & r_{ij} \leq L_0 \\ 0 & r_{ij} > L_0 \end{cases} \tag{29}$$

where ε is a parameter chosen to be of the same scale as the square of the largest velocity, L_0 is the initial distance between the particles that was calculated using the number of SPH particles and size of the domain, and $\mathbf{x}_{ij}$ is vector between particles i and j.

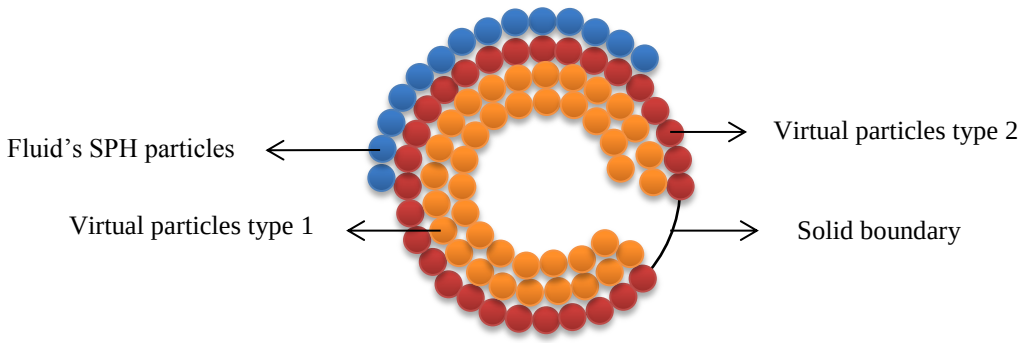

Figure 5-2 Illustration of solid particles made up of SPH particles

Periodic boundary conditions were applied in all three dimensions for the benchmark problem, whereas they were applied only in the flow direction for the μPB work. The fluid particles were initially distributed on a regular grid with spacing of $h = 1.5L_0$, where L_0 is the initial distance between particles. The number of SPH particles was also chosen based on this initial arrangement. The fluid, which was initially at rest, was driven by a body force that yielded the desired flow rate.

5.2.5 **Benchmarking**

The accuracy of the SPH model was verified by comparing an experimental drag correlation [282] against that obtained by solving for the flow around a sphere in a periodic simulation cell with the details given in Table 5-1. The drag force experienced by the sphere was computed by integrating the pressure and viscous stresses around the surface of the sphere to obtain the resultant pressure and viscous forces on the surface. Because of the symmetry of the flow, both of these resultant forces are directed downstream. It was found that one-third of the drag force could be attributed to the pressure force (pressure drag) with the remaining two-thirds being due to the viscous force (viscous drag), in line with literature for Re << 1 [283, 284]. Figure 5-3, which shows the drag coefficient obtained from SPH and the experimental correlation, shows that the SPH predictions tend to fall slightly above that of the correlation until Re ~ 0.05, with the average deviation being around 5%, whereupon it passes below the correlation with a similar deviation.

Table 5-1 Details of benchmark SPH simulation

Parameters	Value
Size of cell (L^3)	200 μm × 200 μm × 200 μm
Sphere diameter (d_p)	100 μm
Number of SPH particles (N_p)	6859
Initial distance between particles (L_0)	6.25 μm
Time step size (Δt)	2.5×10^{-5} s
Time steps to steady state (t_{ss})	6500

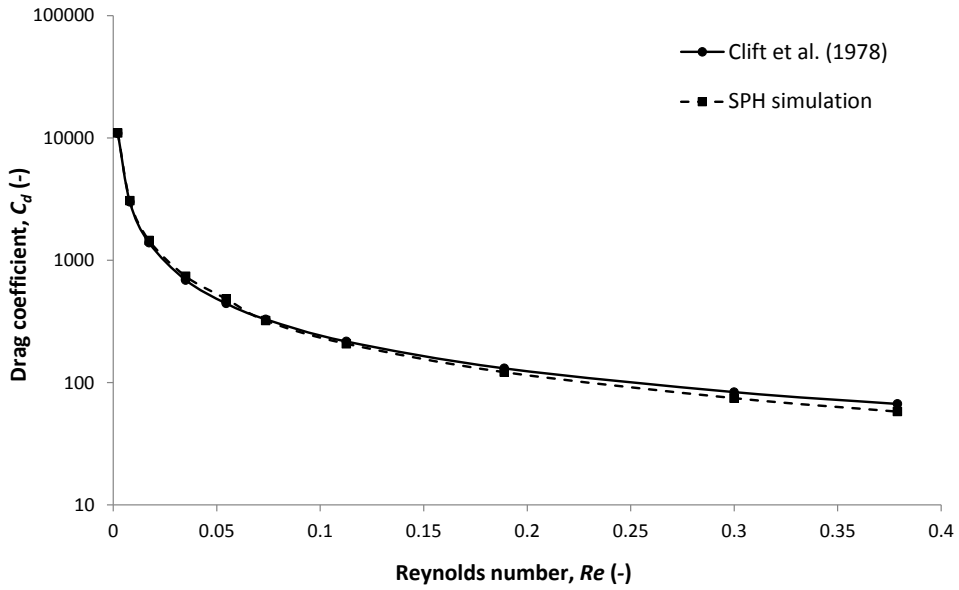

Figure 5-3 Variation of the drag coefficient of a sphere with Reynolds number as evaluated using SPH (broken line) and correlation [282] (solid line)

5.3 Micro-packed bed

For simulation of flow through a µPB, the positions of the solid particles for beds of varying bed-to-particle diameter ratios were determined from experiment using a method developed by the authors [257, 272]. SPH-based simulation of flow in the µPBs was undertaken as explained in the following; the associated simulation parameters are given in Table 5-2. In order to allow solution of the flow problem through the µPBs using a single CPU, they were divided into N_n computational cells as illustrated in Figure 5-4. The simulation was then initiated by solving the flow through first cell, N_1 under periodic boundary conditions in the flow direction until the pressure drop in the flow direction stabilised. At this point the SPH particles were then allowed to pass into the next cell, N_2, and the process repeated. This was in turn repeated for all cells until all the cells along the bed length had been considered. The pressure drop across the entire µPB was equated to the pressure at the outlet of this last cell, P_n. The number of cells considered, N_n, was dictated by the need for the pressure gradient to no longer vary with the number of cells.

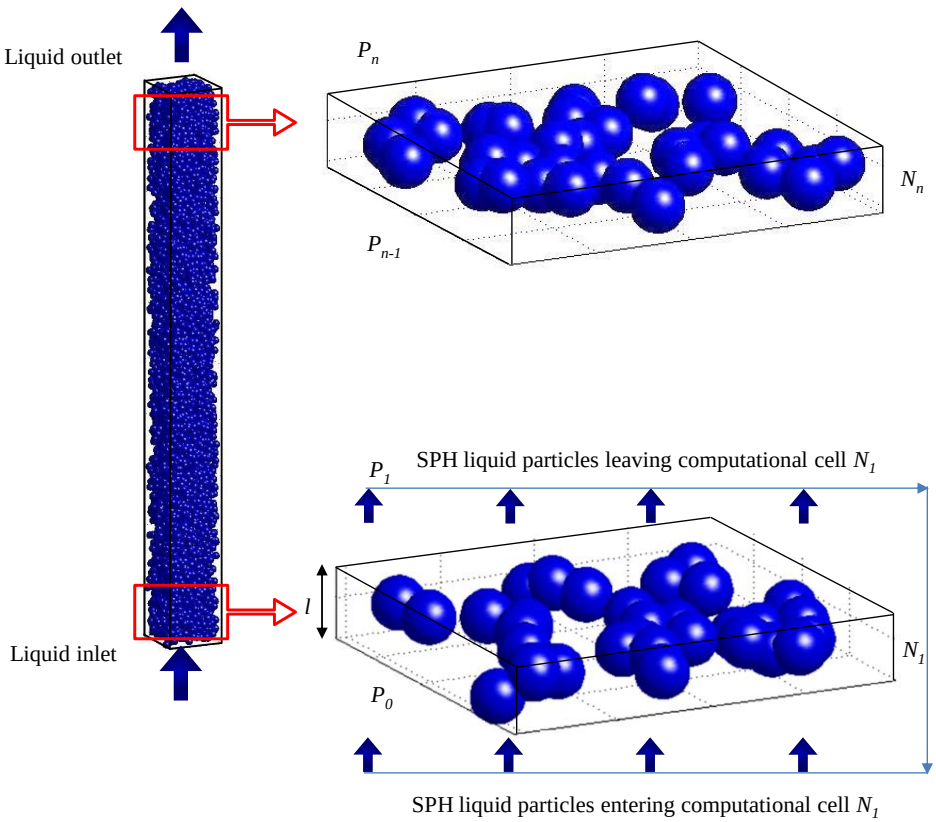

Figure 5-4 The schematic geometry of µPB, computational cells and quasi-periodic boundary condition

Table 5-2 Details of SPH-based simulation of flow in the μPBs

Parameters	Value
Size of computational cell ($D \times D \times l$)	200 μm × 200 μm × 2.2 d_p μm
Number of SPH particles (N_p)	10240
Number of cells (N_n)	$454/d_p$
Initial distance between particles (L_0)	6.25 μm
Smoothing length (h)	$1.4L_0$
Time step size (Δt)	1×10^{-5} s

5.4 Results and Discussion

Figure 5-5, which shows the pressure drop as a function of the superficial velocity for μPBs of varying bed-to-particle diameter ratios, clearly indicates that Darcy's law holds for the systems considered here. Linear fits to these data were excellent, with all lines passing through the origin with R^2 being 96% or better. This figure shows that the pressure drop increases with increasing bed-to-particle diameter ratio, consistent with the fact that the surface area *per* unit volume of the μPB increases as the particle size diminishes relative to the bed size.

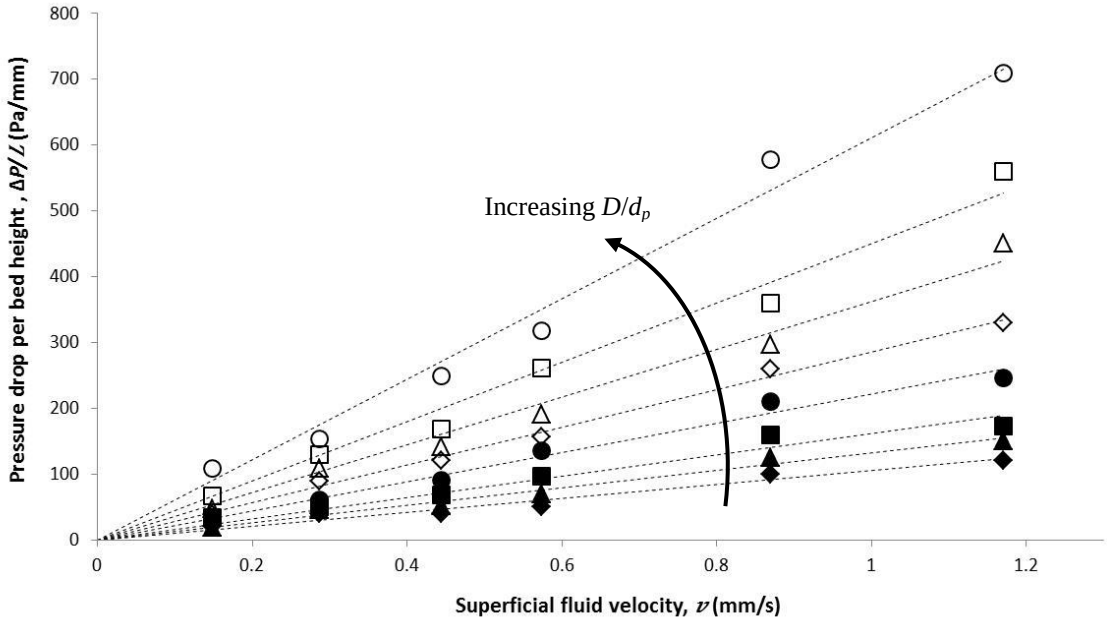

Figure 5-5 Pressure drop variations against superficial fluid velocity for different bed-to-particle diameter ratios equal to: 5.2 (solid diamonds); 5.8 (solid triangles); 6.6 (solid squares); 7.5 (solid circles); 10.4 (open diamonds); 11.6 (open triangles); 13.1 (open squares) and 15.1 (open circles), with the best fit straight lines (dash lines).

Figure 5-6 shows the dependence of the μPB permeabilities predicted here, which are derived from the slopes of the lines in Figure 5-5 as per Darcy's Law in Equation (1), with the bed-to-particle diameter ratio. This figure shows that the SPH-derived permeability decreases with the bed-to-particle diameter ratio in a non-linear manner to reach what appears to be a plateau at the upper end of range that corresponds well to the values predicted by Ergun's expression, Equation (2), which are also shown in this figure. The SPH-derived permeabilities do not, however, match those predicted by the Ergun equation at lower bed-to-particle diameter ratios except at $D/d_p = 5.8$, where the two crossover. The fact that the SPH-derived results approach that yielded by the Ergun equation at the upper end of the bed-to-particle diameter ratio strongly supports the validity of the SPH results. The deviations at lower bed-to-particle diameter ratios, on the other hand, suggests that wall effects are important for μPBs whose bed-to-particle diameter ratio is less than 10, although this limit could be located between this value and that associated with the next smallest ratio investigated, $D/d_p = 7.6$. The decreasing trend to a plateau is consistent with the bed-to-particle diameter ratio dependency of the bed porosity shown in the insert as well as the volume-fraction of the bed over which the wall has a direct influence.

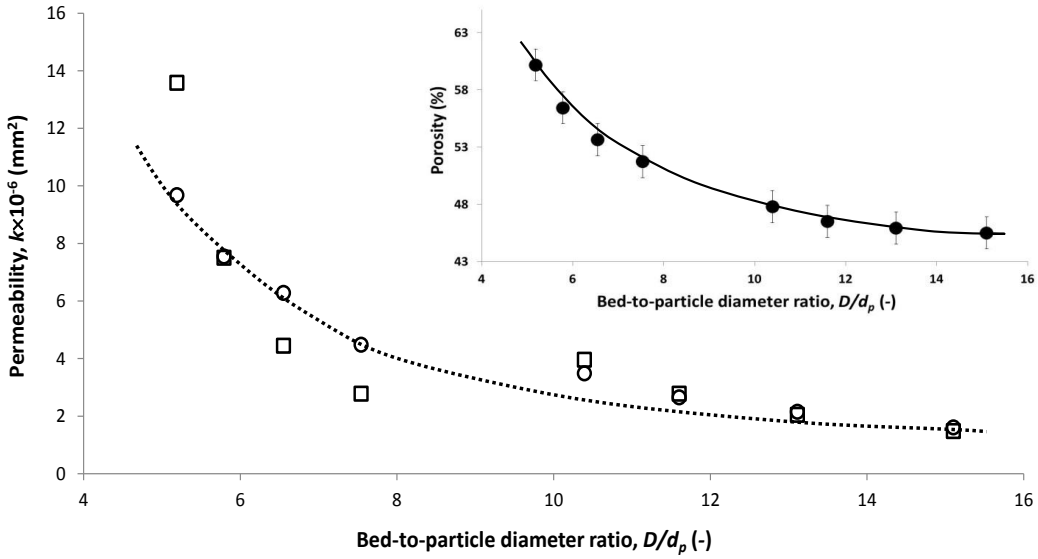

Figure 5-6 Permeability change of μPBs with bed-to-particle diameter ratio as predicted here (open circles) and from the Ergun equation, Equation 2, (open squares); the corresponding dependence of bed porosity is shown as an insert [272]. The uncertainties in the permeability data is less than the size of the symbols. The broken and solid lines are a guide to the eye only for the permeability predicted here and the porosity, respectively.

Figure 5-7 compares the SPH-derived permeabilities of the µPBs with counterparts obtained from the correlations outlined in the Introduction of this paper; deviation of the points from the broken line indicate a discrepancy between the two permeability estimates. The corresponding bed-to-particle diameter ratios are shown in descending order on an axis on the right hand side of the figure to aid understanding. The SPH results compare most favourably to the values derived from the expression of Reichelt [127], where the average and median differences are 50% and 26%, respectively. The estimates yielded by the model of Foumeny [53] are on average around 90% out from the SPH-derived results (average of 87%, median 91%). The remaining models derived for macroscale packed beds that include the bed-to-particle diameter ratio all deviate substantially, 160% to 344% median differences, from the SPH-derived results. As the SPH-derived results appear to match well the Ergun estimate at larger bed-to-particle diameter ratios, the larger deviations seen here for the Eisfeld & Schnitzlein [118], Raichura [50], Cheng [48], and Di Felice & Gibilaro [51] suggest these models are not appropriate for µPBs.

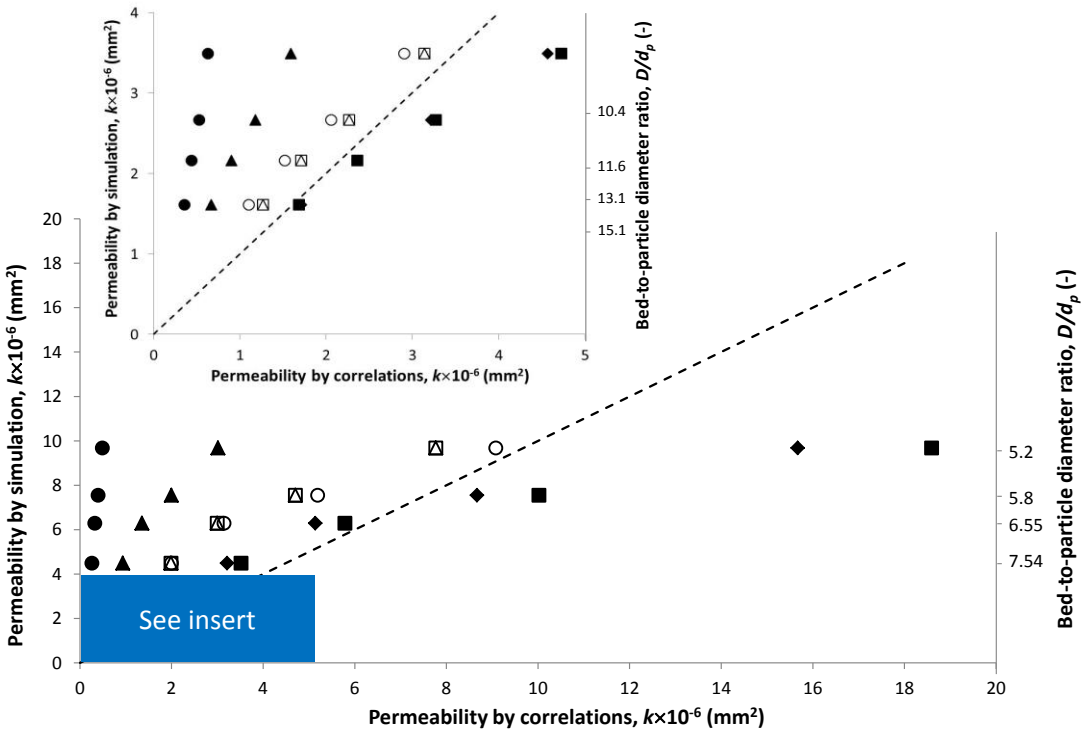

Figure 5-7 Comparison of the µPB permeability obtained by simulation with those determined *via* existing correlations determined from macroscale beds: Eisfeld & Schnitzlein (solid triangles); Reichelt (open triangle); Raichura (solid circles); Cheng (open circles); Di Felice & Gibilaro (solid squares) and Mehta & Hawley (open squares) and Foumeny (solid diamonds).

The variation of the porosity and axial fluid velocity with position across the radius of the μPBs is shown in Figure 5-8 for the bed-to-particle diameter ratio of 15.1; the results are similar for all the other μPBs considered here. It can be seen in Figure 5-8 that the porosity in the μPB decreases from unity at the wall to the bulk value in a damped oscillatory way some three particle diameters in from the wall. This inhomogeneity in the bed porosity leads to significant radial variation in the axial fluid speed, with the speed being locally maximal where the porosity is also similarly maximal, means the fluid not only channels along the wall, but also at annuli within the bed. This clearly has performance implications for μPBs compared to their macroscale counterparts, suggesting that models for their performance (*e.g.* heat and mass transfer characteristics) may not be appropriate for μPBs [53, 273].

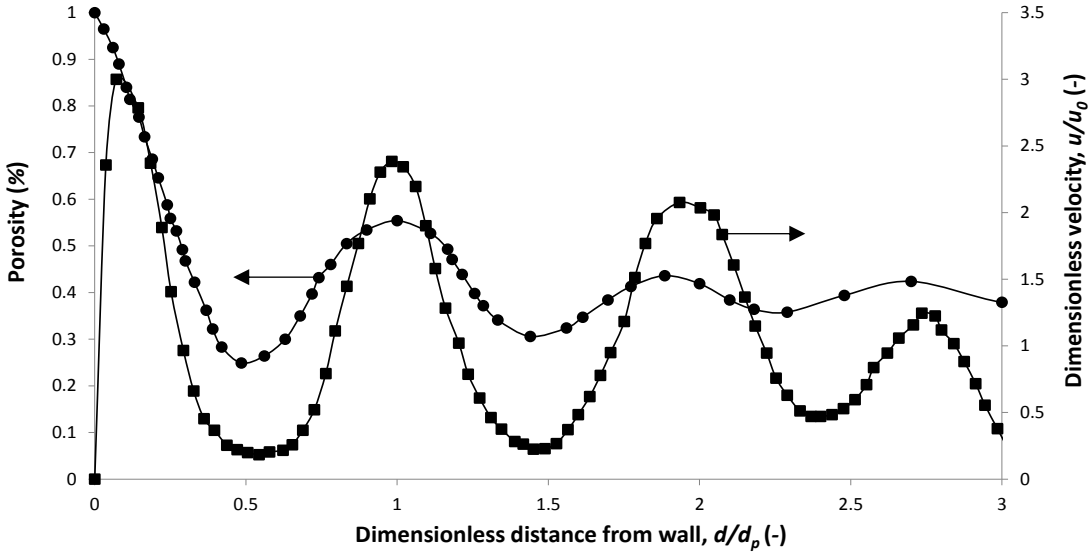

Figure 5-8 The variation of μPB porosity (solid circles) and dimensionless velocity (solid squares) for d_p = 26.5 μm and D/d_p = 15.1

5.5 Conclusion

The hydrodynamic character of micro-packed beds (μPBs) have been investigated as a function of bed-to-particle diameter ratio, D/d_p, using smoothed-particle hydrodynamic (SPH) simulation on models of the beds derived from X-ray microtomography. The permeabilities obtained from this work were in line with that given by the Ergun model for $D/d_p > 10$, suggesting the SPH results are valid. The permeability decreased with the

bed-to-particle diameter ratio in a non-linear manner from around 10^{-5} mm^2 for the smallest ratio ($D/d_p = 5.2$), in line with a similar trend for the porosity change and volume of the 'wall region' relative to the total bed volume.

Comparison of the SPH-derived results with a variety of models developed for accounting for bed-to-particle diameter ratio in macroscale packed beds suggests that the model of Reichelt [127] may be suitable for estimating the permeability of μPBs, although the model of Foumeny [53] also yielded estimates that deviated less than 100% from the SPH results on average. The estimates yielded by the models of Eisfeld & Schnitzlein [118], Raichura [50], Cheng [48], and Di Felice & Gibilaro [51] all deviated significantly from the SPH-derived results. The largely empirical nature of these longer-standing macroscale-based models means it is difficult to discern the origins of these poor comparisons.

Finally, it is also shown that the local axial flow velocity in the μPBs is inhomogeneous, with channelling being observed to occur not only at the bed wall, but also within the bed due to oscillatory porosity variation with radius. This suggests that performance models derived for macroscale beds may not be suitable for μPBs. The work here suggests that the approach taken here could not only form a sound basis for predicting the hydrodynamic character of μPBs, but also their heat and mass transfer and reaction characteristics.

Chapter 6: **Conclusion**

This thesis is focused on detailing work that was focused on developing the application of a mesh-free explicit numerical simulation method to the study of fluid flows in the micro-packed beds (μPBs) so as to determine their hydrodynamic character in general, with particular focus on the effect of the wall region. This work was undertaken through two related developments. The accurate reconstruction of the structure of a μPBs from X-ray microtomography data o represents the first development. Modelling of fluid flow through these structures was the second development.

The first development has been divided into two parts: the first involved generation of approximate μPB models, and the second involved their refinement. Although X-ray microtomography systems can yield three-dimensional (3D) greyscale images of the structure and porosity of μPBs, they are generally of poor quality because the resolution of the X-ray systems are generally low relative to the characteristic dimensions of the particles and porosity in the bed. This manifests as a loss of the underlying particle geometry (*e.g.* spherical if the bed is composed of spheres) in the model, and the conversion of the grayscale images into binary counterparts being sensitive to the greyscale threshold used to partition the pixels between the solid and void phases. The new method described herein obviates these issues when the μPBs are composed of largely monodisperse particles of high sphericity. It achieves this by identifying in successive cross-sectional images of the bed the approximate centre and diameter of the particle cross-sections, replacing them with circles, and then assembling them to form the particles by identifying correlations between the successive images. The new method does not require specification of a threshold for binarizing the images and preserves the spherical geometry of the packing. The method has been demonstrated by applying it to a μPB. The recovered structure appears reasonable and has a porosity that is, within experimental uncertainty, equal to the value measured directly. In comparison, use of the well-known Otsu automatic thresholding method to partition the greyscale images into solid and void regions yielded a model in which the underlying spherical geometry and various other structural details were lost, and a porosity that was nearly 10% adrift, well beyond the experimental uncertainty.

Whilst the method outlined immediately above represents a significant improvement on the status quo, the models still contained defects in the form of particles overlapping each other and the walls, and suspended particles. These defects were in part due to the assumption that the particles were all of the same size equal to the experimental average, and that there is some uncertainty associated with determining the particle positions. In the second part of the first development, these defects were eliminated by applying a reverse Monte Carlo (RMC) algorithm combined with simulated annealing (SA) to shift from the single particle size to the experimentally identified particle size distribution, and refine the particle positions within constraints defined by the uncertainty in their initial determination. A μPB model obtained *via* application of RMC-SA to an initial model yielded a porosity that was consistent with its directly determined counterpart. This approach also yielded a variation of porosity with channel-to-particle size ratio that was consistent with this experimental data and, allowing for different bed cross-sections (square *vs.* circular) data published elsewhere.

The new method was used to build models of the structure of eight μPBs of increasing bed-to-particle diameter ratio. Analysis of these models revealed that the porosity was near unity at the walls and varied in an oscillatory manner normal to it for up to three particle diameters into the bed. The mean coordination number is also found to vary over the same distance from the bed wall where it was a minimum. The values of the mean coordination number in the bulk of the bed fell between that associated with 'loose random packings', which occurred for the bed of the smallest bed-to-particle diameter ratio, to 'close packings' in the largest beds relative to the particles. These observations suggest there are two origins for the variation in the mean coordination number with bed-to-particle size ratio: a volumetric one in which the bulk value exerts increasing influence as the ratio increases, and the degree of packing, where this too increases with the size ratio.

The second development of the work reported here was concerned with a meshless computational fluid dynamics technique to study Newtonian fluid flow through μPBs. The smoothed particle hydrodynamics (SPH) technique was used to study fluid flow through the μPB models derived from the method outlined above. This study included determination of the permeability and by-pass fraction due to wall effects in the μPBs, which go to the issues of bed performance and pumping power requirements. These

developments provide a basis for determining the hydrodynamic character of µPBs that are difficult to determine experimentally because of the challenges faced in measuring the small pressure drops involved and the absence of the limited spatial and temporal resolutions of various imaging techniques.

In terms of future work, there is clearly an opportunity to expand on the work concerned with building models of µPBs to allow the reconstruction of systems that are less mono-disperse or which involve particles of different regular shapes (*e.g.* ellipsoids). Firstly, it would also be of interest to extend the method to bed geometries beyond the simplest such as the straight channels considered here; for example, those involving irregular channel shapes. Secondly, applying RMC algorithm combined with the other optimization algorithms would be of interest to see effectiveness of the structure refinement method, suggested for µPBs in this work. Finally in the case of the explicit numerical simulation work, this can be extended to these more complex beds in addition to fluids beyond that considered here, including non-Newtonian and multiphase, and non-isothermal conditions; all are of relevance to microfluidic applications. Before this happens, however, parallelisation of the code and adoption of more efficient methods for solving the Pressure Poisson Equation will be necessary.

References

[1] Squires TM, Quake SR. Microfluidics: Fluid physics at the nanoliter scale. Rev Mod Phy. 2005;77(3):977.

[2] Stone HA, Stroock AD, Ajdari A. Engineering flows in small devices: Microfluidics towards lab-on-a-chip. Annual Review of Fluid Mechanics. 2004;36(1):381-411.

[3] Whitesides GM. The origins and the future of microfluidics. Nature. 2006;442(7101):368-73.

[4] Shui L. Two-phase flow in micro and nanofluidic devices: University of Twente 2009.

[5] Hessel V, Renken A, Schouten JC, Yoshida J-i. Micro process engineering: a comprehensive handbook: John Wiley & Sons 2009.

[6] Jensen KF. Silicon-based microreactors. Microreactor Technology and Process Intensification ACS Symposium Series; 2005.

[7] Harmsen GJ. Reactive distillation: The front-runner of industrial process intensification: A full review of commercial applications, research, scale-up, design and operation. Chemical Engineering and Processing: Process Intensification. 2007;46(9):774-80.

[8] Burns JR, Jamil JN, Ramshaw C. Process intensification: operating characteristics of rotating packed beds — determination of liquid hold-up for a high-voidage structured packing. Chemical Engineering Science. 2000;55(13):2401-15.

[9] Van Gerven T, Stankiewicz A. Structure, energy, synergy, time The fundamentals of process intensification. Industrial & Engineering Chemistry Research. 2009;48(5):2465-74.

[10] Kockmann N. Transport phenomena in micro process engineering: Springer Science & Business Media 2007.

[11] Jähnisch K, Hessel V, Löwe H, Baerns M. Chemistry in microstructured reactors. Angewandte Chemie International Edition. 2004;43(4):406-46.

[12] Zanfir M, Gavriilidis A, Wille C, Hessel V. Carbon Dioxide Absorption in a Falling Film Microstructured Reactor: Experiments and Modeling. Industrial & Engineering Chemistry Research. 2005;44(6):1742-51.

[13] Wörz O, Jäckel KP, Richter T, Wolf A. Microreactors, a new efficient tool for optimum reactor design. Chemical Engineering Science. 2001;56(3):1029-33.

[14] Losey MW, Schmidt MA, Jensen KF. Microfabricated Multiphase Packed-Bed Reactors: Characterization of Mass Transfer and Reactions. Industrial & Engineering Chemistry Research. 2001;40(12):2555-62.

[15] Su Y, Zhao Y, Chen G, Yuan Q. Liquid–liquid two-phase flow and mass transfer characteristics in packed microchannels. Chemical Engineering Science. 2010;65(13):3947-56.

[16] Ehrfeld W, Hessel V, Löwe H. Microreactors: New Technology for Modern Chemistry: Wiley 2000.

[17] Schulte TH, Bardell RL, Weigl BH. Microfluidic technologies in clinical diagnostics. Clinica Chimica Acta. 2002;321(1):1-10.

[18] Melin J, Quake SR. Microfluidic Large-Scale Integration: The Evolution of Design Rules for Biological Automation. Annual Review of Biophysics and Biomolecular Structure. 2007;36(1):213-31.
[19] Haeberle S, Mark D, von Stetten F, Zengerle R. Microfluidic Platforms for Lab-On-A-Chip Applications. In: Zhou Z, Wang Z, Lin L, eds. *Microsystems and Nanotechnology*: Springer Berlin Heidelberg 2012:853-95.
[20] Abgrall P, Gué AM. Lab-on-chip technologies: making a microfluidic network and coupling it into a complete microsystem—a review. Journal of Micromechanics and Microengineering. 2007;17(5):R15.
[21] Manz A, Graber N, Widmer HM. Miniaturized total chemical analysis systems: A novel concept for chemical sensing. Sensors and Actuators B: Chemical. 1990;1(1–6):244-8.
[22] Reyes DR, Iossifidis D, Auroux P-A, Manz A. Micro total analysis systems. 1. Introduction, theory, and technology. Analytical chemistry. 2002;74(12):2623-36.
[23] Auroux P-A, Iossifidis D, Reyes DR, Manz A. Micro total analysis systems. 2. Analytical standard operations and applications. Analytical chemistry. 2002;74(12):2637-52.
[24] Erickson D, Li D. Integrated microfluidic devices. Analytica Chimica Acta. 2004;507(1):11-26.
[25] Hu G, Li D. Multiscale phenomena in microfluidics and nanofluidics. Chemical Engineering Science. 2007;62(13):3443-54.
[26] van den Berg A, Lammerink T. Micro total analysis systems: microfluidic aspects, integration concept and applications. *Microsystem technology in chemistry and life science*: Springer 1998:21-49.
[27] Losey MW, Jackman RJ, Firebaugh SL, Schmidt MA, Jensen KF. Design and fabrication of microfluidic devices for multiphase mixing and reaction. Microelectromechanical Systems, Journal of. 2002;11(6):709-17.
[28] Ajmera S, Delattre C, Schmidt M, Jensen K. A Novel Cross-Flow Microreactor for Kinetic Studies of Catalytic Processes. In: Matlosz M, Ehrfeld W, Baselt J, eds. *Microreaction Technology*: Springer Berlin Heidelberg 2001:414-23.
[29] Happel J. Viscous flow in multiparticle systems: slow motion of fluids relative to beds of spherical particles. AIChE Journal. 1958;4(2):197-201.
[30] Ergun S, Orning AA. Fluid flow through randomly packed columns and fluidized beds. Industrial & Engineering Chemistry. 1949;41(6):1179-84.
[31] Leder F, Butt JB. The dynamic behavior of a fixed-bed catalytic reactor. AIChE Journal. 1966;12(6):1057-63.
[32] Koch DL, Brady JF. Dispersion in fixed beds. Journal of Fluid Mechanics. 1985;154:399-427.
[33] Del Col D, Bisetto A, Bortolato M, Torresin D, Rossetto L. Experiments and updated model for two phase frictional pressure drop inside minichannels. International Journal of Heat and Mass Transfer. 2013;67(0):326-37.
[34] Márquez N, Castaño P, Moulijn JA, Makkee M, Kreutzer MT. Transient Behavior and Stability in Miniaturized Multiphase Packed Bed Reactors. Industrial & Engineering Chemistry Research. 2009 2010;49(3):1033-40.
[35] Márquez N, Castaño P, Makkee M, Moulijn JA, Kreutzer MT. Dispersion and Holdup in Multiphase Packed Bed Microreactors. Chemical Engineering & Technology. 2008;31(8):1130-9.

[36] Márquez N, Musterd M, Castaño P, Berger R, Moulijn JA, Makkee M, et al. Volatile tracer dispersion in multi-phase packed beds. Chemical Engineering Science. 2010;65(13):3972-85.
[37] van Herk D, Kreutzer MT, Makkee M, Moulijn JA. Scaling down trickle bed reactors. Catalysis today. 2005;106(1):227-32.
[38] Márquez N, Castaño P, Moulijn JA, Makkee M, Kreutzer MT. Transient Behavior and Stability in Miniaturized Multiphase Packed Bed Reactors. Industrial & Engineering Chemistry Research. 2010;49(3):1033-40.
[39] Su H, Niu H, Pan L, Wang S, Wang A, Hu Y. The Characteristics of Pressure Drop in Microchannels. Industrial & Engineering Chemistry Research. 2010;49(8):3830-9.
[40] Steinke ME, Kandlikar SG. Single-phase liquid friction factors in microchannels. International Journal of Thermal Sciences. 2006;45(11):1073-83.
[41] Faridkhou A, Hamidipour M, Larachi F. Hydrodynamics of gas–liquid micro-fixed beds – Measurement approaches and technical challenges. Chemical Engineering Journal. 2013;223(0):425-35.
[42] Bear J. Dynamics of Fluids in Porous Media: Dover 1988.
[43] Dullien FAL, Brenner H. Porous Media: Fluid Transport and Pore Structure: Elsevier Science 2012.
[44] Leva M. Pressure drop through packed tubes-Part I. A general correlation. Chemical Engineering Progress. 1947;43 549–54.
[45] Ergun S. Fluid Flow through Packed Columns. Chemical Engineering Progress. 1952;48:89-94.
[46] Winterberg M, Tsotsas E. Impact of tube-to-particle-diameter ratio on pressure drop in packed beds. AIChE Journal. 2000;46(5):1084-8.
[47] Mehta D, Hawley MC. Wall Effect in Packed Columns. Industrial & Engineering Chemistry Process Design and Development. 1969;8(2):280-2.
[48] Cheng N-S. Wall effect on pressure drop in packed beds. Powder Technology. 2011;210(3):261-6.
[49] Choi YS, Kim SJ, Kim D. A semi-empirical correlation for pressure drop in packed beds of spherical particles. Transport in porous media. 2008;75(2):133-49.
[50] Raichura R. Pressure drop and heat transfer in packed beds with small tube-to-particle diameter ratio. Experimental heat transfer. 1999;12(4):309-27.
[51] Di Felice R, Gibilaro L. Wall effects for the pressure drop in fixed beds. Chemical engineering science. 2004;59(14):3037-40.
[52] Reichelt W. Zur Berechnung des Druckverlustes einphasig durchströmter Kugel- und Zylinderschüttungen. Chemie Ingenieur Technik. 1972;44(18):1068-71.
[53] Foumeny EA, Benyahia F, Castro JAA, Moallemi HA, Roshani S. Correlations of pressure drop in packed beds taking into account the effect of confining wall. International Journal of Heat and Mass Transfer. 1993;36(2):536-40.
[54] Humby SJ, Biggs MJ, Tüzün U. Explicit numerical simulation of fluids in reconstructed porous media. Chemical Engineering Science. 2002;57(11):1955-68.
[55] Le Roux Sb, Petkov V. Interactive Structrue Analysis of Amorphous and Crystalline Systems. 2010 [cited; Available from: http://people.cst.cmich.edu/petko1vg/isaacs/phys/pbc.html
[56] Hellström J, Lundström T. Flow through porous media at moderate Reynolds number. International Scientific Colloquium: Modelling for Material Processing; 2006; 2006. p. 129-34.

[57] Gunjal PR, Ranade VV, Chaudhari RV. Computational study of a single-phase flow in packed beds of spheres. AIChE Journal. 2005;51(2):365-78.
[58] Calis H, Nijenhuis J, Paikert B, Dautzenberg F, Van Den Bleek C. CFD modelling and experimental validation of pressure drop and flow profile in a novel structured catalytic reactor packing. Chemical Engineering Science. 2001;56(4):1713-20.
[59] Han K, Feng YT, Owen DRJ. Sphere packing with a geometric based compression algorithm. Powder Technology. 2005;155(1):33-41.
[60] Jerier J-F, Richefeu V, Imbault D, Donzé F-V. Packing spherical discrete elements for large scale simulations. Computer Methods in Applied Mechanics and Engineering. 2010;199(25–28):1668-76.
[61] Mueller GE. Numerically packing spheres in cylinders. Powder Technology. 2005;159(2):105-10.
[62] Nolan G, Kavanagh P. Computer simulation of random packing of hard spheres. Powder technology. 1992;72(2):149-55.
[63] Hockney RW, Eastwood JW. Computer simulation using particles: Taylor & Francis 1989.
[64] Soppe W. Computer simulation of random packings of hard spheres. Powder Technology. 1990;62(2):189-97.
[65] Jullien R, Pavlovitch A, Meakin P. Random packings of spheres built with sequential models. Journal of Physics A: Mathematical and General. 1992;25(15):4103.
[66] ABREU CRA, MACIAS-SALINAS R, TAVARES FW, CASTIER M. A Monte Carlo simulation of the packing and segregation of spheres in cylinders. Brazilian Journal of Chemical Engineering. 1999;16:395-405.
[67] Maier RS, Kroll DM, Bernard RS, Howington SE, Peters JF, Davis HT. Hydrodynamic dispersion in confined packed beds. Physics of Fluids (1994-present). 2003;15(12):3795-815.
[68] Salles J, Thovert J, Adler P. Deposition in porous media and clogging. Chemical Engineering Science. 1993;48(16):2839-58.
[69] Biggs MJ, Humby SJ, Buts A, Tüzün U. Explicit numerical simulation of suspension flow with deposition in porous media: influence of local flow field variation on deposition processes predicted by trajectory methods. Chemical Engineering Science. 2003;58(7):1271-88.
[70] Valera R, Morales I, Vanmaercke S, Morfa C, Cortés L, Casañas H-G. Modified algorithm for generating high volume fraction sphere packings. Comp Part Mech. 2015:1-12.
[71] Quiblier JA. A new three-dimensional modeling technique for studying porous media. Journal of Colloid and Interface Science. 1984;98(1):84-102.
[72] Bentz DP, Martys NS. Hydraulic radius and transport in reconstructed model three-dimensional porous media. Transport in porous media. 1994;17(3):221-38.
[73] Giona M, Adrover A. Closed-form solution for the reconstruction problem in porous media. AIChE journal. 1996;42(5):1407-15.
[74] Losic N, Thovert J-F, Adler P. Reconstruction of porous media with multiple solid phases. Journal of colloid and interface science. 1997;186(2):420-33.
[75] Roberts AP. Statistical reconstruction of three-dimensional porous media from two-dimensional images. Physical Review E. 1997;56(3):3203.

[76] Levitz P. Off-lattice reconstruction of porous media: critical evaluation, geometrical confinement and molecular transport. Advances in Colloid and Interface Science. 1998;76:71-106.
[77] Liang C, Dai S, Guiochon G. A Graphitized-Carbon Monolithic Column. Analytical Chemistry. 2003;75(18):4904-12.
[78] Dulay MT, Kulkarni RP, Zare RN. Preparation and Characterization of Monolithic Porous Capillary Columns Loaded with Chromatographic Particles. Analytical Chemistry. 1998;70(23):5103-7.
[79] Motokawa M, Kobayashi H, Ishizuka N, Minakuchi H, Nakanishi K, Jinnai H, et al. Monolithic silica columns with various skeleton sizes and through-pore sizes for capillary liquid chromatography. Journal of Chromatography A. 2002;961(1):53-63.
[80] Williams RA, Jia X. Tomographic imaging of particulate systems. Advanced Powder Technology. 2003;14(1):1-16.
[81] Nijemeisland M, Dixon AG. CFD study of fluid flow and wall heat transfer in a fixed bed of spheres. AIChE Journal. 2004;50(5):906-21.
[82] Reddy RK, Joshi JB. CFD modeling of pressure drop and drag coefficient in fixed and expanded beds. Chemical engineering research and design. 2008;86(5):444-53.
[83] Liu GR, Liu MB. Smoothed particle hydrodynamics: a meshfree particle method: World Scientific 2003.
[84] Manz A, Graber N, Widmer HM. Miniaturized total chemical analysis systems: A novel concept for chemical sensing. Sensors and Actuators B. 1990;1(1-6):244-8.
[85] Rivet C, Lee H, Hirsch A, Hamilton S, Lu H. Microfluidics for medical diagnostics and biosensors. Chemical Engineering Science. 2011;66(7):1490-507.
[86] Ryan TJ. Microcirculation in psoriasis: blood vessels, lymphatics and tissue fluid. Pharmacology & therapeutics. 1980;10(1):27-64.
[87] Sackmann EK, Fulton AL, Beebe DJ. The present and future role of microfluidics in biomedical research. Nature. 2014;507(7491):181-9.
[88] Sharrott D, Sayeed HA. Intellectual Property Developments in Biochip Nanotechnology. Nanotechnology Law&Business. 2006;3(1):21-5.
[89] Russel WB, Saville DA, Schowalter WR. Colloidal Dispersions: Cambridge University Press 1992.
[90] Canny M. Flow and transport in plants. Annual Review of Fluid Mechanics. 1977;9(1):275-96.
[91] Ge H, Chen G, Yuan Q, Li H. Gas phase catalytic partial oxidation of toluene in a microchannel reactor. Catalysis Today. 2005;110(1–2):171-8.
[92] Hessel V, Löwe H. Microchemical engineering: components, plant concepts user acceptance–Part I. Chemical engineering & technology. 2003;26(1):13-24.
[93] Odedra A, Geyer K, Gustafsson T, Gilmour R, Seeberger PH. Safe, facile radical-based reduction and hydrosilylation reactions in a microreactor using tris (trimethylsilyl) silane. Chemical Communications. 2008(26):3025-7.
[94] Jensen KF. Microreaction engineering — is small better? Chemical Engineering Science. 2001;56(2):293-303.
[95] Squires TM, Quake SR. Microfluidics: Fluid physics at the nanoliter scale. Reviews of Modern Physics. 2005;77(3):977-1026.
[96] Taghavi-Moghadam S, Kleemann A, Golbig G. Microreaction Technology as a Novel Approach to Drug Design, Process Development and Reliability. Organic Process Research & Development. 2001;5(6):652-8.

[97] Hessel V, Löwe H, Schönfeld F. Micromixers—a review on passive and active mixing principles. Chemical Engineering Science. 2005;60(8–9):2479-501.
[98] Celata GP, Cumo M, McPhail S, Zummo G. Characterization of fluid dynamic behaviour and channel wall effects in microtube. International Journal of Heat and Fluid Flow. 2006;27(1):135-43.
[99] Peng XF, Wang BX, Peterson GP, Ma HB. Experimental investigation of heat transfer in flat plates with rectangular microchannels. International Journal of Heat and Mass Transfer. 1995;38(1):127-37.
[100] Hetsroni G, Mosyak A, Pogrebnyak E, Yarin LP. Fluid flow in micro-channels. International Journal of Heat and Mass Transfer. 2005;48(10):1982-98.
[101] Guettel R, Turek T. Assessment of micro-structured fixed-bed reactors for highly exothermic gas-phase reactions. Chemical Engineering Science. 2010;65(5):1644-54.
[102] Tidona B, Desportes S, Altheimer M, Ninck K, von Rohr PR. Liquid-to-particle mass transfer in a micro packed bed reactor. International Journal of Heat and Mass Transfer. 2012;55(4):522-30.
[103] Ajmera SK, Delattre C, Schmidt MA, Jensen KF. Microfabricated cross-flow chemical reactor for catalyst testing. Sensors and Actuators B: Chemical. 2002;82(2–3):297-306.
[104] Trachsel F, Hutter C, von Rohr PR. Transparent silicon/glass microreactor for high-pressure and high-temperature reactions. Chemical Engineering Journal. 2008;135, Supplement 1(0):S309-S16.
[105] Ajmera SK, Delattre C, Schmidt MA, Jensen KF. Microfabricated Differential Reactor for Heterogeneous Gas Phase Catalyst Testing. Journal of Catalysis. 2002;209(2):401-12.
[106] Hotz N, Osterwalder N, Stark WJ, Bieri NR, Poulikakos D. Disk-shaped packed bed micro-reactor for butane-to-syngas processing. Chemical Engineering Science. 2008;63(21):5193-201.
[107] de Mas N, Günther A, Schmidt MA, Jensen KF. Microfabricated Multiphase Reactors for the Selective Direct Fluorination of Aromatics. Industrial & Engineering Chemistry Research. 2003;42(4):698-710.
[108] Wang K, Lu YC, Xia Y, Shao HW, Luo GS. Kinetics research on fast exothermic reaction between cyclohexanecarboxylic acid and oleum in microreactor. Chemical Engineering Journal. 2011;169(1–3):290-8.
[109] Oleschuk RD, Shultz-Lockyear LL, Ning Y, Harrison DJ. Trapping of bead-based reagents within microfluidic systems: on-chip solid-phase extraction and electrochromatography. Analytical chemistry. 2000;72(3):585-90.
[110] Kiwi-Minsker L, Renken A. Microstructured reactors for catalytic reactions. Catalysis Today. 2005;110(1–2):2-14.
[111] Cao C, Palo DR, Tonkovich ALY, Wang Y. Catalyst screening and kinetic studies using microchannel reactors. Catalysis Today. 2007;125(1–2):29-33.
[112] Hartman RL, Jensen KF. Microchemical systems for continuous-flow synthesis. Lab on a Chip. 2009;9(17):2495-507.
[113] Hessel V, Löwe H, Schönfeld F. Micromixers - a review on passive and active mixing principles. Chemical Engineering Science. 2005;60(8-9):2479-501.
[114] Rose HE. An Investigation into the Laws of Flow of Fluids through Beds of Granular Materials*. Proceedings of the Institution of Mechanical Engineers. 1945 June 1, 1945;153(1):141-8.

[115] Baker MJ. CFD simulation of flow through packed beds using the finite volume technique: University of Exeter; 2011.
[116] Balhoff MT, Thompson KE. A macroscopic model for shear-thinning flow in packed beds based on network modeling. Chemical Engineering Science. 2006;61(2):698-719.
[117] Khirevich S, Höltzel A, Hlushkou D, Tallarek U. Impact of Conduit Geometry and Bed Porosity on Flow and Dispersion in Noncylindrical Sphere Packings. Analytical Chemistry. 2007;79(24):9340-9.
[118] Eisfeld B, Schnitzlein K. The influence of confining walls on the pressure drop in packed beds. Chemical Engineering Science. 2001;56(14):4321-9.
[119] Strigle RF. Packed tower design and applications: random and structured packings: Gulf Pub. Co. 1994.
[120] Carman P. Fluid flow through granular beds. Transactions-Institution of Chemical Engineeres. 1937;15:150-66.
[121] Bird RB, Stewart WE, Lightfoot EN. Transport phenomena: John Wiley & Sons 2007.
[122] Happel J, Brenner H. Low Reynolds number hydrodynamics. The Hague, Netherlands: M. Nijhoff Publishers 1983.
[123] Azzam MIS, Dullien FAL. Calculation of the Permeability of Porous Media from the Navier-Stokes Equation. Industrial & Engineering Chemistry Fundamentals. 1976 1976/11/01;15(4):281-5.
[124] Staněk V. Fixed bed operations: flow distribution and efficiency: Ellis Horwood 1994.
[125] Carman PC. Fluid flow through granular beds. Chemical Engineering Research and Design. 1997;75, Supplement(0):S32-S48.
[126] Martin H. Low Peclet number particle-to-fluid heat and mass transfer in packed beds. Chemical Engineering Science. 1978;33(7):913-9.
[127] Reichelt W. Zur Berechnung des Druckverlustes einphasig durchströmter Kugel- und Zylinderschüttungen. Chemie Ingenieur Technik. 1972;44(18):1068-71.
[128] Tsotsas E. The influence of confining walls on the pressure drop in packed beds. Chemical Engineering Science. 2002;57(10):1827.
[129] Macdonald I, El-Sayed M, Mow K, Dullien F. Flow through porous media-the Ergun equation revisited. Industrial & Engineering Chemistry Fundamentals. 1979;18(3):199-208.
[130] Foscolo P, Gibilaro L, Waldram S. A unified model for particulate expansion of fluidised beds and flow in fixed porous media. Chemical Engineering Science. 1983;38(8):1251-60.
[131] Handley D, Heggs P. Momentum and heat transfer mechanisms in regular shaped packings. Transactions of the Institution of Chemical Engineers and the Chemical Engineer. 1968;46(9):T251-&.
[132] Mehta D, Hawley M. Wall effect in packed columns. Industrial & Engineering Chemistry Process Design and Development. 1969;8(2):280-2.
[133] Liu X, Xu G, Gao S. Micro fluidized beds: Wall effect and operability. Chemical Engineering Journal. 2008;137(2):302-7.
[134] Piller M, Schena G, Nolich M, Favretto S, Radaelli F, Rossi E. Analysis of Hydraulic Permeability in Porous Media: From High Resolution X-ray Tomography to Direct Numerical Simulation. Transport in Porous Media. 2009;80(1):57-78.

[135] Vidal D, Ridgway C, Pianet G, Schoelkopf J, Roy R, Bertrand F. Effect of particle size distribution and packing compression on fluid permeability as predicted by lattice-Boltzmann simulations. Computers & Chemical Engineering. 2009;33(1):256-66.
[136] Tobiś J. Influence of bed geometry on its frictional resistance under turbulent flow conditions. Chemical Engineering Science. 2000;55(22):5359-66.
[137] Kuwabara S. The Forces experienced by Randomly Distributed Parallel Circular Cylinders or Spheres in a Viscous Flow at Small Reynolds Numbers. Journal of the Physical Society of Japan. 1959;14(4):527-32.
[138] Tien C, Ramarao BV. Granular filtration of aerosols and hydrosols: Elsevier 2011.
[139] Brinkman H. A calculation of the viscous force exerted by a flowing fluid on a dense swarm of particles. Appl Sci Res. 1949;1(1):27-34.
[140] Joseph D, Tao L. The effect of permeability on the slow motion of a porous sphere in a viscous liquid. ZAMM-Journal of Applied Mathematics and Mechanics/Zeitschrift für Angewandte Mathematik und Mechanik. 1964;44(8-9):361-4.
[141] Sutherland DN, Tan CT. Sedimentation of a porous sphere. Chemical Engineering Science. 1970;25(12):1948-50.
[142] Neale G, Epstein N, Nader W. Creeping flow relative to permeable spheres. Chemical Engineering Science. 1973;28(10):1865-74.
[143] Tien C, Ramarao BV. Chapter 3 - Model representation of granular media. In: Tien C, Ramarao BV, eds. *Granular Filtration of Aerosols and Hydrosols (Second Edition)*. Oxford: Butterworth-Heinemann 2007:59-116.
[144] Abreu CRA, Macias-Salinas R, Tavares FW, Castier M. A Monte Carlo simulation of the packing and segregation of spheres in cylinders. Brazilian Journal of Chemical Engineering. 1999;16(4):395-405.
[145] Visscher WM, Bolsterli M. Random packing of equal and unequal spheres in two and three dimensions: Los Alamos Scientific Lab., N. Mex.(USA); 1973.
[146] Powell M. Computer-simulated random packing of spheres. Powder Technology. 1980;25(1):45-52.
[147] Jodrey W, Tory E. Computer simulation of isotropic, homogeneous, dense random packing of equal spheres. Powder Technology. 1981;30(2):111-8.
[148] Cundall PA, Strack OD. A discrete numerical model for granular assemblies. Geotechnique. 1979;29(1):47-65.
[149] Cundall P. Distinct element models of rock and soil structure. Analytical and computational methods in engineering rock mechanics. 1987;4:129-63.
[150] Theuerkauf J, Witt P, Schwesig D. Analysis of particle porosity distribution in fixed beds using the discrete element method. Powder Technology. 2006;165(2):92-9.
[151] Langston PA, Tüzün U, Heyes DM. Discrete element simulation of granular flow in 2D and 3D hoppers: Dependence of discharge rate and wall stress on particle interactions. Chemical Engineering Science. 1995;50(6):967-87.
[152] Heyes DM, Baxter J, Tüzün U, Qin RS. Discrete-Element Method Simulations: From Micro to Macro Scales. Philosophical Transactions: Mathematical, Physical and Engineering Sciences. 2004;362(1822):1853-65.
[153] Kloosterman J, Ougouag A. Comparison and extension of dancoff factors for pebble-bed reactors. Nuclear Science and Engineering. 2007;157(1):16-29.
[154] Visscher WM, Bolsterli M. Random Packing of Equal and Unequal Spheres in Two and Three Dimensions. Nature. 1972;239(5374):504-7.

[155] Freund H, Zeiser T, Huber F, Klemm E, Brenner G, Durst F, et al. Numerical simulations of single phase reacting flows in randomly packed fixed-bed reactors and experimental validation. Chemical Engineering Science. 2003;58(3–6):903-10.
[156] Torquato S. Random Heterogeneous Materials: Microstructure and Macroscopic Properties: Springer 2002.
[157] Yeong CLY, Torquato S. Reconstructing random media. Physical Review E. 1998;57(1):495-506.
[158] Adler P, Jacquin C, Quiblier J. Flow in simulated porous media. International Journal of Multiphase Flow. 1990;16(4):691-712.
[159] Adler P, Brenner H. Porous Media: Geometry and Transports: Elsevier Science 2013.
[160] Giona M, Adrover A. Closed-form solution for the reconstruction problem in porous media. AIChE Journal. 1996;42(5):1407-15.
[161] Cahn JW. Phase separation by spinodal decomposition in isotropic systems. The Journal of Chemical Physics. 1965;42(1):93-9.
[162] Berk N. Scattering properties of a model bicontinuous structure with a well defined length scale. Physical review letters. 1987;58(25):2718.
[163] Berk N. Scattering properties of the leveled-wave model of random morphologies. Physical Review A. 1991;44(8):5069.
[164] Roberts A, Teubner M. Transport properties of heterogeneous materials derived from Gaussian random fields: Bounds and simulation. Physical Review E. 1995;51(5):4141.
[165] Roberts A, Knackstedt M. Structure-property correlations in model composite materials. Physical Review E. 1996;54(3):2313.
[166] Yao J, Thovert J, Adler P, Burganos V, Payatakes A, Moulu J, et al. Characterization, reconstruction and transport properties of Vosges sandstones. Revue-Institut Francais du Petrole. 1997;52:3-22.
[167] Tessier J, Packer K, Thovert JF, Adler P. NMR measurements and numerical simulation of fluid transport in porous solids. AIChE journal. 1997;43(7):1653-61.
[168] Salles J, Thovert JF, Delannay R, Prevors L, Auriault JL, Adler P. Taylor dispersion in porous media. Determination of the dispersion tensor. Physics of Fluids A: Fluid Dynamics (1989-1993). 1993;5(10):2348-76.
[169] Bekri S, Thovert J, Adler P. Dissolution of porous media. Chemical Engineering Science. 1995;50(17):2765-91.
[170] Bekri S, Vizika O, Thovert J-F, Adler P. Binary two-phase flow with phase change in porous media. International Journal of Multiphase Flow. 2001;27(3):477-526.
[171] Hazlett R. Statistical characterization and stochastic modeling of pore networks in relation to fluid flow. Mathematical Geology. 1997;29(6):801-22.
[172] O'Connor R, Fredrich J. Microscale flow modelling in geologic materials. Physics and Chemistry of the Earth, Part A: Solid Earth and Geodesy. 1999;24(7):611-6.
[173] Kwiecien M, Macdonald I, Dullien F. Three-dimensional reconstruction of porous media from serial section data. Journal of Microscopy. 1990;159(3):343-59.
[174] Odgaard A, Andersen K, Melsen F, Gundersen HJG. A direct method for fast three-dimensional serial reconstruction. Journal of microscopy. 1990;159(3):335-42.
[175] Odgaard A. Three-dimensional methods for quantification of cancellous bone architecture. Bone. 1997;20(4):315-28.

[176] Courtois J, Szumski M, Georgsson F, Irgum K. Assessing the Macroporous Structure of Monolithic Columns by Transmission Electron Microscopy. Analytical Chemistry. 2006;79(1):335-44.
[177] Plummer CJG, Hilborn JG, Hedrick JL. Transmission electron microscopy methods for the determination of void content in polyimide thin film nanofoams. Polymer. 1995;36(12):2485-9.
[178] Man W, Donev A, Stillinger FH, Sullivan MT, Russel WB, Heeger D, et al. Experiments on Random Packings of Ellipsoids. Physical Review Letters. 2005;94(19):198001.
[179] Sederman AJ, Alexander P, Gladden LF. Structure of packed beds probed by Magnetic Resonance Imaging. Powder Technology. 2001;117(3):255-69.
[180] Bromley EHC, Hopkinson I. Confocal Microscopy of a Dense Particle System. Journal of Colloid and Interface Science. 2002;245(1):75-80.
[181] Claxton NS, Fellers TJ, Davidson MW. Microscopy, Confocal. *Encyclopedia of Medical Devices and Instrumentation*: John Wiley & Sons, Inc. 2006.
[182] Fu X, Dutt M, Bentham AC, Hancock BC, Cameron RE, Elliott JA. Investigation of particle packing in model pharmaceutical powders using X-ray microtomography and discrete element method. Powder Technology. 2006;167(3):134-40.
[183] Chaouki J, Larachi F, Duduković MP. Noninvasive Tomographic and Velocimetric Monitoring of Multiphase Flows. Industrial & Engineering Chemistry Research. 1997;36(11):4476-503.
[184] Atwood RC, Jones JR, Lee PD, Hench LL. Analysis of pore interconnectivity in bioactive glass foams using X-ray microtomography. Scripta Materialia. 2004;51(11):1029-33.
[185] Ho ST, Hutmacher DW. A comparison of micro CT with other techniques used in the characterization of scaffolds. Biomaterials. 2006;27(8):1362-76.
[186] Jaecques SVN, Van Oosterwyck H, Muraru L, Van Cleynenbreugel T, De Smet E, Wevers M, et al. Individualised, micro CT-based finite element modelling as a tool for biomechanical analysis related to tissue engineering of bone. Biomaterials. 2004;25(9):1683-96.
[187] Jones AC, Milthorpe B, Averdunk H, Limaye A, Senden TJ, Sakellariou A, et al. Analysis of 3D bone ingrowth into polymer scaffolds via micro-computed tomography imaging. Biomaterials. 2004;25(20):4947-54.
[188] Ketcham RA, Carlson WD. Acquisition, optimization and interpretation of X-ray computed tomographic imagery: applications to the geosciences. Computers & Geosciences. 2001;27(4):381-400.
[189] Lim KS, Barigou M. X-ray micro-computed tomography of cellular food products. Food Research International. 2004;37(10):1001-12.
[190] Shen H, Nutt S, Hull D. Direct observation and measurement of fiber architecture in short fiber-polymer composite foam through micro-CT imaging. Composites Science and Technology. 2004;64(13–14):2113-20.
[191] Salvo L, Cloetens P, Maire E, Zabler S, Blandin JJ, Buffière JY, et al. X-ray micro-tomography an attractive characterisation technique in materials science. Nuclear Instruments and Methods in Physics Research Section B: Beam Interactions with Materials and Atoms. 2003;200(0):273-86.

[192] Suzuki M, Kawabata K, Iimura K, Hirota M. Particle Shape Measurement Using X-ray Micro Computed Tomography. JOURNAL-SOCIETY OF POWDER TECHNOLOGY. 2004;41(3):156-61.
[193] Suzuki M, Ojima K, Iimura K, Hirota M. Measurement of Vertical Voidage Distribution in Powder Packed Bed Using X-ray Micro Computed Tomography-Comparison between Piston Compression and Centrifugal Compression. J Soc Powder Technol, Japan. 2004;41:663-7.
[194] Suzuki M, Shinmura T, Iimura K, Hirota M. Study of the wall effect on particle packing structure using X-ray micro computed tomography. Advanced Powder Technology. 2008;19(2):183-95.
[195] Bauer D, Chaves H, Arcoumanis C. Measurements of void fraction distribution in cavitating pipe flow using x-ray CT. Measurement Science and Technology. 2012;23(5):055302.
[196] Calvo S, Beugre D, Crine M, Léonard A, Marchot P, Toye D. Phase distribution measurements in metallic foam packing using X-ray radiography and micro-tomography. Chemical Engineering and Processing: Process Intensification. 2009;48(5):1030-9.
[197] Feldkamp LA, Davis LC, Kress JW. Practical cone-beam algorithm. J Opt Soc Am A. 1984;1(6):612-9.
[198] Sasov AY. Microtomography I. Methods and equipment. Journal of Microscopy. 1987;147(2):169-78.
[199] Sasov AY. Microtomography II. Examples of applications. Journal of Microscopy. 1987;147(2):179-92.
[200] Demirkaya O, Ritman EL. Noise reduction in x-ray microtomographic images by anisotropic diffusion filtration of the scanner projection images. 1999; 1999. p. 690-7.
[201] Hsieh J, Molthen RC, Dawson CA, Johnson RH. An iterative approach to the beam hardening correction in cone beam CT. Medical physics. 2000;27:23.
[202] Fajardo RJ, Ryan TM, Kappelman J. Assessing the accuracy of high-resolution x-ray computed tomography of primate trabecular bone by comparisons with histological sections. American Journal of Physical Anthropology. 2002;118(1):1-10.
[203] Ding M, Odgaard A, Hvid I. Accuracy of cancellous bone volume fraction measured by micro-CT scanning. Journal of Biomechanics. 1999;32(3):323-6.
[204] Hara T, Tanck E, Homminga J, Huiskes R. The influence of microcomputed tomography threshold variations on the assessment of structural and mechanical trabecular bone properties. Bone. 2002;31(1):107-9.
[205] Mitton D, Cendre E, Roux JP, Arlot ME, Peix G, Rumelhart C, et al. Mechanical Properties of Ewe Vertebral Cancellous Bone Compared With Histomorphometry and High-Resolution Computed Tomography Parameters. Bone. 1998;22(6):651-8.
[206] Waarsing JH, Day JS, Weinans H. An Improved Segmentation Method for In Vivo μCT Imaging. Journal of Bone and Mineral Research. 2004;19(10):1640-50.
[207] Wonho O, Lindquist B. Image thresholding by indicator kriging. Pattern Analysis and Machine Intelligence, IEEE Transactions on. 1999;21(7):590-602.
[208] Otsu N. A Threshold Selection Method from Gray-Level Histograms. Systems, Man and Cybernetics, IEEE Transactions on. 1979;9(1):62-6.
[209] Sheppard AP, Sok RM, Averdunk H. Techniques for image enhancement and segmentation of tomographic images of porous materials. Physica A: Statistical Mechanics and its Applications. 2004;339(1–2):145-51.

[210] Sezgin M, Sankur Bl. Survey over image thresholding techniques and quantitative performance evaluation. Journal of Electronic Imaging. 2004;13(1):146-68.
[211] Pal NR, Pal SK. A review on image segmentation techniques. Pattern Recognition. 1993;26(9):1277-94.
[212] Ioannou D, Huda W, Laine AF. Circle recognition through a 2D Hough transform and radius histogramming. Image and Vision Computing. 1999;17(1):15-26.
[213] Yuen H, Princen J, Illingworth J, Kittler J. Comparative study of Hough transform methods for circle finding. Image and Vision Computing. 1990;8(1):71-7.
[214] Thiedmann R, Spettl A, Stenzel O, Zeibig T, Hindson JC, Saghi Z, et al. Networks of nanoparticles in organic–inorganic composites: algorithmic extraction and statistical analysis. Image Anal Stereol, under revision. 2012.
[215] Spanne P, Thovert J, Jacquin C, Lindquist W, Jones K, Adler P. Synchrotron computed microtomography of porous media: topology and transports. Physical Review Letters. 1994;73(14):2001.
[216] Coles M, Hazlett R, Spanne P, Soll W, Muegge E, Jones K. Pore level imaging of fluid transport using synchrotron X-ray microtomography. Journal of Petroleum Science and Engineering. 1998;19(1):55-63.
[217] Ferreol B, Rothman DH. Lattice-Boltzmann simulations of flow through Fontainebleau sandstone. *Multiphase Flow in Porous Media*: Springer 1995:3-20.
[218] Auzerais F, Dunsmuir J, Ferreol B, Martys N, Olson J, Ramakrishnan T, et al. Transport in sandstone: a study based on three dimensional microtomography. Geophysical Research Letters. 1996;23(7):705-8.
[219] Mantle M, Sederman A, Gladden L. Single-and two-phase flow in fixed-bed reactors: MRI flow visualisation and lattice-Boltzmann simulations. Chemical Engineering Science. 2001;56(2):523-9.
[220] Manz B, Gladden L, Warren P. Flow and dispersion in porous media: Lattice-Boltzmann and NMR studies. AIChE journal. 1999;45(9):1845-54.
[221] Bernsdorf J, Brenner G, Durst F. Numerical analysis of the pressure drop in porous media flow with lattice Boltzmann (BGK) automata. Computer physics communications. 2000;129(1):247-55.
[222] Liu M, Liu G. Smoothed particle hydrodynamics (SPH): an overview and recent developments. Archives of computational methods in engineering. 2010;17(1):25-76.
[223] Holmes DW, Williams JR, Tilke P. Smooth particle hydrodynamics simulations of low Reynolds number flows through porous media. International Journal for Numerical and Analytical Methods in Geomechanics. 2011;35(4):419-37.
[224] Jiang F, Oliveira MS, Sousa AC. Mesoscale SPH modeling of fluid flow in isotropic porous media. Computer Physics Communications. 2007;176(7):471-80.
[225] Tartakovsky AM, Meakin P. Pore scale modeling of immiscible and miscible fluid flows using smoothed particle hydrodynamics. Advances in Water Resources. 2006;29(10):1464-78.
[226] Liu M, Liu G. Smoothed Particle Hydrodynamics (SPH): an Overview and Recent Developments from Lecture notes on the smoothed particle hydrodynamics (SPH). Archives of Computational Methods in Engineering. 2010;17(1):25-76.
[227] Hashemi MR, Fatehi R, Manzari MT. A modified SPH method for simulating motion of rigid bodies in Newtonian fluid flows. International Journal of Non-Linear Mechanics.

[228] Asai M, Aly AM, Sonoda Y, Sakai Y. A stabilized incompressible SPH method by relaxing the density invariance condition. Journal of Applied Mathematics. 2012;2012.
[229] Cummins SJ, Rudman M. An SPH Projection Method. Journal of Computational Physics. 1999;152(2):584-607.
[230] Hu XY, Adams NA. An incompressible multi-phase SPH method. Journal of Computational Physics. 2007;227(1):264-78.
[231] Hosseini SM, Manzari MT, Hannani SK. A fully explicit three-step SPH algorithm for simulation of non-Newtonian fluid flow. International Journal of Numerical Methods for Heat & Fluid Flow. 2007;17(7):715-35.
[232] Krog E. GPU-based Real-Time Snow Avalanche Simulations. Trondhiem: Norwegian University of Science and Technology; 2010.
[233] Colin F, Egli R, Lin FY. Computing a null divergence velocity field using smoothed particle hydrodynamics. Journal of Computational Physics. 2006;217(2):680-92.
[234] Shao S, Lo EYM. Incompressible SPH method for simulating Newtonian and non-Newtonian flows with a free surface. Advances in Water Resources. 2003;26(7):787-800.
[235] Morris JP, Fox PJ, Zhu Y. Modeling low Reynolds number incompressible flows using SPH. Journal of computational physics. 1997;136(1):214-26.
[236] Potapov AV, Hunt ML, Campbell CS. Liquid–solid flows using smoothed particle hydrodynamics and the discrete element method. Powder Technology. 2001;116(2-3):204-13.
[237] Colagrossi A, Landrini M. Numerical simulation of interfacial flows by smoothed particle hydrodynamics. Journal of Computational Physics. 2003;191(2):448-75.
[238] Shao S. Incompressible SPH simulation of water entry of a free-falling object. International Journal for Numerical Methods in Fluids. 2009;59(1):91-115.
[239] Kelager M. Lagrangian Fluid Dynamics Using Smoothed Particle Hydrodynamics. Copenhagen, Denmark: University of Copenhagen; 2006.
[240] Liu GR, Liu B. Smoothed Particle Hydrodynamics: A Meshfree Particle Method: World Scientific 2003.
[241] Mills PL, Quiram DJ, Ryley JF. Microreactor technology and process miniaturization for catalytic reactions—A perspective on recent developments and emerging technologies. Chemical Engineering Science. 2007;62(24):6992-7010.
[242] Jung S, Ehlert S, Mora J-A, Kraiczek K, Dittmann M, Rozing GP, et al. Packing density, permeability, and separation efficiency of packed microchips at different particle-aspect ratios. Journal of Chromatography A. 2009;1216(2):264-73.
[243] Zivkovic V, Biggs MJ, Alwahabi ZT. Experimental study of a liquid fluidization in a microfluidic channel. AIChE Journal. 2013;59(2):361-4.
[244] Zivkovic V, Kashani M, Biggs M. Experimental and theoretical study of a micro-fluidized bed. POWDERS AND GRAINS 2013: Proceedings of the 7th International Conference on Micromechanics of Granular Media; 2013: AIP Publishing; 2013. p. 93-6.
[245] Doroodchi E, Peng Z, Sathe M, Abbasi-Shavazi E, Evans GM. Fluidisation and packed bed behaviour in capillary tubes. Powder Technology. 2012;223:131-6.
[246] Doroodchi E, Sathe M, Evans G, Moghtaderi B. Liquid–liquid mixing using micro-fluidised beds. Chemical Engineering Research and Design. 2013;91(11):2235-42.
[247] Reyes DR, Iossifidis D, Auroux PA, Manz A. Micro total analysis systems. 1. Introduction, theory, and technology. Analytical chemistry. 2002;74(12):2623-36.
[248] Aggarwal P, Tolley HD, Lee ML. Monolithic bed structure for capillary liquid chromatography. Journal of Chromatography A. 2012;1219(0):1-14.

[249] Unger KK, Skudas R, Schulte MM. Particle packed columns and monolithic columns in high-performance liquid chromatography-comparison and critical appraisal. Journal of Chromatography A. 2008;1184(1):393-415.
[250] Dautzenberg F, Mukherjee M. Process intensification using multifunctional reactors. Chemical Engineering Science. 2001;56(2):251-67.
[251] DeStefano J, Langlois T, Kirkland J. Characteristics of superficially-porous silica particles for fast HPLC: some performance comparisons with sub-2-μm particles. Journal of chromatographic science. 2008;46(3):254-60.
[252] González RC, Woods RE. Digital Image Processing: Pearson/Prentice Hall 2008.
[253] The MathWorks Inc. MATLAB and Image Processing Toolbox Natick, Massachusetts, United States R2013a.
[254] Rasband WS. ImageJ. U. S. National Institutes of Health, Bethesda, Maryland, USA (http://imagej.nih.gov/ij/) 1997-2013.
[255] Sage D, Prodanov D, Tinevez J-Y, Schindelin J. MIJ: Making Interoperability Between ImageJ and Matlab Possible. *ImageJ User & Developer Conference*. Luxembourg 2012.
[256] Gonzalez RCA, Woods REA, Eddins SLA. Digital image processing: using MATLAB: Prentice Hall 2004.
[257] Navvab Kashani M, Zivkovic V, Elekaei H, Biggs MJ. A new method for reconstruction of the structure of micro-packed beds of spherical particles from desktop X-ray microtomography images. Part A. Initial structure generation and porosity determination. Chemical Engineering Science. 2015.
[258] McGreevy RL. Reverse monte carlo modelling. Journal of Physics: Condensed Matter. 2001;13(46):R877.
[259] Kirkpatrick S, Jr. DG, Vecchi MP. Optimization by simmulated annealing. Science. 1983;220(4598):671-80.
[260] Georgalli GA, Reuter MA. A particle packing algorithm for pellet design with a predetermined size distribution. Powder Technology. 2007;173(3):189-99.
[261] Zivkovic V, Biggs M. On importance of surface forces in a microfluidic fluidized bed. Chemical Engineering Science. 2015;126:143-9.
[262] Biggs M, Zivkovic V, Kashani M, Alwahabi Z. Importance of surface forces in a micro-fluidized bed. Chemeca 2012: Quality of life through chemical engineering: 23-26 September 2012, Wellington, New Zealand. 2012:698.
[263] de Klerk A. Voidage variation in packed beds at small column to particle diameter ratio. AIChE Journal. 2003;49(8):2022-9.
[264] Torquato S. Random heterogeneous materials: microstructure and macroscopic properties: Springer Science & Business Media 2002.
[265] Bernal JD, Mason J. Packing of Spheres: Co-ordination of Randomly Packed Spheres. Nature. 1960 12/10/print;188(4754):910-1.
[266] Stone HA, Stroock AD, Ajdari A. Engineering flows in small devices: microfluidics toward a lab-on-a-chip. Annu Rev Fluid Mech. 2004;36:381-411.
[267] Manz A, Graber N, Widmer Há. Miniaturized total chemical analysis systems: a novel concept for chemical sensing. Sensors and actuators B: Chemical. 1990;1(1):244-8.
[268] Tsukagoshi K, Jinno N, Nakajima R. Development of a micro total analysis system incorporating chemiluminescence detection and application to detection of cancer markers. Analytical chemistry. 2005;77(6):1684-8.

[269] Kovarik ML, Gach PC, Ornoff DM, Wang Y, Balowski J, Farrag L, et al. Micro total analysis systems for cell biology and biochemical assays. Analytical chemistry. 2011;84(2):516-40.
[270] Cheng Y, Zhu C, Xie Z, Gu H, Tian T, Zhao Y, et al. Anisotropic colloidal crystal particles from microfluidics. Journal of colloid and interface science. 2014;421:64-70.
[271] Nezhad AS. Microfluidic platforms for plant cells studies. Lab on a Chip. 2014;14(17):3262-74.
[272] Navvab Kashani M, Zivkovic V, Elekaei H, Herrera LF, Affleck K, Biggs MJ. A new method for reconstruction of the structure of micro-packed beds of spherical particles from desktop X-ray microtomography images. Part B. Structure refinement and analysis. Chemical Engineering Science. 2015.
[273] Bruns S, Tallarek U. Physical reconstruction of packed beds and their morphological analysis: Core–shell packings as an example. Journal of Chromatography A. 2011;1218(14):1849-60.
[274] Monaghan JJ. Smoothed particle hydrodynamics. Reports on progress in physics. 2005;68(8):1703.
[275] Monaghan JJ. Smoothed particle hydrodynamics. Annual review of astronomy and astrophysics. 1992;30:543-74.
[276] Tartakovsky AM, Meakin P, Scheibe TD, West RME. Simulations of reactive transport and precipitation with smoothed particle hydrodynamics. Journal of Computational Physics. 2007;222(2):654-72.
[277] Monaghan J. Smoothed particle hydrodynamics and its diverse applications. Annual Review of Fluid Mechanics. 2012;44:323-46.
[278] Shao S, Lo EY. Incompressible SPH method for simulating Newtonian and non-Newtonian flows with a free surface. Advances in Water Resources. 2003;26(7):787-800.
[279] Heusser C. Conjugate gradient-type algorithms for a finite-element discretization of the Stokes equations. Journal of computational and applied mathematics. 1992;39(1):23-37.
[280] Libersky LD, Petschek AG, Carney TC, Hipp JR, Allahdadi FA. High Strain Lagrangian Hydrodynamics: A Three-Dimensional SPH Code for Dynamic Material Response. Journal of Computational Physics. 1993;109(1):67-75.
[281] Monaghan JJ. Simulating Free Surface Flows with SPH. Journal of Computational Physics. 1994;110(2):399-406.
[282] Clift R, Grace JR, Weber ME. Bubbles, Drops, and Particles: Academic Press 1978.
[283] Mitra SK, Chakraborty S. Microfluidics and Nanofluidics Handbook: Chemistry, Physics, and Life Science Principles: CRC Press 2011.
[284] Jakobsen HA. Chemical reactor modeling. Multiphase Reactive Flows, Berlin, Germany: Springer-Verlag. 2008.